Aeroelastic Tailoring of Composite Aircraft

Natella, M.

DOI
10.4233/uuid:48af4e9b-1487-4402-a1aa-19e302b0eb97

Publication date
2020

Document Version
Final published version

Citation (APA)
Natella, M. (2020). *Aeroelastic Tailoring of Composite Aircraft*. [Dissertation (TU Delft), Delft University of Technology]. https://doi.org/10.4233/uuid:48af4e9b-1487-4402-a1aa-19e302b0eb97

AEROELASTIC TAILORING OF COMPOSITE AIRCRAFT

AEROELASTIC TAILORING OF COMPOSITE AIRCRAFT

Proefschrift

ter verkrijging van de graad van doctor
aan de Technische Universiteit Delft,
op gezag van de Rector Magnificus Prof. ir. T. H. J. J. van der Hagen
voorzitter van het College voor Promoties,
in het openbaar te verdedigen op maandag 30 november 2020 om 10:00 uur

door

Mario NATELLA
Master of Science in Aerospace Engineering, Technische Universiteit Delft
born in Battipaglia, Italy

Lucht- en Ruitevaarttechniek,
Technische Universiteit Delft, Nederland.

Dit proefschrift is goedgekeurd door de

promotor: Dr. ir. R. De Breuker
promotor: Prof. dr. C. Bisagni

Samenstelling promotiecommissie:

Prof. dr. ir. T.H.J.J. van der Hagen	Rector Magnificus en Voorzitter
Prof. dr. C. Kassapoglou	Technische Universiteit Delft
Prof. dr. ir. L. Veldhuis	Technische Universiteit Delft

Onafhankelijke leden/Independent members:

Prof. dr. E. Carrera	Politecnico di Torino
Dr. O. Stodiek	University of Bristol
P.H.A.P. Cabral	Embraer, Brazil

Keywords: aeroelastic tailoring, structural design, stiffness optimization

Printed by: Ipskamp Printing

Front & Back: Designed by Mario Natella

ISBN 978-94-6421-117-7

An electronic version of this dissertation is available at
http://repository.tudelft.nl/.

He thinks in secret, and it comes to pass:
Environment is but his looking-glass.
J. Allen

CONTENTS

SUMMARY

Aeroelastic Tailoring of Composite Aircraft

The process of designing an aircraft is generally divided in three phases, namely the conceptual, preliminary and detailed. The whole process is one that involves various disciplines and is subject to multiple constraints. Traditionally the different aspects of the design process are tackled separately by different departments within a company. This approach assumes that there is little to no interaction between the various disciplines. The use of composite materials for aircraft structures has challenged this traditional approach on the account that the interaction between the relevant disciplines within aircraft design and optimization cannot be neglected as easily.

With the present dissertation, the author builds upon the aeroelastic tailoring framework developed at the Delft University of Technology by R. De Breuker to provide a coupled framework for the analysis and optimization of composite aircraft at preliminary design level. The low-fidelity approach inevitably requires to simplify the formulations used to describe the relevant disciplines in aircraft analysis and optimization. The simplification allows to develop coupled models to address the most important concerns already at preliminary design level. In addition to aerodynamics and structural dynamics, used in classic aeroelastic tailoring, the framework developed by the author addresses passive maneuver load alleviation, body-freedom stability, handling qualities and dynamic loads. With a preliminary design that already includes an initial assessment of relevant phenomena, the chances of major costly changes in the later stages of the design process is reduced. Furthermore, with the use of low-fidelity frameworks, one can explore more design options and even configurations before selecting the best candidates for the detailed design phase. The design studies on the aircraft configurations, however, are outside of the scope of the present dissertation.

The base of the framework for analysis and optimization of aircraft structures is the monolithic coupling between structural dynamics, aerodynamics and flight dynamics. The wing is divided in independent property regions in span- and chord-wise section. The parts of the structure within any given property regions inherit the stiffness and mass properties. These remain constant within one property region. The stiffness of a laminate is described in lamination parameters to allow for gradient-based optimization with analytical derivatives. The 3D structure is condensed into a 1D beam model by means of a cross-sectional modeler. The framework consists of a geometrically nonlinear static aeroelastic model and a dynamic aeroelastic model that is linearized around the static aeroelastic equilibrium solution. The flight dynamic equations are derived in the Euler formulation and coupled to the structural equations of motion to describe the dynamics of free bodies.

The static aeroelastic model is based on a 2D vortex lattice aerodynamic model to account for the effects of wing camber, and with eccentric follower and non-follower forces to account for the effects of, for example, engine thrust or gravity on the wing designs. The dynamic aeroelastic model couples a dynamic structural model, including the effects of non-structural masses and based on Timoshenko beam elements, to an unsteady aerodynamic model based on the unsteady vortex lattice method to obtain a monolithic system of continuous-time state-space equations describing the dynamic aeroelastic response of the wing. The control surfaces, for passive load alleviation purposes, are modeled by applying an additional hinge rotation to the aerodynamic panel.

The optimized wing designs are obtained using a gradient-based optimizer for computational efficiency where the sensitivities of the aeroelastic responses with respect to the design variables are computed analytically. In order to validate the model, a series of studies have been performed on each of the fundamental modules of the framework. The model used for the verification studies is the NASA CRM aircraft. The reference results are obtained in NASTRAN®, where an equivalent model of the CRM aircraft has been build for verification purposes.

To illustrate the advantages of the framework, three different studies are carried out. First, the optimized design obtained using the framework implemented within this dissertation is benchmarked against the classic aeroelastic tailoring practice. This study highlights the importance of relevant interactions mechanisms, e.g. body-freedom instabilities and handling qualities. The second study discusses the implication of three distinct choices for the optimization of the laminate stiffness. In this study, the author shows how some of the concerns and requirements coming from the aerospace industry, with respect to composite manufacturing, can already be incorporated at preliminary design level. The last study, addresses the criticality of dynamic loads on the aeroelastic tailoring of a composite wing. The aim of the last study is to contextualize the results obtained in classic aeroelastic tailoring concerning the criticality of dynamic loads.

To conclude, the analysis and optimization framework developed in this dissertation has been successfully applied to the optimization studies on composite aircraft for commercial aviation. The studies *i)* highlight the implications of comprehensive models at preliminary design level, *ii)* demonstrate how industry standards and certification requirements can be incorporated in the initial low-fidelity studies and *iii)* question and give more context to the state-of-the-art practices of classic aeroelastic tailoring.

1

INTRODUCTION

A century has flown by since the first commercial aircraft took off thus changing our paradigm of mobility for good. Since that moment aircraft have changed radically, pushed by a staggering increase in demand. Famous became the words of PanAm to Boeing in the 1960s:

"You build it, I buy it."

Words that motivated the start of the 747 project. A memorable moment in aviation history.

The giant steps in commercial aviation have gone hand-in-hand with the technological development of the various disciplines involved in aircraft design, which is - itself - strongly influenced by the political and economical scenario. As of this writing, the combination of stricter environmental concerns and the need for higher revenue dictated by the private sector is determining the current, and future design challenges in the aviation industry. Common objectives such as weight reduction, fuel efficiency, increased payload and greener design are almost a constant in current aircraft design philosophy.

It is interesting to see how externally imposed constraints have shaped the aircraft design concepts and thus lead to the fundamental thoughts behind this research. The strong need for greener structures implies weight reduction, a challenge that presents engineers and designers with new problems within the fields of aeroelasticity and stress analysis. Lighter structures feature high flexibility making phenomena of aeroelastic nature some of the sizing criteria in aircraft design.

Since first observed in the early 1900s, aeroelastic phenomena have played a significant role in aircraft structural design. Different ways to account for aeroelasticity have been investigated. For example, in the first half of the 20^{th} century, common practice advised local stiffening of wing structures to suppress aeroelastic instabilities, [1]. A solution that does not comply with the modern weight reduction policies. It was not until the late

second half of the 1900s that new engineering solutions became available since (1) the understanding of aeroelastic phenomena had grown more solid, and (2) composite materials had found their way into the aeronautical industry.

The use of composite materials in aircraft design marked the start of a new methodology for aircraft optimization. In 1986, in the work by Shirk et al. [1], the new methodology was referred to as *aeroelastic tailoring*. Aeroelastic tailoring is an optimization method that aims at tailoring the material and geometric properties of the structure for enhanced performance. The methodology allows for smart use of materials, proper smearing of properties throughout the structure and total control of the response to any perturbation. Nevertheless, modern aircraft design has brought new challenges for structural engineers. The increasing use of light and slender wings leads to structural configurations featuring low natural frequencies which can easily couple with aircraft rigid body motions, as discussed in [2], [3], [4] and [5].

Realizing the importance of aircraft motions as a consequence of the enhanced flexibility in wing structures brings a new challenge at early stages of the design process, thus contributing to the development of preliminary analysis tools for the design of advanced aircraft structures.

1.1. RESEARCH GOAL

In order to extend aeroelastic tailoring to a composite aircraft, different aspects and disciplines are to be combined in a unified framework for a good assessment (in terms of analysis and design) of real structure. The goal of this dissertation, providing the basis to the contribution of this work, is thus to:

develop a preliminary analysis and optimization framework for aeroelastic tailoring of a free flying composite aircraft.

This work builds upon the state-of-the-art aeroelastic tailoring framework developed at Delft University of Technology [6]. The main problem statement is broken down into 4 objectives in the attempt to encompass all important aspects of the research. The objectives are illustrated in Fig.1.1.

1.1.1. OBJECTIVE I: ADVANCED LO-FI AIRCRAFT MODEL

The aeroelastic framework, used in this research, operates on low-fidelity representation of the aircraft structure using Timoshenko beam theory. While this approach gives a more fundamental understanding of the problem, it inevitably requires a simplified model that remains representative of its more complex counterpart.
With the low-fidelity aircraft model, the author wants to provide a powerful tool for radical feasibility studies at preliminary design level. In particular, the term *advanced* refers to the fact that the low-fidelity model describes the 3D model in its structural details. The complex topology of 3D models makes it impractical to conduct high-fidelity analyses and optimizations at an acceptable computational time.

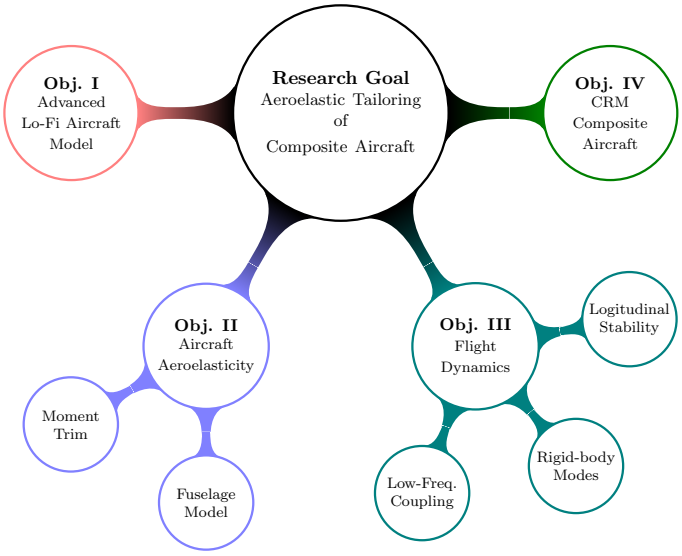

Figure 1.1: Mind map illustrating the research goal and objectives.

1.1.2. OBJECTIVE II/III: FREE-FLYING AIRCRAFT

These two objectives, namely *aircraft aeroelasitic*y and *flight dynamics of a flexible aircraft* are the pillars upon which the aeroelastic tailoring for composite aircraft is built.

The *aircraft aeroelasticity* will allow us to quantify the fuselage and tail contribution to the aerodynamic loads on the wing structure. In addition to that, the aircraft can be trimmed both for force and moment equilibrium. The moment equilibrium is expected to change the loading conditions on the main wing structure and thus have an effect on the analysis and optimization of its composite structure.

Using the *flight dynamic model for a flexible aircraft* at equilibrium, the longitudinal stability of the trim condition can be assessed. The assessment will take aeroelastic and rigid body modes into consideration, thus accounting for low-frequency coupling (typical phenomenon observed in flexible aircraft structures). The longitudinal stability of the aircraft will be an additional constraint in the optimization process, thus influencing the search for an optimum design at minimum weight and optimized stiffness distribution. The author expects to quantify the penalty in terms of additional structural mass on the main wing structure due to enforcing said constraints. Modeling the longitudinal flight dynamics also allows to quantify the handling qualities of the aircraft, and enforce the required levels of maneuverability. The lateral aspects are however outside of the scope of this dissertation.

1.1.3. OBJECTIVE IV: AICRAFT BENCHMARK MODEL

This last objective is envisioned as a technical application of the approach to aeroelastic tailoring developed in this research. The benchmark wills serve as a starting point for further research in the field of aeroelastic tailoring. The aircraft will be based on the NASA CRM model and designed using the unified framework developed as part of this dissertation.

1.2. OUTLINE OF DISSERTATION

The contribution of this dissertation is categorized in three main aspects, namely *(i)* the technical contribution to the state of the art aeroelastic tailoring framework, *(ii)* the application of the framework to extensive tailoring studies on a composite aircraft structure and *(iii)* the assessment of dynamic load criticality for composite aircraft.

Part I of the dissertation discusses the technical contribution to the state of the art aeroelastic framework. In particular, Chapter 3 discusses the structural model and the detailed derivation of dynamic equations of motion for flexible structures, the aerodynamic model and maneuverability assessment of the aircraft.

Part II focuses on the design studies. In Chapter 4, the effect of the full aircraft aerodynamic model on aeroelastic tailoring is investigated, whereas in Chapter 5 the various stiffness optimization strategies for composite structures are presented. Finally, in Chapter 6, the criticality of gust loads for free-free structures will be discussed.

1.3. NOVELTY OF DISSERTATION

The novelty of the framework developed in this dissertation is to be found in the following contributions to the aeroelastic tailoring work developed at Delft University of Technology, [6]. In particular,

- a monolithic description is developed to describe the aeroelasticity of a free-free flexible aircraft in its longitudinal aspect; the monolithic approach presented in Chapter 3. This approach allows to describe the dynamics of free-free composite structure and perform advanced aeroelastic tailoring optimization studies that include body-freedom stability constraint and handling qualities; the optimization studies are presented in Chapter 4,
- a novel stiffness tailoring approach is developed, named Principal Direction Optimization, to be able to apply aeroelastic tailoring optimization techniques on standard certified laminates; this novel approach to aeroelastic tailoring is presented in Chapter 5, and
- gust loads have been included in the aeroelastic tailoring optimization framework on the full free-free flexible aircraft, including passive maneuver load alleviation. This is an addition to the classic approach for clamp-free structures, [6]; the dynamic optimization studies are presented in Chapter 6.

These three additions make the aeroelastic framework more comprehensive to address analyses and optimization problems of composite aircraft in preliminary design.

REFERENCES

[1] M. Shirk, H. T.J., and T. Weisshaar, *Aeroelastic tailoring - theory, practice and promise,* Journal of Aircraft, Vol. 23, No. 1 (1987).

[2] M. J. Patil, *Nonlinear aeroelastic analysis, flight dynamics, and control of a complete aircraft,* PhD Thesis, Georgia Institute of Technology, Atlanta, GA (1999).

[3] W. Su, *Coupled nonlinear aeroelasticity and flight dynamics of fully flexible aircraft,* PhD Thesis, The University of Michigan, Ann Arbor, MI (2008).

[4] C. Cesnik, M. Patil, and D. Hodges, *Nonlinear aeroelastic analysis of complete aircraft in subsonic flow,* Journal of Aircraft, Vol. 27, No. 5, pp. 753-760 (2000).

[5] C. Cesnik, M. Patil, and D. Hodges, *Nonlinear aeroelasticity and flight dynamics of high-altitude long endurance aircraft,* Journal of Aircraft, Vol. 38, No. 1, pp. 88-94 (2001).

[6] N. Werter, *Aeroelastic modelling and design of aeroelastically tailored and morphing wings,* PhD Dissertation, Delft University of Technology (2017).

2

Recent Progress in Aeroelastic Tailoring Design

As the name implies, aeroelasticity is at the core of aeroelastic tailoring frameworks. The term *tailoring* indicates the fact that the structure and its properties are designed against specific loading conditions and performance requirements. The aeroelastic tailoring design framework is multidisciplinary by nature, and the number of disciplines coupled to the framework increases with the problem complexity. Together with structural dynamics and aerodynamics, the building blocks of *classic* aeroelasticity, another important aspect when addressing aircraft structures is the flight dynamics. Aeroelasticity and flight dynamics have traditionally been developed as separate disciplines. However, the need for considering interaction efforts was recognized very early. On this note, it is worth mentioning the work by Collar in 1946, "The Expanding Domain Of Aeroelasticity" [1], J. B. Rea in 1957, "Aeroelasticity In Aircraft Stability And Control Theory" [2] and A. S. Taylor in 1959, "The Present Status Of Aircraft Stability Problems In The Aeroelastic Domain" [3].

The scarcity of efforts in linking aeroelasticity and flight dynamics was justified - in the 1950s - by three important considerations:

- aeroelasticity was a very young discipline at the time, and some of the fundamental understanding was still under development,
- the increase in problem complexity made analysis and optimization impractical given the computational power available at the time,
- aircraft structural flexibility was still rather limited reaching about 15% wing-tip deflection only at ultimate load.

As a result, problems combining aeroelasticity and flight dynamics have been subject to many simplifying assumptions designed to permit large analyses and optimizations.

This section reviews the relevant literature in the attempt to gather significant results and insights regarding the coupling of aeroelasticity and flight dynamics. Although the literature fails to address the effect of coupling on the tailored composite design, it provides important observations describing crucial phenomena caused by the interaction between flight dynamic and aeroelastic models. This will help acquiring a solid background knowledge for the present dissertation.

2.1. AEROELASTIC TAILORING

The promise of aeroelastic tailoring was to develop a design framework that could enhance aircraft structural performance at large. The idea sees great recognition in the research community in the 1980s with important works by Shirk et al. [4], Weisshaar et al.[5], and recent developments by Werter et al. [6], Stanford et al. [7], and Stodiek et al. [8]. State-of-the-art aeroelastic tailoring practices have developed frameworks to solve the problem at a wing level. The results in terms of weight saving, load alleviation and/or range optimization are very promising, thus justifying the further development in this field. The combined developments on both fundamental theories, material engineering and computational power have given the opportunity to tackle more and more complex problems. The application of aeroelastic tailoring to the design and optimization of a composite wing is a multi-disciplinary problem. In this section, the progress made in each of the relevant disciplines is presented.

2.1.1. MODELING APPROACHES

The early studies, Shirk et al. [4], Weisshaar et al. [5], explored the potential of aeroelastic tailoring using a single fiber angle, thus describing most of the fundamental aeroelastic phenomena affecting the design of composite wings, for example flutter and divergence, and how to prevent them by inducing a beneficial bend-twist coupling. In the late 1990s, aeroelastic tailoring research started to focus on laminates with different fiber angles through the thickness, an approach that increased the level of complexity of the models to describe more realistic composite structures. There are three main approaches to this problem found in literature, namely using *(i)* laminates with a fixed thickness, but varying fiber angles, *(ii)* laminates with a fixed set of fiber angles, and varying thickness and *(iii)* laminates with both varying fiber angles and varying thickness.

The first approach, where the thickness is kept constant, has been solved with evolutionary algorithms, Georgiou et al. [9], Manan et al. [10], Guo et al. [11], or fiber steering, Haddadpour et al. [12], Stodieck et al. [8], Stanford et al. [7], to maximize flutter speed. Both approaches already show significant improvements in overall aeroelastic performance due to varying stiffness along the span of the wing compared to the classic approach with straight fibers.

The second approach, with a fixed set of discrete ply angles, provides a solution to comply with certification requirements, reduce the number of design variables (Eastep et al. [13], Kim et al. [14], Tian et al. [15]) and improve aeroelastic performance under different set of constraints including buckling, strains and aileron effectiveness.

The aeroelastic framework developed by De Breuker et al. [16] and Werter et al. [6] focuses on the third approach where both fiber angles and thickness are modeled as design variables to explore the full potential of aeroelastic tailoring and simplify the formulation of the optimization problem. In contrast to working with fiber angles directly, the formulation where both thickness and fiber angles are varying can be described in the continuous domain using lamination parameters thus making this problem fit for gradient-based solvers and optimization frameworks. The first description of lamination parameters related to aeroelastic tailoring was introduced by Kameyama et al. [17]. The approach was first proved for a flat composite panel, where the set of lamination parameters and thickness was calculated for maximum flutter speed. The work of Jin et al. [18], and Dillinger et al. [19] has scaled this approach to solve a similar problem for the whole wing, modeled as a multitude of chordwise and spanwise panels for a more detailed description of a composite wingbox and its structural elements.

The methodology combines classic aeroelasticity and optimization algorithms to deliver advanced structural designs. Aeroelastic tailoring is set up as a minimization problem. The algorithm explores the design space looking for the structural design at minimum weight. The search for the local or global minimum also leads to a design at low root bending moment. This consideration qualifies aeroelastic tailoring as a powerful approach for load alleviation in modern composite structures and to eliminate flutter problems. In this regard, T. A. Weisshaar comments on an important physical aspect of aeroelastic tailoring. Weisshaar [5] proves how classic flutter speed (i.e. clamped-root flutter speed) is maximized when optimizing a composite wing design using aeroelastic tailoring.

The problem arises when the classic clamped-root assumption is removed. Free-flying flexible structures show a new instability known as *body-freedom flutter*. Body-freedom flutter is a dynamic instability that involves aircraft pitching and lifting surface deformation. Such an instability is also caused by aeroelastic tailoring itself. While aeroelastic tailoring maximizes the classic flutter speed, the body-freedom flutter speed is actually descreasing making this phenomenon an important design constraint.

2.1.2. CLASSIC AEROELASTIC TAILORING

Throughout this dissertation, the term *classic aeroelastic tailoring* refers to the aeroelastic tailoring optimization of a composite wing structure clamped at the root. These studies have helped assessing the feasibility of the method and have contributed to the application of aeroelastic tailoring to complex problems like the optimization of real-life composite wings, addressing modeling, certification and manufacturing challenges.

Important advances in this field of research are found in the work of Werter et al. [20] in 2015. The work presents an extensive study and optimization on the NASA Common Research Model (CRM). The study shows the effect of aeroealstic tailoring on thickness and stiffness distribution of the wing structure. This is an example of how the material and structural properties adapt to the particular requirements imposed by the flight con-

ditions and design constraints. The results from this study provide design guidelines for (conventional) composite wings subject to maneuver loads. The properties of the wing, both stiffness and mass, are smeared in a 'smart' way, allocating it where necessary based on the loading severity in each region. The load severity is a case-dependent constraint the user should carefully specify depending on the aicraft mission, and flight envelope.

Similar studies, that contribute to a deeper understanding of the potentialities of aeroelastic tailoring, are found in the work by Cooper et al. [21]. The discussion focuses on high-level performance of the wing model, namely weight saving, load alleviation and flutter suppression in a composite wing. The analytical predictions via aeroelastic tailoring are supported with an experimental test campaign aimed at proving the validity of the approach.

Both references previously discussed focus on medium to low-fidelity approaches to structures and aerodynamic modeling. The implementation of the methodology to high-fidelity structures poses a challenge both from the modeling and computation aspect, as discussed in [19], in the attempt to extend the modeling capabilities of the optimization approach. Buckling and aileron effectiveness constraints are applied and the structure is optimized under cruise, maneuver and landing loads. The results prove the importance of buckling constraints in aeroelastic tailoring. The constraint is active for skin panels under compression loads, thus being one of the main sizing factors for the structural design. The work by Dillinger et al. [19] is also the first to extend the use of lamination parameters to the design of a wingbox structure and use a gradient-based optimizer to search for optimum thickness and stiffness distribution (given in terms of lamination parameters). The wing is discretized in property regions at constant stiffness and thickness to minimize structural under various case-dependent constraints. High-fidelity aeroelastic loads and gradients can further increase the quality of the optimum design, as extensively discussed in the work by Jovanov [22].

It is important to note a consequence of the choice of lamination parameters as design variables for aeroelastic tailoring optimization. The set of lamination parameters is a high-level description of the stiffness properties of a laminate and allows for a fast assessment of all structural performance (e.g. strains, buckling, failure etc.), however it provides no information regarding the actual stacking sequence of the laminates. Going from lamination parameters to stacking sequence (lay-up) is a separate discrete optimization problem, outside the scope of this dissertation. The solution to this problem, from a mathematical point of view, is not uniquely defined if not for a laminate with an infinite number of plies. For this reason, it requires a discrete or genetic optimization scheme to determine a (manufacturable) stacking sequence that matches the target lamination parameters within a user-specified tolerance. In the formulation of this problem, the manufacturing and/or certification aspects can be included to be able to calculate a realistic and cost-effective lay-up sequence for the entire wing or other structural part considered. More literature in this field of research can be found in [23], [24].

In view of a more complete analysis, it is important to understand the classic aeroe-

lastic phenomena in the context of the whole aircraft, in particular with respect to the interaction of the wing with fuselage and tails. The first problem encompasses the solution to the flow around the full aircraft configuration, in particular in the area near the wing-body junction. A very extensive explanation of the fuselage aerodynamics, including the effects of the wing-body interaction and its importance is found in the work of Singh et al. [25]. The main contributions of the fuselage aerodynamics are a large pitching moment and a destabilizing neutral point shift upstream. A minor contribution is the increase of effective angle of attack at the root of the wing. The lift generated by the fuselage itself is negligible. Further details regarding the interaction phenomena in a full aircraft configuration are found in the work of Rusak et al. [26]. Another important point to discuss is the vortex shedding of the body, although there is no comprehensive model to describe the phenomenon, experimental evidence shows how the effect of the body wake on the longitudinal aerodynamic coefficient is of orders of magnitude smaller, thus negligible.

2.1.3. CHOICES FOR THIS DISSERTATION IN AEROELASTIC TAILORING

To summarize, the advancement in low- and medium-fidelity physical models for the description of the aeroelastic framework have made new solutions available at the preliminary design level. Already in the early phases of the design process, it is possible to develop a framework for analysis and optmization which is capable to select an improved design candidate for the more detailed phases ahead. Certification aspects and manufacturability constraints are also important parts of the problem that can be incorporated at this level. The benefit of the low-fidelity approach is in the capability of exploring a wide range of the design space at a relative small computational effort or cost. A preliminary study of this size would be almost unfeasible with any 2D or 3D finite element description.

In this spirit, the following choices have been made for the aeroelastic framework used as basis for this dissertation.

- The structural properties (design variables of the aeroelastic tailoring optimization) are modeled in accordance with the third category (described in Subsection 2.1.1) where both ply angles and the thickness distribution of the laminates are independent parameters. The variation of ply angles is however controlled by the set of lamination parameters.

- The standard constraints included in the aeroelastic tailoring framework are: *(i)* aeroelastic stability either of a clamped-free or free-free wing model, *(ii)* material failure, *(iii)* buckling, *(iv)* aileron effectiveness.

- The aeroelastic tailoring optimization will use a gradient-based optimizer. The sensitivities of objective and constraints with respect to the design variables for all modules within the framework are calculated analytically.

2.2. FLIGHT DYNAMICS

As mentioned earlier in this report, flight dynamics and aeroelasticity are traditionally decoupled. The method is applicable for aircraft configurations featuring a clear separation in the frequency of aeroelastic modes and rigid modes. With the development of lighter and more slender wing structures, the choice of a decoupled system may result in a precarious assumption, at best. For example, the longitudinal stability of the trim condition is no longer an assumption, but it becomes a constraint for the design. The new trend in aircraft structural design requires a new framework for design, analysis and optimization based on flexible flight dynamics.

Different flight dynamic formulations in literature are presented. The first point of focus is the choice of a proper reference frame for the derivation of the equations of motion. The choice has been proven fundamental for the accuracy of the analytical description. Several analytical approaches within the research field are presented.

2.2.1. FRAMES OF REFERENCE

A targeted choice of reference frame is fundamental for an efficient derivation of the flight dynamic equations of motion (EOM). In this context the term *efficient* refers to a formulation that is accurate for the purposes of the present work, while simplified in its analytical formulation in order to facilitate the use and solution of the system.

The first concern when selecting the frame of reference is the inertia coupling. Common practice advices the use of a Lagrangian description in body axes aligned instantaneously with the principal axes. The formulation as such leads to a diagonal inertia tensor, thus facilitating derivation and manipulation of the EOM. An equivalent approach is the Newtonian formulation, where the flexibility is accounted in the definition of the position vector of any given point of structure.

The choice of the origin has a significant impact on the flight dynamic description. For rigid aircraft dynamics one could locate the origin of the reference frame at the center of mass. With the increase in flexibility, and under severe loading conditions, the position of the center of mass varies continuously. A frame of reference that features this behaviour is referred to as floating reference, [27]. The complexity of a flight dynamic description in a floating reference has lead to the mean axes approximation, [28, 29]. Said approximation stems from the assumption of inertia decoupling between the structural-dynamics and rigid body equations. This leads to enforcing the linear angular momentum, due to the elastic deformation, to be zero.

The interested reader can investigate the detailed mathematical formulation of the mean axes constraint, as well as its application and direct impact on the energy expressions, [30]. The approach is customary in literature, although its validity is still a major point of discussions and controversies, [30].

2.2.2. ANALYTICAL MODEL

One of the important works on the aeroelastic properties of flexible aircraft has been presented by Van Schoor and Von Flotow, [31]. The study suggests that modeling flexibility and unsteady aerodynamics is fundamental in order to properly describe aircraft dynamics. On that note, a study carried out by Waszak and Schmidt, [29], presents an analytical method in Lagrangian formulation to derive the non-linear equation of a flexible aircraft. A later study, presented by Newman and Schmidt, [32], proposes a reduced order model for flight dynamics of a flexible aircraft. The method allows to get physical insights of the system itself, as well as an approximate expression of zeroes and poles for stability purposes. The energy approach in a Lagrangian formulation as proposed by Waszak and Schmidt, [29], is suitable to easily generate an accurate description of the flight dynamics of a flexible aircraft, even for unconventional configurations that feature canards or multiple tails. An equivalent system can also be built using a Newtonian formulation. The system derived with any of the two methods is fully coupled and non-linear but can be linearized around any given configuration for stability analyses. Although not as accurate, the reduced model is more appropriate for low-fidelity analysis in preliminary design. The underlying assumption in the reduced model presented by Newman and Schmidt, [32], is that the flight dynamics system is linearized about the deformed configuration, and therefore the perturbation is assumed relatively small compared to the wing span. The linear assumption has been widely used in literature. Relevant examples can be also found in [33–35].

Meirovitch and Tuzcu [30] worked on a new paradigm for the dynamics and control of a flexible aircraft. The theory integrates structural dynamics, aerodynamics and controls. The unified formulation includes rigid-body degrees of freedom, elastic deformations, and all forces acting on the aircraft, namely gravity, thrust, aerodynamic, control forces, and exogenous disturbances. A seamless integration is achieved through the use of the same reference frame to describe all the aircraft motions and forces acting on it and the equations of motion are expressed in terms of quasi-coordinates, derived in an earlier work by Meirovitch [30].

As previously mentioned while discussing the frames of reference, the choice of axes, either fixed, or mean, influences the performance of the analytical model. In particular, the mean axis frame is a free floating reference frame positioned at the instantaneous center of gravity of the body, and thereby modeling no inertia coupling. In the fixed-axis approach, on the other hand, this coupling is taken into account. Reschke [36, 37] formulates the equations of motion for the elastic aircraft using a Lagrangian in fixed-axes. The approach incorporates finite element (FE) models of the aircraft structure. The proposed method is suitable for loads computation and flight dynamic investigations. Li [38] and Abbasi [39] investigated differences between the mean-axis and a fixed-axis approach finding moderate differences, however leaving certain interesting points open for further investigation. As the fixed-axes equations consider the effect of elastic deformation on the 1^{st} and 2^{nd} mass moments of inertia they have the potential to produce more accurate results. Nikravesh [40] provided a comprehensive comparison of the mean-axis and fixed-axis equations.

2.2.3. CHOICES FOR THIS DISSERTATION IN FLIGHT DYNAMICS

The technical choices regarding the details of the flight dynamic model is highly case-dependent and, most importantly, result-dependent. The objective of the flight dynamic model in the aeroelastic tailoring framework developed in this dissertation is to assess the free-free longitudinal stability of a linearized dynamic aeroelastic model. In this respect, the following decision have been made.

- to use a Newtonian formulation, verified analytically against the equivalent Lagrangian, and
- a mean-axis formulation has been chosen, thus removing the inertia coupling.

2.3. COUPLED AEROELASTICITY AND FLIGHT DYNAMICS

Important insights about the coupling phenomena are provided in the study by Dowell et al. [41]. A wing-only type of configuration has been analysed. The configuration as such serves as a good benchmark to gather data on the coupling effect. Nevertheless, the quality of the analysis and the predictions can be enhanced by more elaborate configurations, namely wing-horizontal tail, or wing-horizontal and vertical tail, and at last full aircraft.

The works of Nguyen et al., [42], and Cesnik and Shearer, [43], present a finite element wing model coupled with aircraft motions about the principal axes (roll, pitch, yaw). These studies highlight the importance of flight dynamics in the aircraft modal response and flutter onset. The lighter and more slender the wing structure, the more important it is to consider aircraft motions in the wing design. This consideration becomes crucial when analyzing particular aircraft configurations. On that note the work of Cesnik et al., [44–46], reporting on aeroelasticity and flight dynamics of HALE aircraft (High-Altitude Long Endurance) discusses the aeroelastic effects observed in light and slender structures. Their results show that large wing deflections due to high-aspect-ratio may significantly change the aerodynamic load distribution comparing to the undeformed configuration. As a consequence, the linear approach may not be valid. The extent to which the wing structure deflects will give an indication as to what type of analysis has to be performed in which particular case. The importance of low frequency coupling has been confirmed by later studies, [47].

The effect of coupled aeroelasticity and flight dynamics on the aeroelastic performance of conventional aicraft configurations has been addressed in recent years, focusing on stability and control phenomena. In the work by Cesnik and Su, [48], one can find a non-linear aeroelastic analysis of a fully flexible aircraft, with a detailed model of tails and fuselage.

The model allows for a thorough assessment of control, maneuverability, as well as aeroelastic effects of the whole aicraft. Non linear flight dynamics of flexbile aircraft has also been presented by Chang et al. [49]. The study reports on the effect of large deflections on the aeroelastic phenomena. The strong coupling has been identified as the main cause of the high sensitivities observed in the aeroelastic analysis. In addition, the

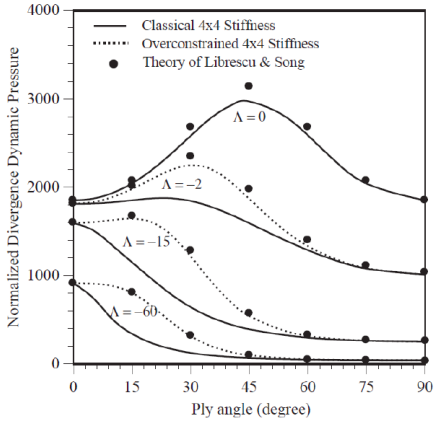

Figure 2.1: Variation of divergence dynamics pressure with ply angle, [33].

study also provides a baseline for a thorough understanding of the significance, accuracy and limitation of the results obtained at preliminary design level.

Numerical tests on different aircraft configurations have been carried out by Patil [33], Brown [50] and Su [34]. The composite beam model adopted in the formulation is geometrically-exact, and coupled with 2D finite-state unsteady aerodynamics. The aircraft is modeled as fully flexible. The equation of motion is formulated from the virtual work principle, and the fully non-linear coupled system thus derived is then linearized about the non-linear deformed configuration.

The formulation as presented in the aforementioned references encompasses a wide range of aircraft configurations, [48, 51, 52]. The studies not only investigate the effect of rigid body motions on aeroelastic stability, but the effect on global aeroelastic phenomena is also addressed. Ply angles in a composite wing structure have been proven to be relevant in the assessment of particular aeroelastic phenomena. In support of this statement, Patil [33] reports on the change of divergence speed with ply angle, see Fig. 2.1. In particular, with positive ply angles one can obtain favourable bending-twisting coupling, thus increasing the divergence speed. The exact opposite holds for negative ply angles. The positive orientation is defined with respect to the wing box reference frame, as described in the aforementioned reference. Flutter is also influenced by both flight dynamics and aeroelastic tailoring, although it is more diffcult to identify the direct physical quantities playing a role in the flutter onset.

REFERENCES

[1] A. R. Collar, *The expanding domain of aeroelasticity,* Journal of the Royal Aeronautical Society, Vol. 50, p.428 (1946).

[2] J. B. Rea, *Aeroelasticity in stability and control,* Wright Air Development Center Technical Report 55-173 (1957).

[3] A. S. Taylor, *The present status of aircraft stability problems in the aeroelastic domain,* Journal of the Royal Aeronautical Society, Vol. 63, p.580 (1959).

[4] M. Shirk, H. T.J., and T. Weisshaar, *Aeroelastic tailoring - theory, practice and promise,* Journal of Aircraft, Vol. 23, No. 1 (1987).

[5] T. Weisshaar, *Aeroelastic tailoring - creative use of unusual materials,* AIAA/ASME/ASCE/AHS 28th Structures, Structural Dynamics and Material Conference, Monterey, CA. April 6-8 (1987).

[6] N. Werter, *Aeroelastic modelling and design of aeroelastically tailored and morphing wings,* PhD Dissertation, Delft University of Technology (2017).

[7] B. K. Stanford, C. D. Wiesman, and s. C. V. Jutte, *Aeroelastic tailoring of transport wings including transonic flutter constraints,* 56th AIAA/ASCE/AHS/ASC Structures, Structural Dynamics, and Materials Conference, AIAA SciTech Forum, https://doi.org/10.2514/6.2015-1127 (2015).

[8] O. Stodieck, J. Cooper, P. Weaver, and P. Kealy, *Aeroelastic tailoring of a representative wing-box using tow-steered composites,* AIAA Journal, DOI: 10.2514/1.J055364 (2016).

[9] G. Georgiou, G. Vio, and J. E. Cooper, *Aeroelastic tailoring and scaling using bacterial foraging optimisation,* Structural and Multidisciplinary Optimization, vol. 50, no. 1, pp. 81–99, doi:10.1007/s00158-013-1033-3 (2014).

[10] A. Manan, G. Vio, M. Y. Harmin, and J. E. Cooper, *Optimization of aeroelastic composite structures using evolutionary algorithms,* Engineering Optimization, vol. 42, no. 2, pp. 171–184, doi:10.1080/03052150903104358 (2010).

[11] S. Guo, J. Bannerjee, and C. W. Cheung, *The effect of laminate lay-up on the flutter speed of composite wings,* Proceedings of the Institution of Mechanical Engineers Part G: Journal of Aerospace Engineering, vol. 217, no. 3, pp. 115–122, doi:10.1243/095441003322297225 (2003).

[12] H. Haddadpour and Z. Zamani, *Curvilinear fiber optimization tools for aeroelastic design of composite wings,* Journal of Fluids and Structures, vol. 33, pp. 180–190. doi:10.1016/j.jfluidstructs.2012.05.008 (2012).

[13] F. E. Eastep, V. A. Tischler, V. B. Venkayya, and N. S. Khot, *Aeroelastic tailoring of composite structures,* Journal of Aircraft, vol. 36, no. 6, pp. 1041–1047, doi:10.2514/2.2546 (1999).

[14] T. U. Kim and I. H. Hwang, *Optimal design of composite wing subjected to gust loads,* Computers and Structures, vol. 83, no. 19-20, pp. 1546–1554, doi: 10.1016/J.Compstruc.2005.02.002 (2005).

[15] W. Tian, Z. Yang, Y. Gu, and Y. Ouyang, *Aeroelastic tailoring of a composite forward-swept wing using a novel hybrid pattern search method,* Journal of Aerospace Engineering, vol. 29, no. 6. doi:10.1061/(ASCE)AS. 1943-5525000652. (2016).

[16] R. De Breuker, M. Abdalla, and Z. Gürdal, *A generic morphing wing analysis and design framework,* Journal of Intelligent Material Systems and Structures, vol. 22, no. 10, pp. 1025-1039 (2011).

[17] M. Kameyama and H. Fukunaga, *Optimum design of composite plate wings for aeroelastic characteristics using lamination parameters,* Computers and Structures, vol. 85, no. 3-4, pp. 213–224. doi:10.1016/J.Compstruc.20068.051 (2007).

[18] P. Jin, B. Song, X. Zhong, T. Yu, and F. Xu, *Aeroelastic tailoring of composite sandwich panel with lamination parameters,* Proceedings of the Institution of Mechanical Engineers, Part G: Journal of Aerospace Engineering, vol. 230, no. 1. doi:10.1177/0954410015587724 (2016).

[19] J. Dillinger, T. Klimmek, M. M. Abdalla, and Z. Gürdal, *Stiffness optimization of composite wings with aeroelastic constraints,* Journal of Aircraft, vol. 50, no. 4, pp. 1159–1168. doi:10.2514/1.C032084 (2013).

[20] N. Werter, R. De Breuker, and M. Abdalla, *Continuous-time stat-space unsteady aerodynamic modelling for efficient aeroelastic load analysis,* International Forum on Aeroelasticity and Structural Dynamics, June 28 - July 2 2015, Saint Petersburg, Russia (2015).

[21] J. Cooper, G. Francois, and P. Weaver, *Aeroelastic tailoring using crenellated skins – modelling and experiment,* Advances in aircraft and spacecraft science (2016).

[22] K. Jovanov, *High-fidelity load and gradient corrections for static aeroelastic tailoring of composite wings,* PhD Dissertation at Delft University of Technology https://doi.org/10.4233/uuid:14b55d5e-586a-4641-8990-55a397674db8 (2019).

[23] R. Hafka and J. Walsh, *Stacking-sequence optimization for buckling of laminated plates by integer programming,* AIAA Journal, vol. 30, no. 3, pp. 814-819, https://doi.org/10.2514/3.10989 (1992).

[24] D. Peeters, F. Irisarri, and M. Abdalla, *Optimizing the ply dropping order in variable stiffness, variable thickness laminates using stacking sequence tables,* ECCM17, Munich, Germany (2016).

[25] S. Singh, N.and Aikat and B. Basu, *Incompressible potential flow about complete aircraft configurations,* Aeronautical Journal, 93(929):335–343 (1989).

[26] Z. Rusak, E. Wasserstrom, and A. Seginer, *Numerical calculation of nonlinear aerodynamics of wing-body configurations,* AIAA Journal, 21(7):929–936 (1983).

[27] A. A. Shabana, *Dynamics stability of a rotating pre-twisted asymmetric cross section timoshenko beam subject to an axial periodic force,* International Journal of Mechanical Sciences, 48: 579-590 (1997).

[28] R. D. Milne, *Dynamics of the deformable aeroplane, parts i and ii,* Aeronautical Research Council Reports and Memoranda, No. 3345 (1962).

[29] M. Waszak and D. Schmidt, *Flight dynamics of aeroelastic vehicles,* Journal of Aircraft, Vol. 27, No. 10, pp. 901-908 (1990).

[30] L. Mierovitch and I. Tuzcu, *The lure of mean axes,* Journal of Applied Mechanics, Vol. 74, p. 497 (2007).

[31] M. VanSchoor and A. VonFlotow, *Aeroelastic characteristics of a highly flexible aircraft,* Journal of Aircraft, Vol. 27, No. 10 (1990).

[32] B. Newman and D. Schmidt, *Numerical and literal aeroelastic-vehicle model reduction for feedback control synthesis,* Journal of Guidance, Control and Dynamics, Vol. 14, No. 5, pp. 943-953 (1991).

[33] M. J. Patil, *Nonlinear aeroelastic analysis, flight dynamics, and control of a complete aircraft,* PhD Thesis, Georgia Institute of Technology, Atlanta, GA (1999).

[34] W. Su, *Coupled nonlinear aeroelasticity and flight dynamics of fully flexible aircraft,* PhD Thesis, The University of Michigan, Ann Arbor, MI (2008).

[35] J. Murua, *Flexible aircraft dynamics with a geometrically nonlinear description of the unsteady aerodynamics,* PhD Dissertation, Imperial College, London, United Kingdom (2012).

[36] C. Reschke, *Flight loads analysis with inertially coupled equations of motion,* AIAA Atmospheric Flight Mechanics Conference (2005).

[37] C. Reschke, *Integrated flight loads modeling and analysis for flexible transport,* Aircraft. PhD thesis, Universitat Stuttgart (2006).

[38] N. Li, P. Grant, and H. Abbasi., *A comparison of the fixed-axes and the mean-axes modeling methods for flexible aircraft simulation,* Guidance, Navigation,and Control and Co-located Conferences, American Institute of Aeronautics and Astronautics (2010).

[39] H. Abbasi, P. Grant, and N. Li., *Real-time simulation of flexible aircraft: a comparison of two methods,* Guidance, Navigation, and Control and Co-located Conferences, American Institute of Aeronautics and Astronautics (2009).

[40] P. Nikravesh, *Understanding mean-axis conditions as floating reference frames,* Advances in Computational Multibody Systems, 2:185–203 (2005).

[41] E. Dowell, J. Edwards, and T. Strganac, *Nonlinear aeroelasticity,* 44th AIAA/ASME/ASCE/AHS Structures, Structural Dynamics and Material Conference, Norfolk, VA, Apr. 7-10 (2003).

[42] N. Nguyen, K. Trinh, D. Nguyen, and I. Tuzcu, *Nonlinear aeroelasticity of a flexible wing structure coupled with aircraft flight dynamics,* 53rd AIAA Structures, Structural Dynamics and Material Conference, Honolulu, Hawaii (2012).

[43] C. Cesnik and M. Shearer, *Nonlinear flight dynamics of very flexible aircraft,* AIAA Atmospheric Flight Mechanics Conference and Exhibit, San Francisco, CA (2005).

[44] C. Cesnik, M. Patil, and D. Hodges, *Aeroelastic analysis of composite wings,* Proceedings of the 37th Structures, Structural Dynamics, and Material Conference, Salt Lake City, UT, Apr. 18-19, pp. 1113-1123 (1996).

[45] C. Cesnik, M. Patil, and D. Hodges, *Nonlinear aeroelastic analysis of complete aircraft in subsonic flow,* Journal of Aircraft, Vol. 27, No. 5, pp. 753-760 (2000).

[46] C. Cesnik, M. Patil, and D. Hodges, *Nonlinear aeroelasticity and flight dynamics of high-altitude long endurance aircraft,* Journal of Aircraft, Vol. 38, No. 1, pp. 88-94 (2001).

[47] E. Livne and T. Weishaar, *Aeroelasticity of nonconventional airplane configurations - past and future,* Journal of Aircraft, Vol. 40, No. 6, pp. 1047-1065 (2003).

[48] C. Cesnik and W. Su, *Nonlinear aeroelastic modeling and analysis of fully flexible aircraft,* AIAA, 46th AIAA/ASME/ASCE/AHS/ASC Structures, Structural Dynamics, and Material Conference, Austin, TX (2005).

[49] C. Chang, D. Hodges, and M. Patil, *Flight dynamics of highly flexible aircraft,* Journal of Aircraft, Vol. 45, No. 2, pp. 538-545 (2008).

[50] L. Brown, *Integrated strain actuation in aircraft with highly flexible composite wings,* PhD Dissertation, MIT, Cambridge, MA (2003).

[51] C. Cesnik and W. Su, *Nonlinear aeroelasticity of a vert flexible blended-wing body aircraft,* 50th AIAA/ASME/ASCE/AHA/ASC Structures, Structural Dynamics, and Material Conference, Palm Springs, CA, USA (2009).

[52] C. Cesnik and W. Su, *Dynamic response of highly flexible aircraft,* AIAA Journal, 49 (2): 324-339, doi: 10.2514/1.J050496 (2011).

3

ANALYSIS FRAMEWORK

The aeroelastic framework required to assess the aeroelastic performance of a composite aircraft is presented in this chapter. As outlined in the introduction to this dissertation, this work builds upon the state-of-the-art aeroelastic tailoring framework developed at Delft University of Technology [1]. This chapter highlights the contribution of this work to the development of said framework. The verification of the framework is performed on the NASA Common Research Model presented in details in Appendix C.

3.1. DYNAMICS OF FREE FLEXIBLE BODIES

In this section, the equations of motion describing the structural dynamics of free-free structures are derived, [2]. Removing the clamp constraint at the root (used in classic aeroelasticity) and introducing the additional longitudinal rigid degrees of freedom allows for more realistic predictions of the aeroelastic response of flexible aircraft in flight.

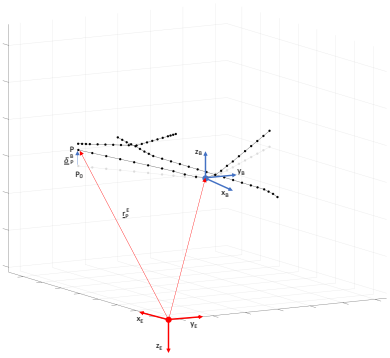

Figure 3.1: Illustration of the frames of reference and relevant quantities for the derivation of the EOMs.

3.1.1. FRAMES OF REFERENCE AND NOMENCLATURE

For the derivation of the equations of motion of free flexible bodies, two separate frames of reference are used, namely *(i)* the earth-fixed (inertial) frame indicated with superscript E, and *(ii)* body-fixed frame with superscript B, Fig. 3.1. The distance between the two frames is referred to as $\underline{r}^E_{EB}(t)$, which is in the most general case a function of time (t). Note that underlined quantities indicate vectors, while double underline refers to matrices. Other important quantities to define before beginning with the derivation of the equations are given: P_0 is a point of the structure in its initial position at $t = 0$, P is a point of the structure in its deformed position at t, $\underline{r}^B_{P_0}(t)$ is the distance of the point P_0 from the origin of the body-fixed frame written in the body-fixed frame, $\underline{r}^E_P(t)$ is the distance of the point P from the origin of the earth-fixed frame written in the earth-fixed frame, $\underline{\delta}^B_P(t)$ is the distance between P_0 and P written in the body-fixed frame.

In the derivation of the system of equation, the following definition of degrees of freedom (DOFs) are used: structural DOFs are translations and rotation in the body-fixed frame defined at each structural node, rigid DOFs are the elevation, pitch and forward motion defined at the center of gravity of the structure (CG) since only the longitudinal aspect is taken into account in this dissertation.

3.1.2. EQUATIONS OF MOTION (EOM)

The derivation of the EOM that couples structural and flight dynamics begins by writing the position vector of point P (any point of the structures in its deformed position at time t) which is a function of both structural and rigid degrees of freedom.

$$\underline{r}^E_P(t) = \underline{r}^E_{EB}(t) + \underline{\underline{R}}_{BE}(t)\left(\underline{r}^B_{P_0} + \underline{\delta}^B_P(t)\right) \tag{3.1}$$

where $\underline{\underline{R}}_{BE}(t)$ is the rotation matrix from the body- to the earth-fixed frame, also a function of time. Let us now define the vector $\underline{r}^B_P(t)$ as:

$$\underline{r}^B_P(t) = \underline{r}^B_{P_0} + \underline{\delta}^B_P(t) \tag{3.2}$$

so that:

$$\underline{r}^E_P(t) = \underline{r}^E_{EB}(t) + \underline{\underline{R}}_{BE}(t)\underline{r}^B_P(t) \tag{3.3}$$

The velocity of point P can be thus written as:

$$\dot{\underline{r}}^E_P(t) = \dot{\underline{r}}^E_{EB}(t) + \tilde{\underline{\underline{\Omega}}}_{BE}\underline{\underline{R}}_{BE}\underline{r}^B_P(t) + \underline{\underline{R}}_{BE}\dot{\underline{\delta}}^B_P(t) \tag{3.4}$$

The derivation of the term $\tilde{\underline{\underline{\Omega}}}_{BE}\underline{\underline{R}}_{BE}$ is given in Appendix A. From the expression for the velocity vector, one can derive the acceleration as follows:

$$\ddot{\underline{r}}^E_P(t) = \ddot{\underline{r}}^E_{EB}(t) + \dot{\tilde{\underline{\underline{\Omega}}}}_{BE}\underline{\underline{R}}_{BE}\underline{r}^B_P(t) + \tilde{\underline{\underline{\Omega}}}_{BE}\tilde{\underline{\underline{\Omega}}}_{BE}\underline{\underline{R}}_{BE}\underline{r}^E_P(t) + 2\tilde{\underline{\underline{\Omega}}}_{BE}\underline{\underline{R}}_{BE}\dot{\underline{\delta}}^B_P(t) + \underline{\underline{R}}_{BE}\ddot{\underline{\delta}}^B_P(t) \tag{3.5}$$

where the following substitution has been made:

$$\dot{\underline{r}}^B_P(t) = \dot{\underline{r}}^B_{P_0} + \dot{\underline{\delta}}^B_P(t) \equiv \dot{\underline{\delta}}^B_P(t) \tag{3.6}$$

The angular acceleration can be derived by looking at the rotation matrix from the nodal- to a earth-fixed frame of reference, defined as $\underline{\underline{R}}_{EN}$. The matrix can be split in two rotations, namely:

$$\underline{\underline{R}}_{NE} = \underline{\underline{R}}_{BE}\underline{\underline{R}}_{NB} \tag{3.7}$$

Taking the time-derivative of both sides of the equation leads to:

$$\underline{\underline{\tilde{\Omega}}}_{NE}\underline{\underline{R}}_{NE} = \underline{\underline{\tilde{\Omega}}}_{BE}\underline{\underline{R}}_{BE}\underline{\underline{R}}_{NB} + \underline{\underline{R}}_{BE}\underline{\underline{\tilde{\Omega}}}_{NB}\underline{\underline{R}}_{NB} \tag{3.8}$$

Refer to Appendix A for a detailed derivation of the time derivative of a rotation matrix. By means of the Poisson's equation, relating nodal angular velocities to the associated rotor, one can write:

$$\underline{\underline{\tilde{\Omega}}}_{NB} = \underline{\dot{\delta}}^{B}_{\text{rot}}\underline{\underline{R}}_{EB} \tag{3.9}$$

where $\underline{\dot{\delta}}^{\text{rot}}_{BN}$ is the pseudo-vector of angular velocities defined at the structural nodes. Substituting it in Eq. 3.8:

$$\underline{\underline{\tilde{\Omega}}}_{NE}\underline{\underline{R}}_{NE} = \underline{\underline{\tilde{\Omega}}}_{BE}\underline{\underline{R}}_{BE}\underline{\underline{R}}_{NB} + \underline{\underline{R}}_{BE}\underline{\dot{\delta}}^{B}_{\text{rot}}\underline{\underline{R}}_{BE}\underline{\underline{R}}_{NB} \tag{3.10}$$

post-multiplying both sides of the equation by $\underline{\underline{R}}^{T}_{EN}$:

$$\underline{\underline{\tilde{\Omega}}}_{NE} = \underline{\underline{\tilde{\Omega}}}_{BE} + \underline{\underline{R}}_{BE}\underline{\dot{\delta}}^{B}_{\text{rot}} \tag{3.11}$$

or equivalently:

$$\underline{\omega}^{E}_{P}(t) = \underline{\omega}^{E}_{EB}(t) + \underline{\underline{R}}_{BE}\underline{\dot{\delta}}^{B}_{\text{rot}}(t) \tag{3.12}$$

from which the angular acceleration is derived as:

$$\underline{\dot{\omega}}^{E}_{P}(t) = \underline{\dot{\omega}}^{E}_{EB}(t) + \underline{\underline{\tilde{\Omega}}}_{BE}\underline{\underline{R}}_{BE}\underline{\dot{\delta}}^{B}_{\text{rot}}(t) + \underline{\underline{R}}_{BE}\underline{\ddot{\delta}}^{B}_{\text{rot}} \tag{3.13}$$

The quantities $\underline{\ddot{r}}^{E}_{P}(t)$, $\underline{\dot{\omega}}^{E}_{P}(t)$, $\underline{\dot{r}}^{E}_{P}(t)$, $\underline{\omega}^{E}_{P}(t)$, $\underline{r}^{E}_{P}(t)$ and the pseudo-vector with angular rotations $\underline{\theta}^{E}_{P}(t)$ can be used to build a coupled system in matrix form describing the dynamics of a flexible body at a nodal level (P). The system can then be scaled for multiple nodes thus describing the dynamics of the entire structure.

MATRIX SYSTEM AT A NODAL LEVEL

Let us hereby summarize the relationships found so far for velocity and angular velocity of the point P.

$$\underline{\ddot{r}}^{E}_{P}(t) = \underline{\ddot{r}}^{E}_{EB}(t) + \underline{\underline{\dot{\tilde{\Omega}}}}_{BE}\underline{\underline{R}}_{BE}\underline{r}^{B}_{P}(t) + \underline{\underline{\tilde{\Omega}}}_{BE}\underline{\underline{\tilde{\Omega}}}_{BE}\underline{\underline{R}}_{BE}\underline{r}^{E}_{P}(t) + 2\underline{\underline{\tilde{\Omega}}}_{BE}\underline{\underline{R}}_{BE}\underline{\dot{\delta}}^{B}_{P}(t) + \underline{\underline{R}}_{BE}\underline{\ddot{\delta}}^{B}_{P}(t) \tag{3.14}$$

$$\underline{\dot{\omega}}^{E}_{P}(t) = \underline{\dot{\omega}}^{E}_{EB}(t) + \underline{\underline{\tilde{\Omega}}}_{BE}\underline{\underline{R}}_{BE}\underline{\dot{\delta}}^{B}_{\text{rot}}(t) + \underline{\underline{R}}_{BE}\underline{\ddot{\delta}}^{B}_{\text{rot}} \tag{3.15}$$

These two equations can be written in matrix form as hereby shown. The terms indicated with index 1, 2 and 3 will be further discussed.

$$\begin{Bmatrix} \ddot{\underline{r}} \\ \dot{\underline{\omega}} \end{Bmatrix} = \begin{bmatrix} \underline{\underline{I}} \\ \underline{\underline{0}} \end{bmatrix} \underbrace{\ddot{\underline{r}}^E_{EB}}_{1} + \underbrace{\begin{bmatrix} -\underline{\underline{R}}_{BE}\tilde{\underline{\underline{r}}}^B_P \\ \underline{\underline{I}} \end{bmatrix}}_{2} \underbrace{\dot{\underline{\omega}}^E_{EB}}_{1} + \underbrace{\begin{bmatrix} \tilde{\underline{\underline{\Omega}}}_{BE} & \underline{\underline{0}} \\ \underline{\underline{0}} & \frac{1}{2}\tilde{\underline{\underline{\Omega}}}_{BE} \end{bmatrix}}_{3} \begin{bmatrix} \tilde{\underline{\underline{\Omega}}}_{BE} & \underline{\underline{0}} \\ \underline{\underline{0}} & \frac{1}{2}\tilde{\underline{\underline{\Omega}}}_{BE} \end{bmatrix} \begin{bmatrix} \underline{r}^E_P \\ \underline{0} \end{bmatrix} + \tag{3.16}$$

$$+2 \begin{bmatrix} \tilde{\underline{\underline{\Omega}}}_{BE} & \underline{\underline{0}} \\ \underline{\underline{0}} & \frac{1}{2}\tilde{\underline{\underline{\Omega}}}_{BE} \end{bmatrix} \begin{bmatrix} \underline{\underline{R}}_{BE} & \underline{\underline{0}} \\ \underline{\underline{0}} & \underline{\underline{R}}_{BE} \end{bmatrix} \begin{bmatrix} \dot{\underline{\delta}}_P \\ \dot{\underline{\delta}}_{\text{rot}} \end{bmatrix} + \begin{bmatrix} \underline{\underline{R}}_{BE} & \underline{\underline{0}} \\ \underline{\underline{0}} & \underline{\underline{R}}_{BE} \end{bmatrix} \begin{bmatrix} \ddot{\underline{\delta}}_P \\ \ddot{\underline{\delta}}_{\text{rot}} \end{bmatrix}$$

Note that:

1. $\ddot{\underline{r}}^E_{EB}(t)$ and $\dot{\underline{\omega}}^E_{EB}(t)$ are rigid constants applied to the node P. They model the flight dynamic contribution on top of the flexible one. To be consistent with the dimensions they should be written as follows:

$$[\ldots] \begin{bmatrix} \underline{\underline{I}} \\ \underline{\underline{0}} \end{bmatrix} \begin{bmatrix} \ddot{\underline{r}}^E_{EB} \\ \ddot{\underline{r}}^E_{EB} \end{bmatrix} + \begin{bmatrix} -\underline{\underline{R}}_{BE}\tilde{\underline{\underline{r}}}^B_P \\ \underline{\underline{I}} \end{bmatrix} \begin{bmatrix} \dot{\underline{\omega}}^E_{EB} \\ \dot{\underline{\omega}}^E_{EB} \end{bmatrix} [\ldots] \tag{3.17}$$

   The convention in Eq. 3.16 will be used since it makes the scaling of the system easier to follow.

2. From the rule of commutation of cross products:

$$\dot{\tilde{\underline{\underline{\Omega}}}}_{BE}\underline{\underline{R}}_{BE}\underline{r}^B_P(t) = -\underline{\underline{R}}_{BE}\tilde{\underline{\underline{r}}}^B_P(t)\dot{\underline{\omega}}^E_{EB}(t) \tag{3.18}$$

3. The content of the second row of the matrix is of no need since it multiplies zero. This mathematical expedient is used for two reasons, being: *(1)* avoid ill-defined matrices by moving the zeros to the vector, and *(2)* simplify the notation since the same matrix is found later in the expression multiplying the deformation vector.

The following nomenclature will be introduced to simplify the matrix equations at nodal level and thus simplify the derivation of the system for multiple nodes.

$$\begin{aligned} \underline{\underline{\tilde{I}}}_i &= \begin{bmatrix} \underline{\underline{I}} \\ \underline{\underline{0}} \end{bmatrix} & \underline{\underline{\tilde{r}}}_i &= \begin{bmatrix} -\underline{\underline{R}}_{BE}\tilde{\underline{\underline{r}}}^B_P \\ \underline{\underline{I}} \end{bmatrix} & \underline{\underline{\Omega}}_i &= \begin{bmatrix} \tilde{\underline{\underline{\Omega}}}_{BE} & \underline{\underline{0}} \\ \underline{\underline{0}} & \frac{1}{2}\tilde{\underline{\underline{\Omega}}}_{BE} \end{bmatrix} \\ \underline{\underline{R}}_i &= \begin{bmatrix} \underline{\underline{R}}_{BE} & \underline{\underline{0}} \\ \underline{\underline{0}} & \underline{\underline{R}}_{BE} \end{bmatrix} & \underline{\delta}_i &= \begin{bmatrix} \ddot{\underline{\delta}}_P \\ \ddot{\underline{\delta}}_{\text{rot}} \end{bmatrix} & \ddot{\underline{r}}_i &= \begin{bmatrix} \ddot{\underline{r}}^E_P \\ \dot{\underline{\omega}}^E_P \end{bmatrix} \end{aligned} \tag{3.19}$$

The equations at nodal level become thus:

$$\begin{cases} \ddot{\underline{r}}_i = \underline{\underline{\tilde{I}}}_i \ddot{\underline{r}}_{EB} + \underline{\underline{\tilde{r}}}_i \dot{\underline{\omega}}_{EB} + \underline{\underline{\Omega}}_i \underline{\underline{\Omega}}_i \underline{r}_i + 2\underline{\underline{\Omega}}_i \underline{\underline{R}}_i \dot{\underline{\delta}}_i + \underline{\underline{R}}_i \ddot{\underline{\delta}}_i \\ \dot{\underline{r}}_i = \underline{\underline{\tilde{I}}}_i \dot{\underline{r}}_{EB} + \underline{\underline{\tilde{r}}}_i \underline{\omega}_{EB} + \underline{\underline{R}}_i \dot{\underline{\delta}}_i \end{cases} \tag{3.20}$$

MATRIX SYSTEM FOR MULTIPLE NODES

To obtain the system for multiple nodes, thus describing the dynamics of free structures, Eq. 3.20 is to be stacked for N nodes:

$$\begin{cases} \underline{\ddot{r}} = \underline{\underline{\tilde{I}}}\,\underline{\ddot{r}}_{EB} + \underline{\underline{\tilde{r}}}\,\underline{\dot{\omega}}_{EB} + \underline{\underline{\Omega}}\,\underline{\underline{\Omega}}\,\underline{r} + 2\underline{\underline{\Omega}}\,\underline{\underline{R}}\,\underline{\dot{\delta}} + \underline{\underline{R}}\,\underline{\ddot{\delta}} \\ \underline{\dot{r}} = \underline{\underline{\tilde{I}}}\,\underline{\dot{r}}_{EB} + \underline{\underline{\tilde{r}}}\,\underline{\omega}_{EB} + \underline{\underline{R}}\,\underline{\dot{\delta}} \end{cases} \tag{3.21}$$

or in a more convenient format for the derivation of the structural equations of motion:

$$\underline{\ddot{r}} = \begin{bmatrix} \underline{\underline{R}} & \underline{\underline{\tilde{I}}} & \underline{\underline{\tilde{r}}} \end{bmatrix} \begin{bmatrix} \underline{\ddot{\delta}} \\ \underline{\ddot{r}}_{EB} \\ \underline{\dot{\omega}}_{EB} \end{bmatrix} + \underline{\underline{\Omega}}\,\underline{\underline{\Omega}}\,\underline{r} + 2\underline{\underline{\Omega}}\,\underline{\underline{R}}\,\underline{\dot{\delta}} \tag{3.22}$$

and

$$\underline{\dot{r}} = \begin{bmatrix} \underline{\underline{R}} & \underline{\underline{\tilde{I}}} & \underline{\underline{\tilde{r}}} \end{bmatrix} \begin{bmatrix} \underline{\dot{\delta}} \\ \underline{\dot{r}}_{EB} \\ \underline{\omega}_{EB} \end{bmatrix} \tag{3.23}$$

EQUATIONS OF MOTION

In the inertial frame (earth-fixed), the dynamics of a body can be written in the standard format:

$$\underline{\underline{M}}\,\underline{\ddot{r}} + \underline{\underline{K}}\,\underline{r} = \underline{f} \tag{3.24}$$

For a flexible body, the equation is also valid with exception that the position and acceleration are a function of the deformations. Note that $\underline{\underline{M}}$ and $\underline{\underline{K}}$ are also to be written in the inertial frame using the standard transformation:

$$\begin{cases} \underline{\underline{M}} = \underline{\underline{R}}\,\underline{\underline{M}}_B\,\underline{\underline{R}}^T \\ \underline{\underline{K}} = \underline{\underline{R}}\,\underline{\underline{K}}_B\,\underline{\underline{R}}^T \end{cases} \tag{3.25}$$

By using the expression derived for $\underline{\ddot{r}}$ and $\underline{r}$ as a function of both the rigid, $\underline{r}_{EB}$ and $\underline{\omega}_{EB}$, and flexible degrees of freedom, $\underline{\delta}$, we have:

$$\underline{\underline{M}} \left\{ \begin{bmatrix} \underline{\underline{R}} & \underline{\underline{\tilde{I}}} & \underline{\underline{\tilde{r}}} \end{bmatrix} \begin{bmatrix} \underline{\ddot{\delta}} \\ \underline{\ddot{r}}_{EB} \\ \underline{\dot{\omega}}_{EB} \end{bmatrix} + \underline{\underline{\Omega}}\,\underline{\underline{\Omega}}\,\underline{r} + 2\underline{\underline{\Omega}}\,\underline{\underline{R}}\,\underline{\dot{\delta}} \right\} + \underline{\underline{K}} \left\{ \underline{r}_{EB} + \underline{\underline{R}}_{BE}\underline{r}_{P_0} + \underline{\underline{R}}_{BE}\underline{\delta} \right\} = \underline{\underline{R}}\,\underline{f} \tag{3.26}$$

By pre-multiplying both sides of the equation by $\begin{bmatrix} \underline{\underline{R}} & \underline{\underline{\tilde{I}}} & \underline{\underline{\tilde{r}}} \end{bmatrix}^T$ (so that it becomes square), the following terms are derived.

Mass Matrix
The mass matrix of the coupled system is given by the following matrix operation:

$$\underline{\underline{M}}_s = \begin{bmatrix} \underline{\underline{R}} & \underline{\tilde{I}} & \underline{\tilde{r}} \end{bmatrix}^T \underline{\underline{M}} \begin{bmatrix} \underline{\underline{R}} & \underline{\tilde{I}} & \underline{\tilde{r}} \end{bmatrix} \tag{3.27}$$

equivalent to:

$$\underline{\underline{M}}_s = \begin{bmatrix} \underline{\underline{R}}^T \underline{\underline{M}} \underline{\underline{R}} & \underline{\underline{R}}^T \underline{\underline{M}} \underline{\tilde{I}} & \underline{\underline{R}}^T \underline{\underline{M}} \underline{\tilde{r}} \\ \underline{\tilde{I}}^T \underline{\underline{M}} \underline{\underline{R}} & \underline{\tilde{I}}^T \underline{\underline{M}} \underline{\tilde{I}} & \underline{\tilde{I}}^T \underline{\underline{M}} \underline{\tilde{r}} \\ \underline{\tilde{r}}^T \underline{\underline{M}} \underline{\underline{R}} & \underline{\tilde{r}}^T \underline{\underline{M}} \underline{\tilde{I}} & \underline{\tilde{r}}^T \underline{\underline{M}} \underline{\tilde{r}} \end{bmatrix} \tag{3.28}$$

Note that the term $\underline{\underline{R}}^T \underline{\underline{M}} \underline{\underline{R}}$ is nothing other than the mass matrix in the body-fixed frame of reference indicated as $\underline{\underline{M}}_B$, while the term $\underline{\tilde{I}}^T \underline{\underline{M}} \underline{\tilde{I}}$ is a diagonal matrix with the total mass of the structure and $\underline{\tilde{r}}^T \underline{\underline{M}} \underline{\tilde{r}}$ its total inertia. A more elaborated discussion on these quantities is presented when discussing the solution to the equations of motion.

Stiffness Matrix
The stiffness matrix of the coupled system is given by:

$$\underline{\underline{K}}_s = \begin{bmatrix} \underline{\underline{R}} & \underline{\tilde{I}} & \underline{\tilde{r}} \end{bmatrix}^T \underline{\underline{K}} \tag{3.29}$$

equivalent to:

$$\underline{\underline{K}}_s^T = \begin{bmatrix} \underline{\underline{R}}^T \underline{\underline{K}} \\ \underline{\tilde{I}}^T \underline{\underline{K}} \\ \underline{\tilde{r}}^T \underline{\underline{K}} \end{bmatrix} = \begin{bmatrix} \underline{\underline{R}}^T \underline{\underline{R}} \underline{\underline{K}}_B \underline{\underline{R}}^T \\ \underline{\tilde{I}}^T \underline{\underline{R}} \underline{\underline{K}}_B \underline{\underline{R}}^T \\ \underline{\tilde{r}}^T \underline{\underline{R}} \underline{\underline{K}}_B \underline{\underline{R}}^T \end{bmatrix} \tag{3.30}$$

The expression can be futher simplified as follows by looking at each term individually.

1. $\underline{\underline{R}}^T \underline{\underline{R}} \underline{\underline{K}}_B \underline{\underline{R}}^T$: from the properties of rotation matrices, one derives that $\underline{\underline{R}}^T \underline{\underline{R}} = \underline{\underline{I}}$, with $\underline{\underline{I}}$ being the identity matrix in this case. Fom this follows:

$$\underline{\underline{R}}^T \underline{\underline{R}} \underline{\underline{K}}_B \underline{\underline{R}}^T = \underline{\underline{I}} \underline{\underline{K}}_B \underline{\underline{R}}^T \tag{3.31}$$

   Note that the stiffness terms multiplies $\underline{\delta}$ which is given in the inertial frame. By pre-multiplying the deformation in the earth-fixed frame by $\underline{\underline{R}}^T$ the deformation in the body-fixed frame is obtained. In this case, the first term of the stiffness matrix is only $\underline{\underline{K}}_0$ (body-fixed frame).

2. $\underline{\tilde{I}}^T \underline{\underline{R}} \underline{\underline{K}}_B \underline{\underline{R}}^T$: breaking down this multiplication term by term, one derives:

$$\begin{bmatrix} \underline{\underline{I}} & \underline{\underline{0}} \end{bmatrix} \begin{bmatrix} \underline{\underline{R}} & \underline{\underline{0}} \\ \underline{\underline{0}} & \underline{\underline{R}} \end{bmatrix} \begin{bmatrix} \underline{\underline{0}} & \underline{\underline{0}} \\ \underline{\underline{0}} & \underline{\underline{K}} \end{bmatrix} = \begin{bmatrix} \underline{\underline{R}} & \underline{\underline{0}} \end{bmatrix} \begin{bmatrix} \underline{\underline{0}} & \underline{\underline{0}} \\ \underline{\underline{0}} & \underline{\underline{K}} \end{bmatrix} \equiv \begin{bmatrix} \underline{\underline{0}} \\ \underline{\underline{0}} \end{bmatrix} \tag{3.32}$$

3. $\underline{\underline{\tilde{r}}}^T \underline{\underline{R}}\,\underline{\underline{K}}_B\underline{\underline{R}}^T$: following the same logic as for the second term, it can be demonstrated that this term is also zero.

The stiffness term is thus:

$$\underline{\underline{K}}_s = \begin{bmatrix} \underline{\underline{K}}_B & \underline{\underline{0}} & \underline{\underline{0}} \end{bmatrix} \tag{3.33}$$

Acceleration Forces
The acceleration forces are given by:

$$\underline{f}_{\text{acc}} = \begin{bmatrix} \underline{\underline{R}} & \underline{\underline{\tilde{I}}} & \underline{\underline{\tilde{r}}} \end{bmatrix}^T \underline{\underline{M}} \left(\underline{\underline{\Omega}}\,\underline{\underline{\Omega}}\,\underline{r} + 2\underline{\underline{\Omega}}\,\underline{\underline{R}}\,\dot{\underline{\delta}} \right) \tag{3.34}$$

These forces are only of interest for non-linear maneuvers at high-speed. In most aeroelastic simulations the magnitude of aerodynamic loads is of several orders higher than acceleration forces thus justifying not taking these forces into account, [2].

External Forces
The external forces can be written as:

$$\underline{f}_s^T = \begin{bmatrix} \underline{f} & \underline{\underline{\tilde{I}}}^T \underline{\underline{R}}\,\underline{f} & \underline{\underline{\tilde{r}}}^t \underline{\underline{R}}\,\underline{f} \end{bmatrix} \tag{3.35}$$

EOM in Matrix Form
Summarizing all the relationships, the equations of motion can be written in matrix form as:

$$\begin{bmatrix} \underline{\underline{R}}^T \underline{\underline{M}}\,\underline{\underline{R}} & \underline{\underline{R}}^T \underline{\underline{M}}\,\underline{\underline{\tilde{I}}} & \underline{\underline{R}}^T \underline{\underline{M}}\,\underline{\underline{\tilde{r}}} \\ \underline{\underline{\tilde{I}}}^T \underline{\underline{M}}\,\underline{\underline{R}} & \underline{\underline{\tilde{I}}}^T \underline{\underline{M}}\,\underline{\underline{\tilde{I}}} & \underline{\underline{\tilde{I}}}^T \underline{\underline{M}}\,\underline{\underline{\tilde{r}}} \\ \underline{\underline{\tilde{r}}}^T \underline{\underline{M}}\,\underline{\underline{R}} & \underline{\underline{\tilde{r}}}^T \underline{\underline{M}}\,\underline{\underline{\tilde{I}}} & \underline{\underline{\tilde{r}}}^T \underline{\underline{M}}\,\underline{\underline{\tilde{r}}} \end{bmatrix} \begin{bmatrix} \ddot{\underline{\delta}} \\ \ddot{\underline{r}}_{EB} \\ \dot{\underline{\omega}}_{EB} \end{bmatrix} + \begin{bmatrix} \underline{\underline{K}}_B & \underline{\underline{0}} & \underline{\underline{0}} \\ \underline{\underline{0}} & \underline{\underline{0}} & \underline{\underline{0}} \\ \underline{\underline{0}} & \underline{\underline{0}} & \underline{\underline{0}} \end{bmatrix} \begin{bmatrix} \underline{\delta} \\ \underline{r}_{EB} \\ \underline{\theta}_{EB} \end{bmatrix} = \begin{bmatrix} \underline{f} \\ \underline{\underline{\tilde{I}}}^T \underline{\underline{R}}\,\underline{f} \\ \underline{\underline{\tilde{r}}}^t \underline{\underline{R}}\,\underline{f} \end{bmatrix} \tag{3.36}$$

The system cannot be solved as is due to a rank deficiency caused by the addition of the six rigid degrees of freedom. There are two ways to obviate the problem, namely *(1)* fixed-axes approximation or *(2)* mean-axes approximation. In the *fixed-axes* approximation, the flexible degrees of freedom of one reference point (node) are zeroed. In the *mean-axes* approximation, the inertial coupling between the rigid and flexible motion is minimized. In mean-axes, the equation of motion becomes:

$$\begin{bmatrix} \underline{\underline{R}}^T \underline{\underline{M}}\,\underline{\underline{R}} & \underline{\underline{R}}^T \underline{\underline{M}}\,\underline{\underline{\tilde{I}}} & \underline{\underline{R}}^T \underline{\underline{M}}\,\underline{\underline{\tilde{r}}} \\ \underline{\underline{0}} & \underline{\underline{\tilde{I}}}^T \underline{\underline{M}}\,\underline{\underline{\tilde{I}}} & \underline{\underline{0}} \\ \underline{\underline{0}} & \underline{\underline{0}} & \underline{\underline{\tilde{r}}}^T \underline{\underline{M}}\,\underline{\underline{\tilde{r}}} \end{bmatrix} \begin{bmatrix} \ddot{\underline{\delta}} \\ \ddot{\underline{r}}_{EB} \\ \dot{\underline{\omega}}_{EB} \end{bmatrix} + \begin{bmatrix} \underline{\underline{K}}_B & \underline{\underline{0}} & \underline{\underline{0}} \\ \underline{\underline{0}} & \underline{\underline{0}} & \underline{\underline{0}} \\ \underline{\underline{0}} & \underline{\underline{0}} & \underline{\underline{0}} \end{bmatrix} \begin{bmatrix} \underline{\delta} \\ \underline{r}_{EB} \\ \underline{\theta}_{EB} \end{bmatrix} = \begin{bmatrix} \underline{f} \\ \underline{\underline{\tilde{I}}}^T \underline{\underline{R}}\,\underline{f} \\ \underline{\underline{\tilde{r}}}^t \underline{\underline{R}}\,\underline{f} \end{bmatrix} \tag{3.37}$$

The same conclusion can be drawn by using a Lagrangian method and then applying the mean-axes approximation. From the definition of the kinetic energy as a function of both the flexible and rigid states, the mass and stiffness matrices can be derived, as well as the additional force terms. The Langrangian method is presented in details in Appendix B.

3.1.3. VERIFICATION

The goal of this verification study is to gauge the accuracy of the lo-fi **beam** model for structural dynamics of free-free structures against NASTRAN®. The clamped-free structural model will also be looked as a benchmark for the free-free responses and the accuracy of the flight dynamic module.

The definition of a *successful* verification is given in terms of average and maximum error, with an average error less or equal than(to) 5% with a maximum error less or equal than(to) 10%. The verification is performed looking at the modal response of the structural model which targets both stiffness and mass matrices. The lowest frequency modes are compared in terms of frequency and mode shape. The accuracy of the mode shape is quantified by means of the Modal Assurance Criterion (MAC) which is a way to compare the shape of two vectors regardless of any scaling factors. Given two eigenvectors $\underline{\phi_1}$ and $\underline{\phi_2}$, the MAC is defined as:

$$\mathrm{MAC}_{12} = \frac{\left(\underline{\phi_1}^T \underline{\phi_2}\right)^2}{(\underline{\phi_1}^T \underline{\phi_1})(\underline{\phi_2}^T \underline{\phi_2})} \tag{3.38}$$

It assumes values between 0 and 1, where 0 is no correlation and 1 is 100% correlation of the mode shapes. The following criteria , taken from Siemens PLM standard practices [3], will be used to interpret the MAC results of this verification:

- $0\% \leq \mathrm{MAC} < 50\%$: no correlation
- $50\% \leq \mathrm{MAC} < 60\%$: low correlation
- $60\% \leq \mathrm{MAC} < 80\%$: acceptable correlation
- $80\% \leq \mathrm{MAC} \leq 100\%$: great correlation

Modes with correlation higher than 60%, preferrably in the range between 80-100%, are accepted. Mode shapes of complex wing geometry, with both geometrical as well as material coupling, tend not to have a clear modal separation and can display a linear combination of the standard structural modes making it more difficult to track a particular modal response. The classic first out-of-plane bending is likely to be mixed with elements of torsional modes, or chordwise bending modes depending on the degree of coupling induced by the structure. In particular the geometric coupling ties bending and torsion together, while the material coupling can also involve other responses. What is important for aeroelastic prediction is to capture the predominant modal behaviour together with its frequency.

Throughout the verification the following nomenclature referring to the lowest frequency structural modes will be used:

I,II,III,...,X : the roman numbers indicate the order of a particular mode,

1,2,3,...,10 : the arabic numbers indicate the extraction order of a particular mode as a result of an eigenvalue problem,

O : indicates *out-of-plane*, more specifically the relevant mode shape is in the YZ plane, with Y being the spanwise direction and Z the vertical,

C : indicates that the mode is *chord-wise*, more specifically the relevant mode shape in in the XY plane, with X being the chorwise direction and Y the spanwise direction,

B : indicates a predominantly *bending* mode,

T : indicates a predominantly *torsional* mode,

HO : indicates a *higher-order* mode.

NASTRAN® Veritication Model

Before moving on to the verification cases, the NASTRAN® verification model is briefly presented. The NASTRAN® verification model describes the composite structure of the CRM aircraft. For more information on the geometric properties, the interested reader is referred to Appendix C. It is important to remember that we are dealing with a composite beam model, where the bending-torsion coupling becomes of great importance. NASTRAN® has an internal procedure to evaluate the cross-sectional stiffness and assemble the element stiffness matrix given a set of geometric inputs and material properties. Nevertheless, there is no element formulation in the NASTRAN® library that accounts for three main aspects of the cross-sections that describe the benchmark wing, namely custom shape, material properties in lamination parameters (or the MAT2 type of formulation in NASTRAN®) and bending-torsion coupling stiffness.

For this reason, the model has been built using the general element formulation known in NASTRAN® as the GENEL card. GENEL stands for **Gen**eral **El**ement and allows to give the element stiffness matrix as an explicit input to the Nastran solver. The element format is illustrated in Tab. 3.1.

Table 3.1: Nastran GENEL card format.

GENEL	EID		UI1	CI1	UI2	CI2	UI3	CI3
	UI4	CI4	UI5	CI5	UI6	CI6	UI7	CI7
	UI8	CI8	UI9	CI9	UI10	CI10	UI11	CI11
	UI12	CI12						
	K	K11	⋯	K1212				

where EID is the element ID, UIi the node ID, and CIi identifies the degree of freedom (the number ranges from 1 to 6).

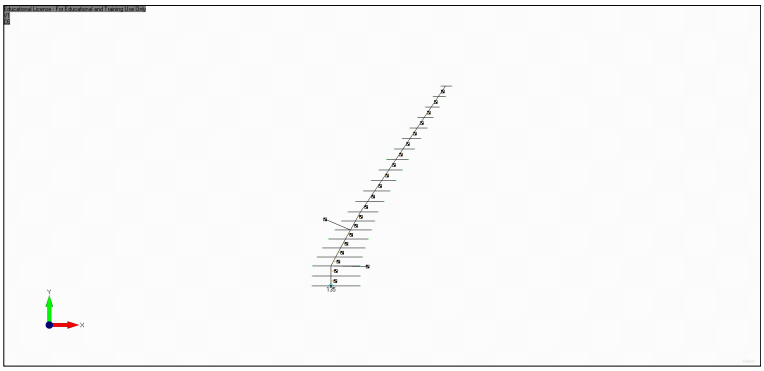

Figure 3.2: Top view of the NASTRAN® beam model of the CRM wing.

The input consists of a first part that indicates the connections between the degrees of freedom of node i and $i+1$ (extremities of the element), while the second part gives the lower triangular part of the element stiffness matrix in the global reference frame (the base in Nastran nomenclature). The element stiffness matrix suffices to perform a static analysis with SOL101 in NASTRAN®, but GENEL has no mass definition and that would prevent a modal analysis with SOL103. The structural mass has therefore been calculated from the cross-sectional shape and material properties are distributed in spanwise direction by means of NASTRAN® elements CONM2 and RBE2. The former defines a lumped mass along the span, the latter connects the degrees of freedom of that mass to the beam nodes which are independent nodes in the formulation. This approach allows to account for both mass and inertia properties of the cross-sections. The RBE2 rigid connection is also used to link the different parts in the wing-tail configuration and aircraft model. Examples of the structural models are in Fig. 3.2, 3.3, 3.4, and Appendix C.

For a representative aerodynamic model, CAERO1 cards are used. The aerodynamic loads are transferred to the structural mesh by means of SPLINE1 cards. An example of the aerodynamic mesh within the aeroelastic beam model are shown in Fig. 3.5.

Structural Modal Analysis: Wing
The modes of interest for this case are the following: *(1)* first out-of-plane bending (IOB), *(2)* second out-of-plane bending (IIOB), *(3)* first torsion combined with second out-of-plane bending (IT + IIOB), *(4)* first chordwise bending combined with second out-of-plane bending (ICB + IIOB) and finally *(5)* third out-of-plane bending (IIIOB).

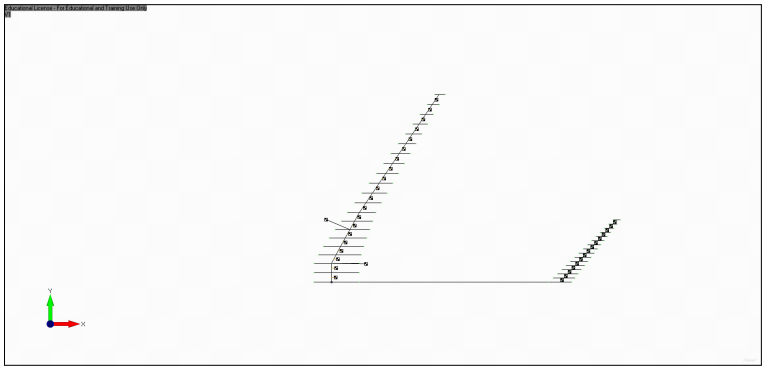

Figure 3.3: Top view of the NASTRAN® beam model of the CRM wing-tail configuration.

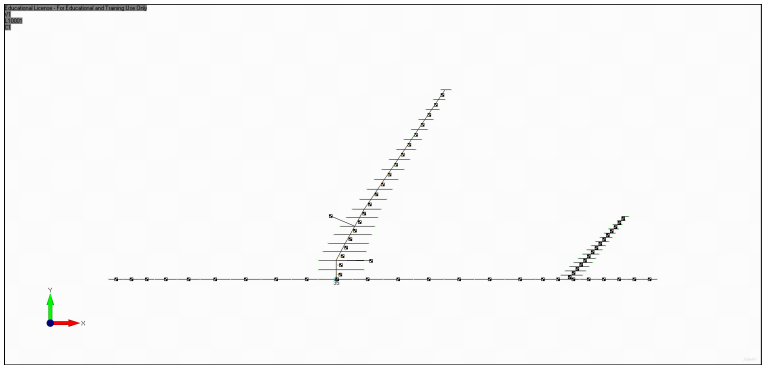

Figure 3.4: Top view of the NASTRAN® beam model of the CRM aircraft.

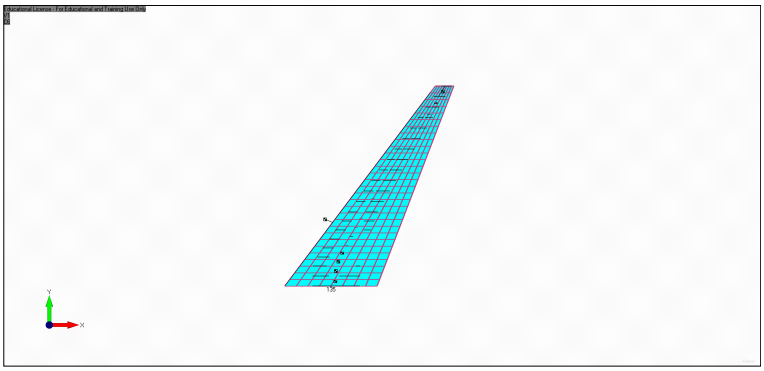

Figure 3.5: Top view of the NASTRAN® beam aeroelastic model of the CRM wing.

The frequencies are shown below in comparison with the NASTRAN® prediction. For the clamped-free case, an average error of 1.0% and a maximum error of 2.56% is made, whereas for the free-free case, 0.15% and 2.41%. The mode shapes are well correlated as can be seen in the MAC table. A summary of all shapes can be found in Fig. 3.6 and 3.7.

Tab. V.1: Frequency comparison of the CRM wing structural model.

	No.	Beam	NASTRAN®	Error (%)		Beam	NASTRAN®	Error (%)
Clamp-Free	1	1.42	1.41	0.71	Free-Free	3.13	3.10	0.97
	2	3.25	3.32	-2.11		7.28	7.46	-2.41
	3	4.56	4.68	-2.56		10.22	10.38	-1.54
	4	5.58	5.60	-0.36		13.25	13.23	0.15
	5	7.00	7.05	-0.71		15.35	15.02	2.20

Tab. V.2: MAC comparison of the CRM wing structural model.

No.		NASTRAN®						NASTRAN®				
1	Beam (Clamp)	0.99	0.46	0.11	0.02	0.01	Beam (Free)	0.99	0.26	0.05	0.05	0.06
2		0.39	0.99	0.71	0.08	0.27		0.33	0.96	0.00	0.18	0.24
3		0.21	0.77	0.98	0.00	0.49		0.12	0.04	0.99	0.22	0.03
4		0.02	0.03	0.01	0.99	0.00		0.12	0.39	0.11	0.87	0.39
5		0.14	0.53	0.56	0.03	0.87		0.13	0.33	0.00	0.41	0.95

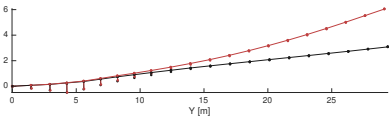

(a) Beam: 1 - I OB

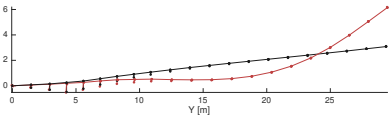

(b) Beam: 3 - I T + III OB

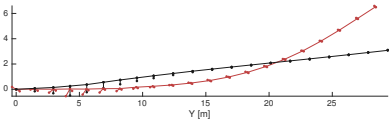

(c) Beam: 2 - II OB

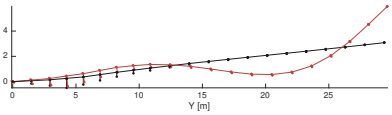

(d) Beam: 5 - III OB

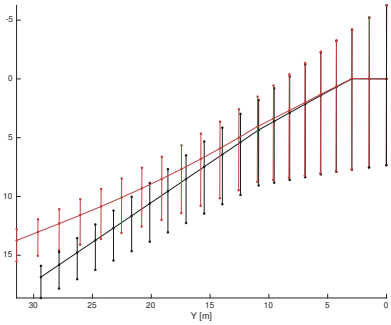

(e) Beam: 4 - I CB + II OB

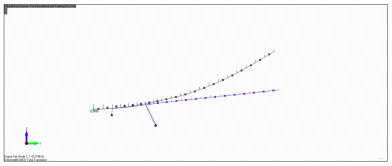

(f) NASTRAN®: 1 - I OB

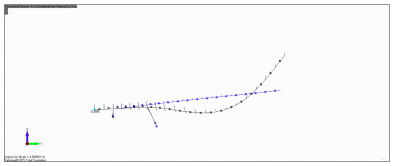

(g) NASTRAN®: 3 - I T + III OB

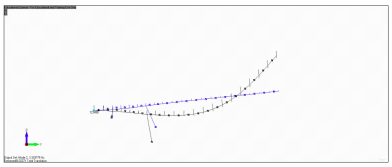

(h) NASTRAN®: 2 - II OB

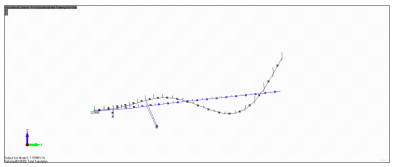

(i) NASTRAN®: 5 - III OB

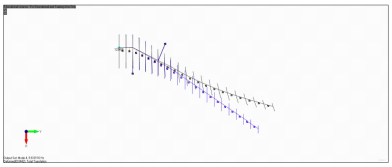

(j) NASTRAN®: 4 - I CB + II OB

Figure 3.6: Mode shapes of the clamped-free wing model in comparison.
Black lines refer to the undeformed configuration, red or blue lines to modal shape.

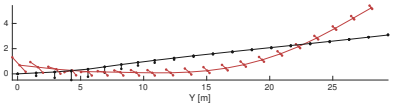

(a) Beam: 1 - I OB

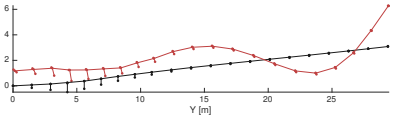

(b) Beam: 4 - I T + III OB

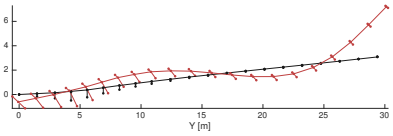

(c) Beam: 2 - II OB

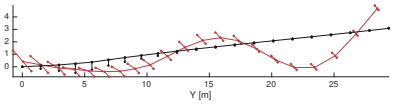

(d) Beam: 5 - III OB

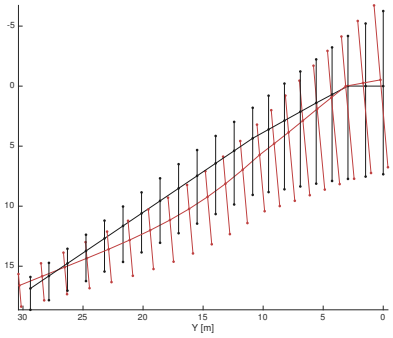

(e) Beam: 3 - I CB + III OB

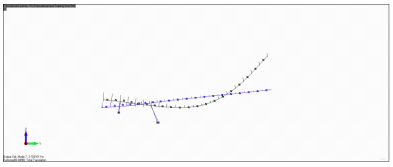

(f) NASTRAN®: 1 - I OB

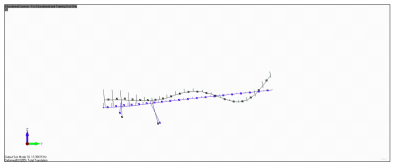

(g) NASTRAN®: 4 - I T + III OB

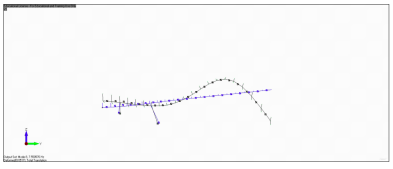

(h) NASTRAN®: 2 - II OB

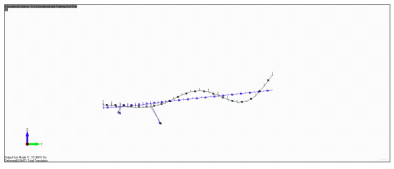

(i) NASTRAN®: 5 - III OB

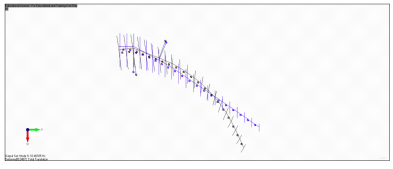

(j) NASTRAN®: 3 - I CB + III OB

Figure 3.7: Mode shapes of the free-free wing model in comparison.
Black lines refer to the undeformed configuration, red or blue lines to modal shape.

Structural Modal Analysis: Wing-Tail

The modes of interest for the free-free wing and horizontal tail configuration[1] are hereby listed. With the wing clamped at the root, and the horizontal tail rigidly attached to the wing, solving the eigenvalue problem of the wing-tail configuration is equivalent to solving the two eigenvalue problems (for wing and horizontal tail) separately. The modes of the free-free configuration involve both surfaces, generally with different responses. The annotation *(W)* will indicate the response of the wing, whereas *(HT)* the one of the horizontal tail.

Table 3.2: Overview of the mode shapes of the wing-tail configuration.

Mode No.	*(W)*	*(HT)*
1	IOB	IOB
2	IIOB	IOB
3	ICB	ICB
4	ICB	IIOB
5	IIIOB	IIOB

Both frequencies and mode shapes show excellent agreement with respect to the NASTRAN®prediction. The average error in the frequency prediction is 0.81%, with a maximum error of 2.85%. The mode shapes of the free-free wing-tail configuration are shown in Fig. 3.8.

Tab. V.3: Frequency comparison of the CRM wing-tail structural model.

	Beam	NASTRAN®	Error (%)
Free-Free	2.44	2.44	0.16
	5.00	5.11	-2.15
	6.89	6.94	-0.72
	7.41	7.30	1.51
	8.86	9.12	-2.85

Tab. V.4: MAC comparison of the CRM wing-tail structural model.

No.		NASTRAN®				
1	Beam	0.96	0.01	0.11	0.15	0.01
2		0.04	0.91	0.07	0.05	0.02
3		0.07	0.02	0.90	0.04	0.00
4		0.18	0.14	0.21	0.86	0.02
5		0.02	0.18	0.01	0.04	0.87

[1] Note that the two parts are linked with a rigid element, equivalent to a NASTRAN® RBE2 element.

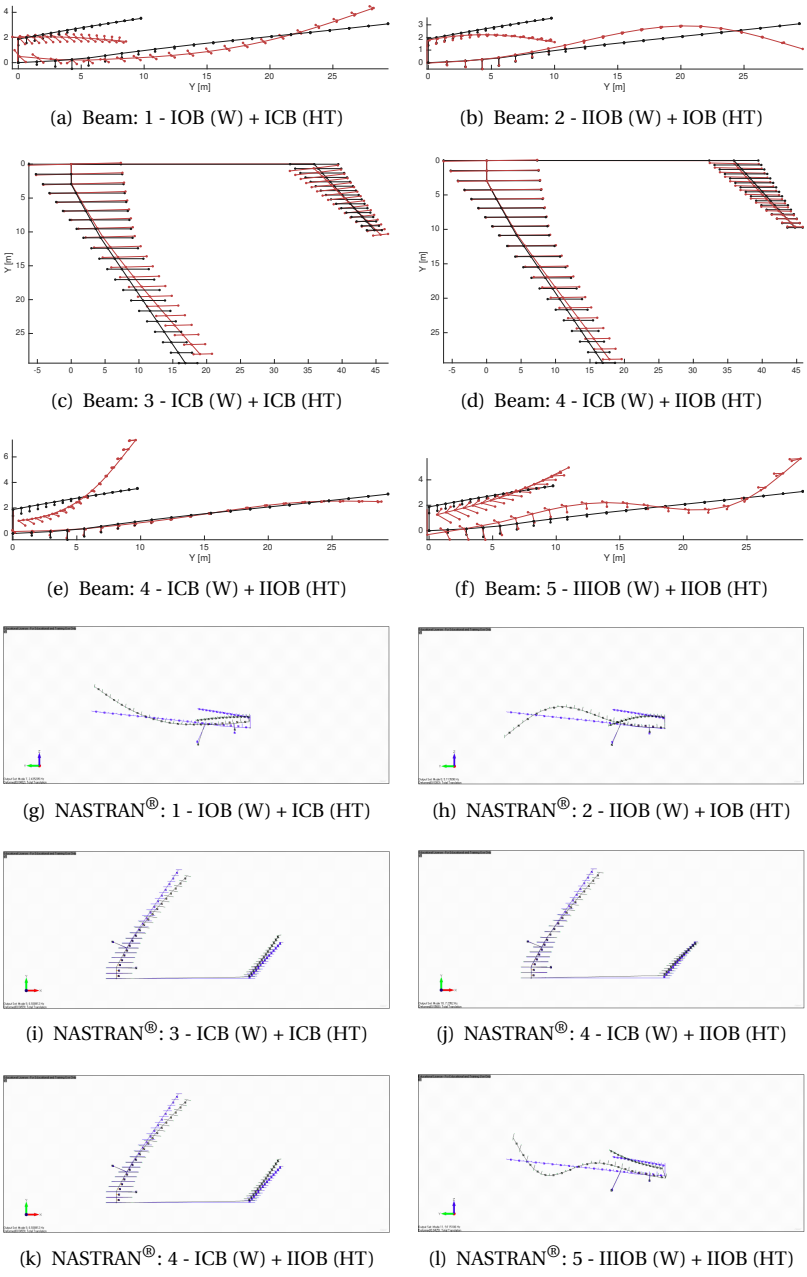

(a) Beam: 1 - IOB (W) + ICB (HT)

(b) Beam: 2 - IIOB (W) + IOB (HT)

(c) Beam: 3 - ICB (W) + ICB (HT)

(d) Beam: 4 - ICB (W) + IIOB (HT)

(e) Beam: 4 - ICB (W) + IIOB (HT)

(f) Beam: 5 - IIIOB (W) + IIOB (HT)

(g) NASTRAN®: 1 - IOB (W) + ICB (HT)

(h) NASTRAN®: 2 - IIOB (W) + IOB (HT)

(i) NASTRAN®: 3 - ICB (W) + ICB (HT)

(j) NASTRAN®: 4 - ICB (W) + IIOB (HT)

(k) NASTRAN®: 4 - ICB (W) + IIOB (HT)

(l) NASTRAN®: 5 - IIIOB (W) + IIOB (HT)

Figure 3.8: Mode shapes of the free-free wing-tail model in comparison.
Black lines refer to the undeformed configuration, red or blue lines to modal shape.

Structural Modal Analysis: Aircraft

The modal comparison for the flexible aircraft (symmetric) is also performed on the free-free model. The modes of interest are hereby given, indicating the response of wing *(W)*, horizontal tail *(HT)* and fuselage *(F)* in each mode.

Table 3.3: Overview of the mode shapes of the aircraft structural model.

Mode No.	*(W)*	*(HT)*	*(F)*
1	IOB	IOB	Elevation
2	IOB + ICB	IOB	IOB
3	IOB	IOB	IOB
4	IIOB	IOB	Pitch
5	IIOB	IIOB	IIOB
6	IIOB + IICB	IIOB	IIOB

The error on the frequency prediction averages at 0.83%, with its maximum value being 4.19% on Mode No. 2, as can be seen in the table below.

Tab. V.5: Frequency comparison of the CRM aircraft structural model.

	No.	Beam	NASTRAN®	Error (%)
Free-Free	1	1.91	1.98	-3.54
	2	3.73	3.58	4.19
	3	4.18	4.17	0.24
	4	4.90	5.06	-3.16
	5	5.57	5.68	-1.94
	6	6.37	6.44	-1.09

The Modal Assurance Criterion also indicates great modal correlation across the different responses with low degrees of cross correlation. The mode shapes can be found in Fig. 3.9 and 3.10

Tab. V.6: MAC comparison of the CRM aircraft structural model.

No.		NASTRAN®					
1	Beam	0.96	0.00	0.01	0.21	0.02	0.00
2		0.00	0.98	0.05	0.00	0.23	0.00
3		0.00	0.03	0.95	0.00	0.53	0.16
4		0.32	0.05	0.29	0.89	0.26	0.00
5		0.00	0.25	0.49	0.00	0.86	0.03
6		0.00	0.00	0.26	0.00	0.01	0.94

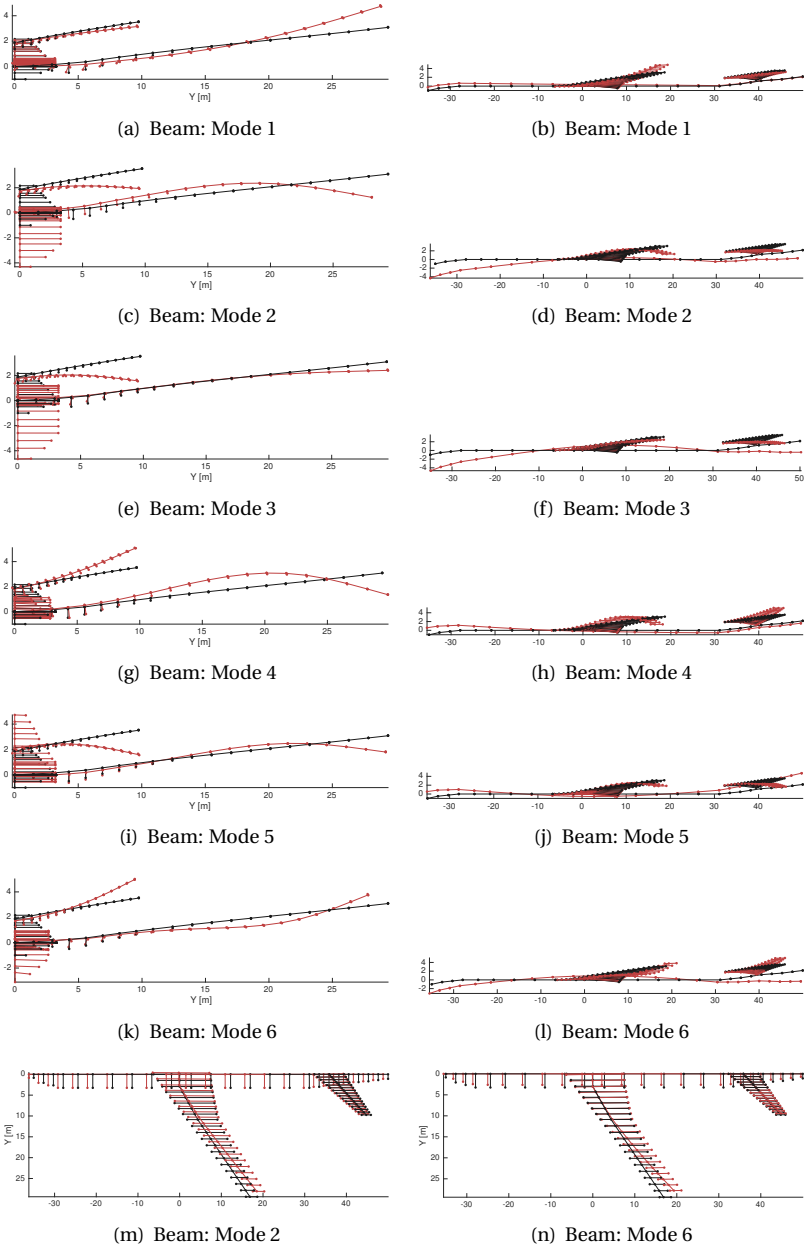

(a) Beam: Mode 1

(b) Beam: Mode 1

(c) Beam: Mode 2

(d) Beam: Mode 2

(e) Beam: Mode 3

(f) Beam: Mode 3

(g) Beam: Mode 4

(h) Beam: Mode 4

(i) Beam: Mode 5

(j) Beam: Mode 5

(k) Beam: Mode 6

(l) Beam: Mode 6

(m) Beam: Mode 2

(n) Beam: Mode 6

Figure 3.9: Mode shapes of the free-free wing-tail model predicted by the method in this dissertation. **Black** lines refer to the undeformed configuration, red lines to modal shape.

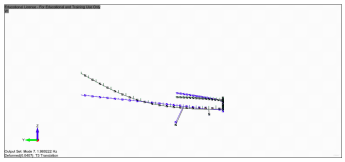

(a) NASTRAN®: Mode 1

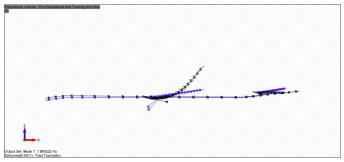

(b) NASTRAN®: Mode 1

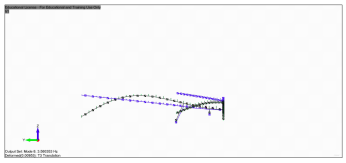

(c) NASTRAN®: Mode 2

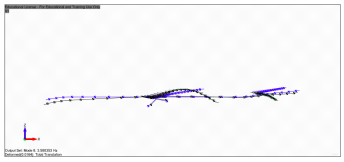

(d) NASTRAN®: Mode 2

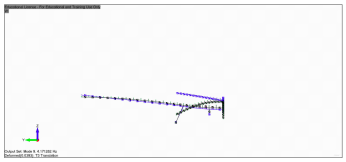

(e) NASTRAN®: Mode 3

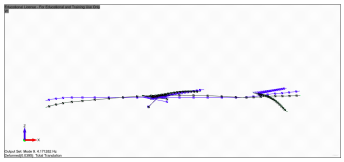

(f) NASTRAN®: Mode 3

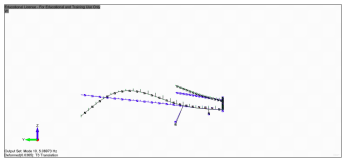

(g) NASTRAN®: Mode 4

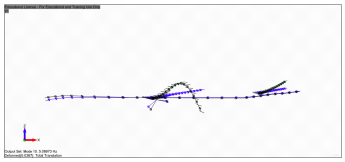

(h) NASTRAN®: Mode 4

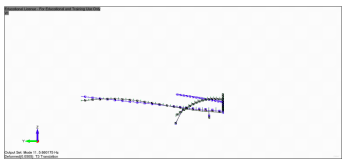

(i) NASTRAN®: Mode 5

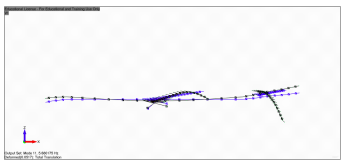

(j) NASTRAN®: Mode 5

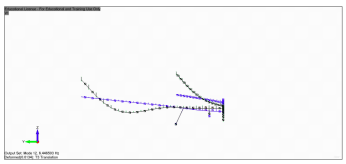

(k) NASTRAN®: Mode 6

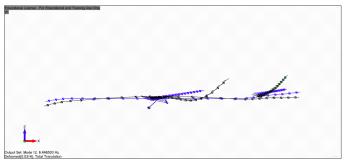

(l) NASTRAN®: Mode 6

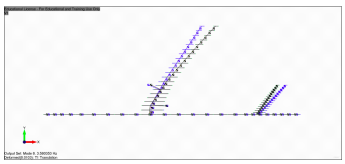

(m) NASTRAN®: Mode 2

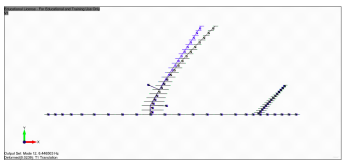

(n) NASTRAN®: Mode 6

Figure 3.10: Mode shapes of the free-free wing-tail model in predicted by NASTRAN®.
Black lines refer to the undeformed configuration, blue lines to modal shape.

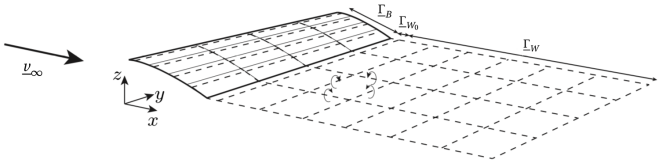

Figure 3.11: Visual description of the aerodynamic mesh and some of the relevant quantities for the derivation of the aerodynamic state space, [1].

3.2. AERODYNAMIC MODEL

This section presents important aspects regarding the aerodynamic model of a full aircraft configuration. An extensive derivation of the unsteady vortex-lattice method (UVLM) is found in [1]. In Sec. 3.2.1, the generic aerodynamic state space will be rewritten, derived in [1] for the case of a double lifting surface. The fuselage aerodynamic model is discussed in Sec. 3.2.3. The two models are then combined in Sec. 3.2.4.

3.2.1. DOUBLE LIFTING SURFACE AERODYAMICS

The aerodynamic model is written in a continuous-time, state-space model. In this model, the wake is discretized using the discontinuous Galerkin method with finite elements that geometrically coincide with the wake panels. The solution, in terms of velocity potential, is approximated by an interpolation function which is *(i)* continuous within the element but *(ii)* discontinuous across element boundaries. Following the detailed derivation in [1], the following matrix equations for the description of the aerodynamic model are obtained,

$$\begin{cases} \underline{\underline{K}}_1\underline{\Gamma}_B + \underline{\underline{K}}_2\underline{\Gamma}_{W_0} + \underline{\underline{K}}_3\underline{\Gamma}_W = -\underline{v}_\infty \cdot \underline{n} & : \text{Flow Tangency} \\ \underline{\underline{K}}_4\underline{\Gamma}_B + \underline{\underline{K}}_5\underline{\Gamma}_{W_0} = 0 & : \text{Kutta Condition} \\ \dot{\underline{\Gamma}}_W = \underline{\underline{K}}_6\underline{\Gamma}_W + \underline{\underline{K}}_7\underline{\Gamma}_{W_0} & : \text{Helmholtz Theorem} \end{cases} \tag{3.39}$$

where subscript B indicates the body of the lifting surface, W_0 the first row of the wake panels (where the velocity is equal to the velocity of the trailing edge of the lifting surface) and W the remaining wake panels. Note also that $\underline{v}$ and $\underline{v}_\infty$ indicate velocity vectors, $\underline{n}$ the normal vector of the aerodynamic panels and V_∞ the scalar flow velocity

At this point an important assumption is made to simplify the equations and write the state space system, namely: the velocity perturbation is assumed small compared to the flow velocity v_∞. This allows to rewrite the flow tangency condition for one lifting surface (e.g. wing) as:

$$\underline{\underline{K}}_1\underline{\Gamma}_B + \underline{\underline{K}}_2\underline{\Gamma}_{W_0} + \underline{\underline{K}}_3\underline{\Gamma}_W = -\underline{v}_\infty \cdot \underline{n} - V_\infty n_z \alpha - \underline{v}_\infty \Delta n + \underline{v}_B \cdot \underline{n} \equiv \underline{\underline{B}}_1 \alpha + \underline{\underline{B}}_2 \tag{3.40}$$

or in case of two lifting surfaces (e.g. wing and horizontal tail):

$$\underline{\underline{K}}_1\underline{\Gamma}_B + \underline{\underline{K}}_2\underline{\Gamma}_{W_0} + \underline{\underline{K}}_3\underline{\Gamma}_W = -\underline{v}_\infty \cdot \underline{n} - v_\infty n_z \alpha - \underline{v}_\infty \Delta n + \underline{v}_B \cdot \underline{n} \equiv \underline{\underline{B}}_{1,1}\underline{\alpha_1} + \underline{\underline{B}}_{1,2}\underline{\alpha_2} + \underline{\underline{B}}_2 \tag{3.41}$$

From this equation, one can derive $\underline{\Gamma}_B$ as:

$$\underline{\Gamma}_B = \underline{\underline{K}}_1^{-1}\left(-\underline{\underline{K}}_2\underline{\Gamma}_{W_0} - \underline{\underline{K}}_3\underline{\Gamma}_W + \underline{\underline{B}}_{1,1}\underline{\alpha}_1 + \underline{\underline{B}}_{1,2}\underline{\alpha}_2 + \underline{\underline{B}}_2\right) \tag{3.42}$$

substituting it into the Kutta condition to isolate $\underline{\Gamma}_{W_0}$ as a function of $\underline{\Gamma}_W$:

$$\underline{\Gamma}_{W_0} = \left(\underline{\underline{K}}_5 - \underline{\underline{K}}_4\underline{\underline{K}}_1^{-1}\underline{\underline{K}}_2\right)^{-1}\underline{\underline{K}}_4\underline{\underline{K}}_1^{-1}\left(\underline{\underline{K}}_3\underline{\Gamma}_W - \underline{\underline{B}}_{1,2}\underline{\alpha}_1 - \underline{\underline{B}}_{1,2}\underline{\alpha}_2 - \underline{\underline{B}}_2\right) \tag{3.43}$$

and finally in the Helmholtz theorem to obtain the final input equation of the state space:

$$\dot{\underline{\Gamma}}_W = \underline{\underline{K}}_8\underline{\Gamma}_W + \underline{\underline{K}}_{9,1}\underline{\alpha}_1 + \underline{\underline{K}}_{9,2}\underline{\alpha}_2 + \underline{\underline{K}}_{10} \tag{3.44}$$

with:

$$\begin{cases} \underline{\underline{K}}_8 = \underline{\underline{K}}_6 + \underline{\underline{K}}_7\left(\underline{\underline{K}}_5 - \underline{\underline{K}}_4\underline{\underline{K}}_1^{-1}\underline{\underline{K}}_2\right)^{-1}\underline{\underline{K}}_4\underline{\underline{K}}_1^{-1}\underline{\underline{K}}_3 \\ \underline{\underline{K}}_{9,i} = -\underline{\underline{K}}_7\left(\underline{\underline{K}}_5 - \underline{\underline{K}}_4\underline{\underline{K}}_1^{-1}\underline{\underline{K}}_2\right)^{-1}\underline{\underline{K}}_4\underline{\underline{K}}_1^{-1}\underline{\underline{B}}_{1,i} \quad \text{with } i = 1,2 \\ \underline{\underline{K}}_{10} = -\underline{\underline{K}}_7\left(\underline{\underline{K}}_5 - \underline{\underline{K}}_4\underline{\underline{K}}_1^{-1}\underline{\underline{K}}_2\right)^{-1}\underline{\underline{K}}_4\underline{\underline{K}}_1^{-1}\underline{\underline{B}}_2 \end{cases} \tag{3.45}$$

For the output equation, one starts by combining the general equation in [1]:

$$\begin{Bmatrix} \underline{F} \\ \underline{M} \end{Bmatrix} = \underline{\underline{L}}_1\underline{\Gamma}_B = \underline{\underline{L}}_2\dot{\underline{\Gamma}}_B \tag{3.46}$$

with the flow tangency and Kutta condition. By adopting a similar methodology as for the input equation, the following is obtained:

$$\begin{Bmatrix} \underline{F} \\ \underline{M} \end{Bmatrix} = \underline{\underline{L}}_4\underline{\Gamma}_W + \underline{\underline{L}}_{5,1}\underline{\alpha}_1 + \underline{\underline{L}}_{5,2}\underline{\alpha}_2 + \underline{\underline{L}}_6\dot{\underline{\Gamma}}_W + \underline{\underline{L}}_{7,1}\dot{\underline{\alpha}}_1 + \underline{\underline{L}}_{7,2}\dot{\underline{\alpha}}_2 + \underline{\underline{L}}_8 \tag{3.47}$$

where:

$$\begin{cases} \underline{\underline{L}}_3 = \underline{\underline{I}} - \underline{\underline{K}}_1^{-1}\underline{\underline{K}}_2\underline{\underline{K}}_5^{-1}\underline{\underline{K}}_4 \\ \underline{\underline{L}}_4 = -\underline{\underline{L}}_1\underline{\underline{L}}_3^{-1}\underline{\underline{K}}_1^{-1}\underline{\underline{K}}_3 \\ \underline{\underline{L}}_{5,i} = \underline{\underline{L}}_1\underline{\underline{L}}_3^{-1}\underline{\underline{K}}_1^{-1}\underline{\underline{B}}_{1,i} \quad \text{with } i = 1,2 \\ \underline{\underline{L}}_6 = -\underline{\underline{L}}_1\underline{\underline{L}}_3^{-1}\underline{\underline{K}}_1^{-1}\underline{\underline{K}}_3 \\ \underline{\underline{L}}_{7,i} = \underline{\underline{L}}_1\underline{\underline{L}}_3^{-1}\underline{\underline{K}}_1^{-1}\underline{\underline{B}}_{1,i} \\ \underline{\underline{L}}_8 = \underline{\underline{L}}_1\underline{\underline{L}}_3^{-1}\underline{\underline{K}}_1^{-1}\underline{\underline{B}}_2 \end{cases} \tag{3.48}$$

It is important to note that the input to the aerodynamic system is the time derivative of the angle of attack. This is the result of assuming that the perturbation is much smaller compared to the flow velocity. This assumption is only valid in case of vertical perturbation and it is important to keep in mind when assessing the gust response of the system.

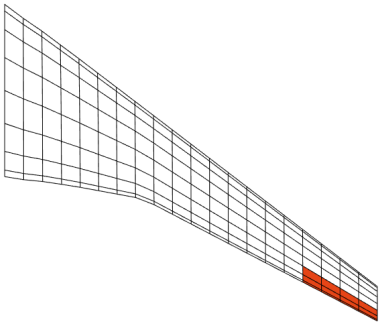

Figure 3.12: Example of a set of aerodynamic panels used as a control surface.

3.2.2. MANEUVER LOAD ALLEVIATION

The aerodynamic model, derived as shown, can be modified to include the option of maneuver load alleviation. To do this one needs to account for the control surface deflections in the calculation of the aerodynamic forces. For a particular maneuver, a set of controllers can be deflected to shift most of the lift generated under trimmed condition towards the mid-plane, thus alleviating the root bending moment. The controllers in the tip area of the wing will not be used for MLA, but rather left for the eventuality of roll control. Hereby, an analytical approach will be presented to model the control deflection of a panel-based mesh to be included in the aerodynamic state space.

Let us consider a selected area of the mesh adopted for the derivation of the aerodynamic model. This set of panels will act as a control surface thus allowing the possibility to control the lift generated in that particular area. The deflection of this control surface will be modeled by altering the normal vectors of its panels, while keeping the geometry fixed. Note that this condition implies a local violation of the flow tangency condition in the control area. The error caused by this simplification is assessed by comparing the loads with a Nastran solution.

There are two main ways to apply the control deflection to the control surface panels. Either by *(i)* rotating the panels around the global Y-axis (the axis that runs in span-wise direction), or *(ii)* rotating the panels around the local hinge axis defined by the edge of the control surface. Both approaches are valid and carry their complications, but for the purposes of this dissertation the latter has been used where the rotation is applied around the local hinge axis. This method has the added complication that the hinge line is a function of the panel coordinates, and these are altered by the elastic deflection. There is thus a dependency of the hinge line to the elastic deflection that has to be taken into account when implementing the sensitivities needed for optimization purposes.

Let us now discuss how the control deflection is modeled and applied to the set of panels that define the control surface. The edge of the controller defines the hinge axis, or in other words, its axis of rotation. The deflection is nothing other than a rotation θ

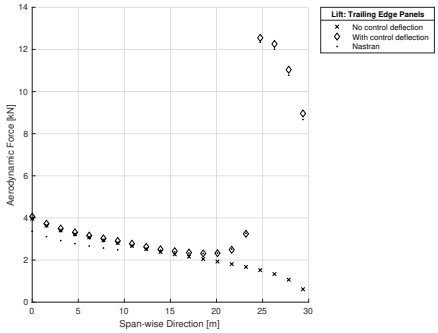

Figure 3.13: Lift generation with and without control deflection in comparison with NASTRAN®.

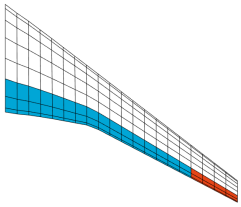

Figure 3.14: Overview of panels monitored for verification purposes.
In blue are the monitored trailing edge aerodynamic panels, in orange are the control panels.

around this axis. This allows us to define the rotation matrix with the axis-angle representation as follows. From the coordinates of the hinge line (rotation axis), defined as:

$$\{x_h,\ y_h,\ z_h\}^T = \underline{P}_2 - \underline{P}_1 \tag{3.49}$$

let us name its skew-symmetric matrix as $\underline{\underline{K}}$. Considering a deflection θ of the control surface, the associated rotation matrix is given by:

$$\underline{\underline{R}} = \underline{\underline{I}} + \underline{\underline{K}} \sin\theta + \underline{\underline{K}}^2 (1 - \cos\theta) \tag{3.50}$$

This expression is derived similarly to the Rodriguez formula, but adapted for the axis-angle formulation. With $\underline{n}_{0,i}$ being the normal at 0 degree deflection of the i^{th} panel in the control surface, the new normal can be simply derived as:

$$\underline{n}_i = \underline{\underline{R}}\, \underline{n}_{0,i} \tag{3.51}$$

This newly calculated vector can be now used for the remainder of the derivation of the aerodynamic model. The verification of the approached described in this section is shown in Fig. 3.13. In this comparison the lift generated by the panels along the trailing edge is compared to isolate the effect of the control deflection. The panels that have been monitored can be found in Fig. 3.14.

3.2.3. FUSELAGE AERODYNAMICS

The aerodynamics of the fuselage is described by means of a source panel distribution. The work by Hess et al. [4] and Katz and Plotkin [5] discusses the two main options for body aerodynamics, namely *(i)* a source distribution along the center line and *(ii)* a source distribution on the fuselage wetted surface. The first model is more appropriate for bodies of revolution, while for more complex body shapes the second one is preferred. For the purposes of this work, a source distribution on the wetted surface has been adopted.

The fuselage aerodynamics is described by potential flow theory. Flow separation, turbulence and the wake shed by the body are not included in this work. Furthermore, the source panel distribution does not allow for wake modeling. The work by Rusak et al. [6] discusses the challenges of modeling such a physical phenomenon.

The different theories behind the source distribution are given in the work by Katz and Plotkin [5]. A distribution of constrant strength source panels has been chosen to describe the aerodynamics of the fuselage. The method is based on the Laplacian of the disturbance velocity potential Φ,

$$\nabla^2 \Phi = 0 \tag{3.52}$$

with flow tangency condition,

$$\underline{\nabla}\Phi \cdot \underline{n} = 0 \tag{3.53}$$

and the far-field condition as,

$$\lim_{r \to \infty} \nabla \Phi = 0 \tag{3.54}$$

where r refers to the distance from the body. The velocity potential at an arbitrary point $\underline{P}$ due to a constant strength quadrilateral source σ is,

$$\Phi(\underline{P}) = \frac{\sigma}{4\pi} \int_s \frac{dS}{\sqrt{(x-x_0)^2 + (y-y_0)^2 + z^2}} \tag{3.55}$$

while the local velocity $\underline{u}$ can be derived from the potential Φ as,

$$\underline{u} = \frac{\partial \Phi}{\partial \underline{P}} \tag{3.56}$$

By solving Eq. 3.55, and differentiating with respect to $\underline{P}$, one can obtain the expressions for the local velocity components u, v and w in each segments, as derived in Katz and Plotkin [5],

$$\underline{u} = \{u, v, w\}^T \tag{3.57}$$

Force Calculation

Hereby the system of equations that describes the flow around the body is given. Neumann boundary conditions are adopted, with the far-field condition being satisfied by definition of the quadrilateral constant-strength source panels, and the flow tangency condition enforced. For a single panel, the flow is described by the following equation,

$$\underline{u} \cdot \underline{n} + \underline{v}_\infty \cdot \underline{n} = 0 \tag{3.58}$$

where $\underline{u}^T = \{u, v, w\}$ is the velocity at the collocation point, and $\underline{v}_\infty$ is the far-field velocity vector in the body reference frame, thus,

$$\underline{v}_\infty = \{V_\infty \cos\alpha,\ 0,\ V_\infty \sin\alpha\} \tag{3.59}$$

Applying the same logic to the rest of the body panels, the following system of equations is written,

$$\underline{\underline{A}}\,\underline{\sigma} = -\underline{B} \tag{3.60}$$

with $\underline{\underline{A}}$ being the aerodynamic influence coefficient matrix, $\underline{\sigma}$ the source strength, and $\underline{B}$ the vector with its i^{th} element being the product $(\underline{v}_i \cdot \underline{n}_i)$ for the i^{th} panel.

Once the source strength distribution is known, the panel velocities can be calculated. The equations are written for the velocity components of one panel. Assembling the equations for all the panels leads to a system of equations in matrix format for each velocity component, thus,

$$\begin{cases} \underline{u} = \underline{\underline{A}}_x\,\underline{\sigma} \\ \underline{v} = \underline{\underline{A}}_y\,\underline{\sigma} \\ \underline{w} = \underline{\underline{A}}_z\,\underline{\sigma} \end{cases} \tag{3.61}$$

where $\underline{u}$, $\underline{v}$, $\underline{w}$ are vectors containing respectively the x, y, z components of the velocity in each panel. The pressure distribution is then derived as a function of the panel velocities. The pressure coefficient is generally expressed as,

$$C_p = 1 - \frac{||\underline{u}||^2}{V_\infty^2} \tag{3.62}$$

For a single panel k, let $\underline{\underline{R}}_k$ be the transformation matrix from the body-frame to the local panel coordinates, the local velocity vector can be written as,

$$\underline{u}_k = \underline{\underline{R}}_k \left(\underline{v}_\infty + \underline{u}_k\right) \tag{3.63}$$

thus,

$$C_p = 1 - \frac{||\underline{u}_k||^2}{V_\infty} \tag{3.64}$$

The force vector $\underline{F}$, normal to the panel, is then given by,

$$\underline{F} = -\frac{1}{2}\rho_\infty C_p S V_\infty^2 \cdot \underline{n} \tag{3.65}$$

with S being the surface area.

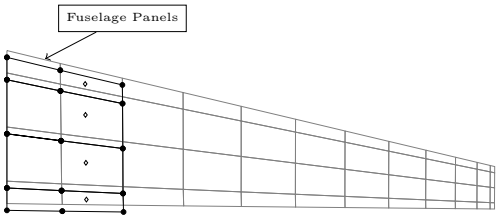

Figure 3.15: Detail of wing-fuselage intersection.
Legend ◇: collocation points, **o**: corner points, **black lines**: fuselage panels, gray lines: wing panels.

WING-BODY INTERACTION PROBLEM

Interrupting the wing at the fuselage intersection would result in a discontinuity in the vortex distribution which will not end at the symmetry plane. The discontinuity will lead to a strong vortex being generated at the root of the wing, that is not counteracted by its symmetric part thus influencing the neighbouring body panels. This condition is also not realistic since a vortex at the midplane is not representative of the physical phenomena.

A possible solution is discussed by Rusak et al. [6] which entails extending the wing panels to the midplane. The extension of the panels will immediately solve the problem of the discontinuity at the midplane shedding no extra vortices within the body. The tangency condition is omitted from the wing panels within the body, and the collocation point is removed. This modification to describe the physics of the wing-body interaction is illustrated in Fig. 3.15.

VERIFICATION WITH LITERATURE

The implementation has been validated against the work by Singh et al. [7], proving both analytical and experimental reference results on the model shown in Fig. 3.16(a), with the wing located at 4.0 m along the fuselage symmetry line. The wing is rectangular with a 8.8 m span and a 1.5 m chord. An extensive description of the model is found in Singh et al. [7]. The results of the comparison are shown in Fig. 3.17, where the pressure coefficient is sampled at different radial positions θ.The sign convention chosen for the radial position is shown in Fig. 3.16(b).

The overall trends are in good agreement. There are two main differences between the model used in the present work and the one by Singh et al. [7] that ultimately cause the differences observed in the results. The differences are due to (i) the wing models used in the studies, and (ii) the different models for the wing-body interaction. In particular,

- in the work by Singh et al. [7], the wing collocation points are defined on the wetted surface, with the panels modelling the 3D airfoil. Whereas in the present work, the airfoil is reduced to its camber line thus not modeling the airfoil thickness. In the

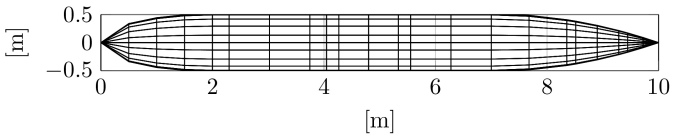

(a) Side view of fuselage aerodynamic mesh.

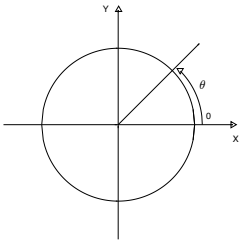

(b) Definition of the positive radial position θ.

Figure 3.16: Fuselage model used for verification.

former case, the forces are thus perpendicular to the local airfoil wetted surface, as opposed to being perpendicular to the camber line (locally) as in the latter case. This explains the slight shift observed in the peak force;

- the wing-body interaction model used in the present work is not needed if the full 3D wing is modelled. In the numerical model in Singh et al., the wing panels will end at the junction meeting the fuselage panels. A discussion with regard to the differences with the experimental data presented in Singh et al. [7] has not been found.

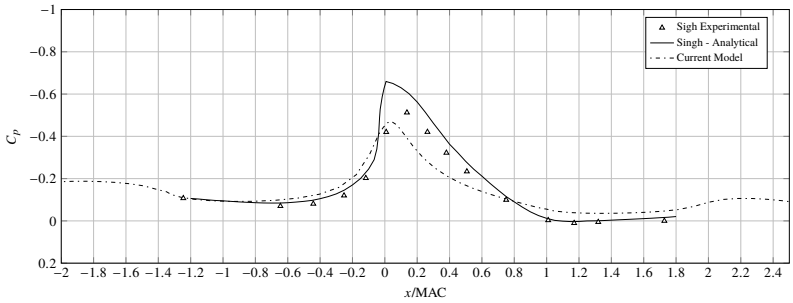

(a) Fuselage line at $\theta = +20$ deg.

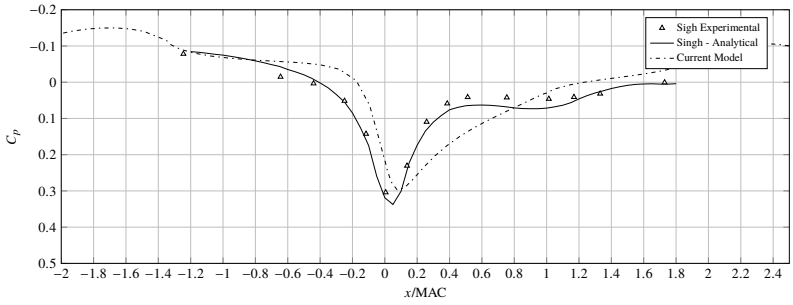

(b) Fuselage line at $\theta = -20$ deg.

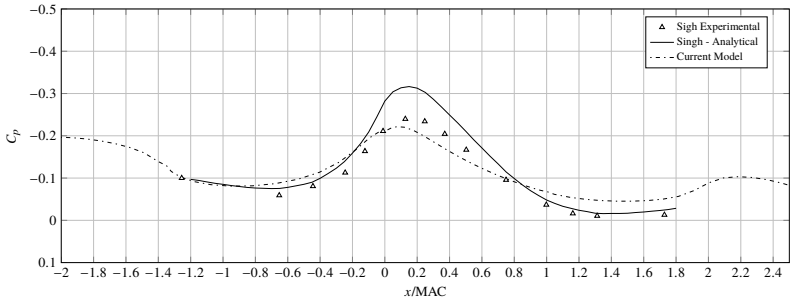

(c) Fuselage line at $\theta = +45$ deg.

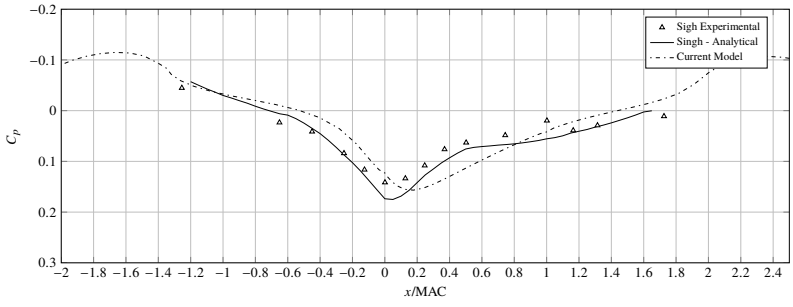

(d) Fuselage line at $\theta = -45$ deg.

Figure 3.17: Fuselage C_p, in comparison with the work of Singh et al. [7].

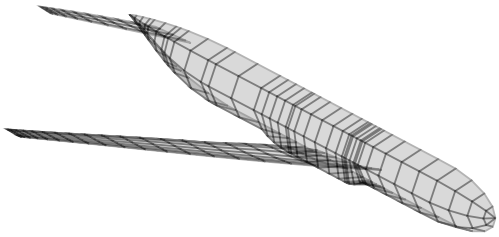

Figure 3.18: Aerodynamic mesh of the symmetric aircraft.

3.2.4. FULL-AIRCRAFT AERODYNAMICS

The aerodynamic models of wing, horizontal tail and fuselage are hereby summarized,

$$\begin{cases} \underline{\underline{A}}_W \underline{\Gamma}_W & = \underline{B}_W \\ \underline{\underline{A}}_{HT} \underline{\Gamma}_{HT} & = \underline{B}_{HT} \\ \underline{\underline{A}}_F \underline{\sigma} & = \underline{B}_F \end{cases} \tag{3.66}$$

with $\underline{\underline{A}}$ being the aerodynamic influence coefficients of fuselage (F), wing (W) and horizontal tail (HT), $\underline{\sigma}$ the fuselage source strength, $\mathbf{\Gamma}$ the vortex strength..

In order to couple the three equations and obtain the full-aircraft aerodynamic model, the following aerodynamic influence coefficients are needed, namely: wing on fuselage, and horizontal tail, horizontal tail on fuselage, and wing , and fuselage on wing, and horizontal tail. The system of equations can then be written as,

$$\begin{bmatrix} \underline{\underline{A}}_W & \underline{\underline{A}}_{W,HT} & \underline{\underline{A}}_{W,F} \\ \underline{\underline{A}}_{HT,W} & \underline{\underline{A}}_{HT} & \underline{\underline{A}}_{HT,F} \\ \underline{\underline{A}}_{F,W} & \underline{\underline{A}}_{F,HT} & \underline{\underline{A}}_F \end{bmatrix} \begin{Bmatrix} \underline{\Gamma}_W \\ \underline{\Gamma}_{HT} \\ \underline{\sigma} \end{Bmatrix} = \begin{Bmatrix} \underline{B}_W \\ \underline{B}_{HT} \\ \underline{B}_F \end{Bmatrix} \tag{3.67}$$

The matrix of influence coeffiencts can be used to extend the unsteady aerodynamic model with the fuselage aerodynamics. Once the source and vortex strength distribution is known across all the panels, the forces are calculated. The force distribution along the fuselage is given by eq.3.65. For wing and horizontal tail, the force is given by the Kutta-Jukowski theorem. With i and j being the spaniwise and chord-wise indexes, the lift expression for a single panel (identified with the indexes i, j) is given by,

$$L_{i,j} = \begin{cases} \rho V_\infty \Gamma_{i,j} \Delta y_{i,j}, & \text{if } j = 1 \\ \rho V_\infty \left(\Gamma_{i,j} - \Gamma_{i,j-1} \right) \Delta y_{i,j}, & \text{if } j \neq 1 \end{cases} \tag{3.68}$$

where $\Delta y_{i,j}$ is the width of the i, j panel. The pressure difference is then given by,

$$\Delta p_{i,j} = \frac{L_{i,j}}{S_{i,j}} \tag{3.69}$$

with $S_{i,j}$ being the area of the panel.

3.3. AEROELASTICITY OF FREE-FREE STRUCTURES

With both the structural and aerodynamic model in state-space format, the aeroelastic model can be derived. The two important factors to the derivation of the aeroelastic system are the two coupling functions to exchange data between the structural and aerodynamic system. In particular:

Aerodynamics → Structures : forces and moments,

Structures → Aerodynamics : angle of attack.

The first transfer function is nothing other than an interpolation scheme between the aerodynamic and structural mesh. The interpolation scheme defines a matrix which we will indicate with the symbol $\underline{\underline{H}}_{AS}$, with AS meaning 'from aerodynamics to structure'. The method of the nearest neighbour has been adopted in this dissertation.

$$\underline{F}_s = \underline{\underline{H}}_{AS}\underline{F}_a \tag{3.70}$$

The function that links the structural model to the aerodynamics is slightly more complex because it requires to write the influence of elastic and rigid degrees of freedom on the angle of attack. The following section presents this derivation.

3.3.1. ANGLE OF ATTACK

The angle of attack is, in the most general case, a function of both elastic and rigid degrees of freedom. As the structure deforms, the mesh is altered and so is the angle of attack seen by the aerodynamic profiles. In the longitudinal case, the relationship between the angle of attack and the elastic and rigid degrees of freedom is given by the following expression:

$$\alpha = \alpha_{\text{air}} + \theta - \frac{\dot{h}}{V_\infty} + \frac{x - x_{EA}}{V_\infty}\dot{\theta}_s + \frac{\dot{h}_r}{V_\infty} + \frac{x - x_{\text{CG}}}{V_\infty}q \tag{3.71}$$

where:

- α_{air} is the perturbation angle of attack induced by the free stream flow,
- θ is the angle of attack induced by the structural and rigid rotations,
- $\dot{h}/V_\infty$ and $\dot{h}_r/V_\infty$ are the perturbation angles of attack induced by elastic and rigid plunge respectively,
- $\dot{\theta}_s \Delta x_{\text{EA}}/V_\infty$ and $q\Delta x_{\text{CG}}/V_\infty$ are the perturbation angles of attack induced by elastic and rigid pitch rates.

A detailed discussion follows on how to derive the contributions to the angle of attack due to each of four factors, namely plunge, twist, plunge rate and twist rate. Note that the rigid equivalents of these factors can be treated in a mathematical sense in the same way as their elastic counterparts since the rigid state is nothing other than an elastic state which is constant across all structural nodes.

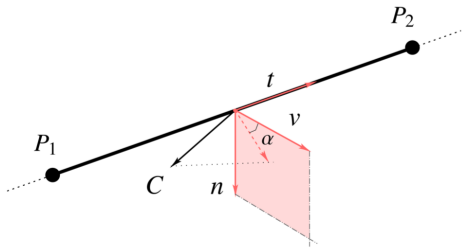

Figure 3.19: Perturbation angle of attack induced by the rotation of the element, both rigid and elastic.

In order to obtain the dynamic perturbation, the angle of attack is linearized around the stationary solution that will be indicated by α_0:

$$\alpha \approx \alpha_0 + \frac{\partial \alpha}{\partial \theta} \Delta\theta \tag{3.72}$$

Let us now look closely at how the rotation of an element influences the angle of attack how the contribution is calculated. For this purpose, let $\underline{t}$ be the tangent vector connecting node i and $i+1$ of the i^{th} structural element and $\underline{c}_0$ the initial chord vector connecting trailing- and leading-edge of the cross-section. If this element is subject to a rotational deformation (indicated by $\underline{\underline{R}}$), the chord vector becomes:

$$\underline{c}_0' = \underline{\underline{R}}\,\underline{\underline{R}}_{\text{ini}}\,\underline{\underline{R}}_{\alpha}\,c_0 \tag{3.73}$$

with $\underline{\underline{R}}_{\text{ini}}$ being the rotation matrix due to the initial wing incidence distribution and $\underline{\underline{R}}_{\alpha}$ the rotation matrix from the body frame of reference to the local aerodynamic reference. This vector will be now projected onto a reference frame described by the right-handed triad created by the tangent vector $\underline{t}$ and the flow velocity unit vector indicated by $\underline{e}_{\infty}$: $\underline{t}$ and $\underline{e}_{\infty}$ and $\underline{t} \times \underline{e}_{\infty}$. This local element frame is indicated in Fig. 3.19 as (v, n). To go from the local element frame to (v, n), the following rotation matrix is to be applied:

$$\underline{\underline{R}}_{\text{loc}} = \begin{bmatrix} \underline{e}_{\infty}^T \\ (\underline{t} \times \underline{e}_{\infty})^T \\ \underline{t}^T \end{bmatrix} \tag{3.74}$$

The deformed chord vector becomes:

$$\underline{c}_0'' = \underline{\underline{R}}_{\text{loc}}\,\underline{c}_0' \tag{3.75}$$

The angle of attack, as seen in Fig. 3.19, can be defined as looking at the projection of $\underline{c}_0''$ on the (v, n) plane, thus:

$$\alpha = \tan^{-1}\left(\frac{c_{0_n}''}{c_{0_v}''}\right) \tag{3.76}$$

or in its linearized version as a function of θ:

$$\alpha = \alpha_0 + \left[1 + \left(\frac{c''_{0_n}}{c''_{0_v}}\right)^2\right]^{-1} \frac{dc''_{0_n} c''_{0_v} - c''_{0_n} dc''_{0_v}}{\left(c''_{0_v}\right)^2} \tag{3.77}$$

with $\mathrm{d}c''$ being:

$$\mathrm{d}c'' = \underline{\underline{R}}_{\text{loc}} \left(\frac{\partial}{\partial \underline{\theta}} \underline{\underline{R}}\right) \underline{\underline{R}}_{\text{ini}} \underline{\underline{R}}_{\alpha} \underline{c}_0 \tag{3.78}$$

The relevant quantities for the angle of attack can be now projected on the v, n frame to calculate the relative components, namely:

$$\begin{cases} \dot{h} = -\left(\underline{\underline{R}}_{\alpha}^T \underline{\dot{u}}_s\right) \cdot \left(\underline{t} \times \underline{e}_{\infty}\right) \\ \dot{h}_r = \left(\underline{\underline{R}}_{\alpha}^T \underline{\dot{u}}_r\right) \cdot \left(\underline{t} \times \underline{e}_{\infty}\right) \\ \dot{\theta}_s = \left(\underline{\underline{R}}_{\alpha}^T \underline{\dot{\theta}}_s\right) \cdot \underline{t} \\ q = \left(\underline{\underline{R}}_{\alpha}^T \underline{\dot{\theta}}_r\right) \cdot \underline{t} \end{cases} \tag{3.79}$$

These equation will be written in matrix format to simply the state-space derivation in the following section.

$$\begin{cases} \underline{\dot{\theta}}_a = \underline{\underline{T}}_t \underline{\dot{\theta}}_s \\ q_a = \underline{\underline{T}}_t^r \underline{\dot{\theta}}_r \\ \underline{\dot{h}} = \underline{\underline{T}}_n \underline{\dot{u}}_s \\ \underline{\dot{h}}_r = \underline{\underline{T}}_n^r \underline{\dot{u}}_r \end{cases} \tag{3.80}$$

3.3.2. STATE-SPACE FORMULATION

From the input equation of the aerodynamic state-space, see [1] for derivation, one has:

$$\begin{Bmatrix} \underline{\dot{\Gamma}}_W \\ \underline{\dot{\alpha}}_{\text{air}} \end{Bmatrix} = \begin{bmatrix} \underline{\underline{K}}_1 & \underline{\underline{K}}_2 \\ \underline{\underline{0}} & \underline{\underline{0}} \end{bmatrix} \begin{Bmatrix} \underline{\Gamma} \\ \underline{\alpha} \end{Bmatrix} + \begin{bmatrix} \underline{\underline{0}} \\ \underline{\underline{I}} \end{bmatrix} \underline{\dot{\alpha}}_{\text{air}} \tag{3.81}$$

Introducing the relationship for alpha as a function of the structural and rigid states in its matrix form:

$$\begin{Bmatrix} \underline{\dot{\Gamma}}_W \\ \underline{\dot{\alpha}}_{\text{air}} \end{Bmatrix} = \begin{bmatrix} \underline{\underline{K}}_1 & \underline{\underline{K}}_2 & -\frac{1}{V_\infty} \underline{\underline{K}}_2 \underline{\underline{B}}_{\alpha} & \underline{\underline{K}}_2 \underline{\underline{B}}_{\alpha} & \underline{\underline{K}}_2 \underline{\underline{B}}_{\text{pitch}} & -\frac{1}{V_\infty} \underline{\underline{K}}_2 \underline{\underline{B}}_{\alpha} & \underline{\underline{K}}_2 \underline{\underline{B}}_{\alpha} & \underline{\underline{K}}_2 \underline{\underline{B}}_{\text{rigid}} \\ \underline{\underline{0}} & \underline{\underline{0}} & \underline{\underline{0}} & \underline{\underline{0}} & \underline{\underline{0}} & \underline{\underline{0}} & \underline{\underline{0}} & \underline{\underline{0}} \end{bmatrix} \begin{Bmatrix} \underline{\Gamma} \\ \underline{\alpha}_{\text{air}} \\ \underline{\dot{h}}_s \\ \underline{\theta}_a \\ \underline{\dot{\theta}}_a \\ \underline{\dot{h}}_r \\ \underline{\theta}_{r,a} \\ \underline{\dot{\theta}}_{r,a} \end{Bmatrix} + \begin{bmatrix} \underline{\underline{0}} \\ \underline{\underline{I}} \end{bmatrix} \underline{\dot{\alpha}}_{\text{air}} \tag{3.82}$$

with the transformation matrices from aerodynamics to structure:

$$\begin{Bmatrix} \dot{\underline{\Gamma}}_W \\ \dot{\underline{\alpha}}_{\text{air}} \end{Bmatrix} = \underbrace{\begin{bmatrix} \underline{\underline{K}}_1 & \underline{\underline{K}}_2 & -\frac{1}{V_\infty}\underline{\underline{K}}_2\underline{\underline{B}}_\alpha\underline{\underline{T}}_n & \underline{\underline{K}}_2\underline{\underline{B}}_\alpha\underline{\underline{T}}_n & \underline{\underline{K}}_2\underline{\underline{B}}_{\text{pitch}}\underline{\underline{T}}_\alpha & -\frac{1}{V_\infty}\underline{\underline{K}}_2\underline{\underline{B}}_\alpha\underline{\underline{T}}_n & \underline{\underline{K}}_2\underline{\underline{B}}_\alpha\underline{\underline{T}}_n & \underline{\underline{K}}_2\underline{\underline{B}}_{\text{rigid}}\underline{\underline{T}}_\alpha \\ \underline{\underline{0}} & \underline{\underline{0}} & \underline{\underline{0}} & \underline{\underline{0}} & \underline{\underline{0}} & \underline{\underline{0}} & \underline{\underline{0}} & \underline{\underline{0}} \end{bmatrix}}_{\underline{\underline{H}}_1} \begin{Bmatrix} \underline{\Gamma} \\ \underline{\alpha}_{\text{air}} \\ \underline{\dot{u}}_s \\ \underline{\theta}_s \\ \underline{\dot{\theta}}_s \\ \underline{\dot{u}}_r \\ \underline{\theta}_r \\ \underline{\dot{\theta}}_r \end{Bmatrix} + \underbrace{\begin{bmatrix} \underline{\underline{0}} \\ \underline{\underline{I}} \end{bmatrix}}_{\underline{\underline{H}}_2} \dot{\underline{\alpha}}_{\text{air}} \tag{3.83}$$

The boolean selection matrix $\underline{\underline{T}}_1$ is defined such that:

$$\begin{Bmatrix} \underline{\Gamma} \\ \underline{\alpha}_{\text{air}} \\ \underline{\dot{u}}_s \\ \underline{\theta}_s \\ \underline{\dot{\theta}}_s \\ \underline{\dot{u}}_r \\ \underline{\theta}_r \\ \underline{\dot{\theta}}_r \end{Bmatrix} = \underline{\underline{T}}_1 \underline{x} \tag{3.84}$$

with $\underline{x}$ being the full state vector, including aerodynamic, structural and rigid degrees of freedom. The aerodynamic input equation can be thus written as:

$$\begin{Bmatrix} \dot{\underline{\Gamma}}_W \\ \dot{\underline{\alpha}}_{\text{air}} \end{Bmatrix} = \underline{\underline{H}}_1 \underline{\underline{T}}_! \underline{x} + \underline{\underline{H}}_2 \dot{\underline{\alpha}}_{\text{air}} \tag{3.85}$$

In a similar fashion, the aerodynamic output equation becomes,

$$\begin{Bmatrix} \underline{F}_a \\ \underline{M}_a \end{Bmatrix} = \underbrace{\begin{bmatrix} \underline{\underline{L}}_1 & \underline{\underline{L}}_2 & -\frac{1}{V_\infty}\underline{\underline{L}}_2\underline{\underline{B}}_\alpha\underline{\underline{T}}_n & \underline{\underline{L}}_2\underline{\underline{B}}_\alpha\underline{\underline{T}}_n & \underline{\underline{L}}_2\underline{\underline{B}}_{\text{pitch}}\underline{\underline{T}}_\alpha & -\frac{1}{V_\infty}\underline{\underline{L}}_2\underline{\underline{B}}_\alpha\underline{\underline{T}}_n & \underline{\underline{L}}_2\underline{\underline{B}}_\alpha\underline{\underline{T}}_n & \underline{\underline{L}}_2\underline{\underline{B}}_{\text{rigid}}\underline{\underline{T}}_\alpha \end{bmatrix}}_{\underline{\underline{H}}_3} \begin{Bmatrix} \underline{\Gamma} \\ \underline{\alpha}_{\text{air}} \\ \underline{\dot{u}}_s \\ \underline{\theta}_s \\ \underline{\dot{\theta}}_s \\ \underline{\dot{u}}_r \\ \underline{\theta}_r \\ \underline{\dot{\theta}}_r \end{Bmatrix}$$

$$+ \underbrace{\begin{bmatrix} -\frac{1}{V_\infty}\underline{\underline{L}}_3\underline{\underline{B}}_\alpha\underline{\underline{T}}_n & \underline{\underline{L}}_3\underline{\underline{B}}_{\text{pitch}}\underline{\underline{T}}_t & -\frac{1}{V_\infty}\underline{\underline{L}}_3\underline{\underline{B}}_\alpha\underline{\underline{T}}_n & \underline{\underline{L}}_3\underline{\underline{B}}_{\text{pitch}}\underline{\underline{T}}_t \end{bmatrix}}_{\underline{\underline{H}}_4} \begin{Bmatrix} \ddot{\underline{u}}_s \\ \ddot{\underline{\theta}}_s \\ \ddot{\underline{u}}_r \\ \ddot{\underline{\theta}}_r \end{Bmatrix}$$

$$+ \underline{\underline{L}}_3\underline{\underline{B}}_\alpha\dot{\underline{\alpha}}_{\text{air}} \tag{3.86}$$

With the introduction of the selection matrix $\underline{\underline{T}}_2$ such that:

$$\begin{Bmatrix} \underline{\ddot{u}}_s \\ \underline{\ddot{\theta}}_s \\ \underline{\ddot{u}}_r \\ \underline{\ddot{\theta}}_r \end{Bmatrix} = \underline{\underline{T}}_2 \underline{\dot{x}}_s \tag{3.87}$$

the output equation becomes:

$$\begin{Bmatrix} \underline{F}_a \\ \underline{M}_a \end{Bmatrix} = \underline{\underline{H}}_3 \underline{\underline{T}}_1 \underline{x} + \underline{\underline{H}}_4 \underline{\underline{T}}_2 \underline{\dot{x}} + \underline{\underline{L}}_3 \underline{\underline{B}}_\alpha \underline{\dot{\alpha}}_{\text{air}} \tag{3.88}$$

The last step to complete the aeroelastic state space system is to write the structural state-space of the free-free wing as a function of the aerodynamic states. Remembering that the structural state-space of the free-free structural can be written in its most general form as:

$$\underline{\ddot{x}}_s = \underline{\underline{A}}_s \underline{x}_s + \underline{\underline{B}}_s \underline{\underline{H}}_{AS} \underline{\underline{R}}_\alpha \begin{Bmatrix} \underline{F}_a \\ \underline{M}_a \end{Bmatrix} \tag{3.89}$$

thus, substituting Eq. 3.88:

$$\underbrace{\left(\underline{\underline{I}} - \underline{\underline{B}}_s \underline{\underline{H}}_{AS} \underline{\underline{R}}_\alpha \underline{\underline{H}}_4 \underline{\underline{T}}_2\right)}_{\underline{\underline{H}}_5} \underline{\dot{x}}_s = \underbrace{\left(\underline{\underline{A}}_s \underline{\underline{T}}_3 + \underline{\underline{B}}_s \underline{\underline{H}}_{AS} \underline{\underline{R}}_\alpha \underline{\underline{H}}_3 \underline{\underline{T}}_1\right)}_{\underline{\underline{H}}_6} \underline{x} + \underbrace{\underline{\underline{B}}_s \underline{\underline{H}}_{AS} \underline{\underline{R}}_\alpha \underline{\underline{L}}_3 \underline{\underline{B}}_\alpha}_{\underline{\underline{H}}_7} \underline{\dot{\alpha}}_{\text{air}} \tag{3.90}$$

with $\underline{\underline{T}}_3$ connecting $\{\underline{u}_s, \underline{\theta}_s, \underline{u}_r, \underline{\theta}_r\}^T$ to $\underline{x}$. Finally, isolating $\underline{\dot{x}}$:

$$\underline{\dot{x}}_s = \underline{\underline{H}}_5^{-1} \underline{\underline{H}}_6 \underline{x} + \underline{\underline{H}}_5^{-1} \underline{\underline{H}}_7 \underline{\dot{\alpha}}_{\text{air}} \tag{3.91}$$

that combined with Eq. 3.85:

$$\underline{\dot{x}} = \underbrace{\begin{bmatrix} \underline{\underline{H}}_1 \underline{\underline{T}}_1 \\ \underline{\underline{H}}_5^{-1} \underline{\underline{H}}_6 \end{bmatrix}}_{\underline{\underline{A}}} \underline{x} + \underbrace{\begin{bmatrix} \underline{\underline{H}}_2 \\ \underline{\underline{H}}_5^{-1} \underline{\underline{H}}_7 \end{bmatrix}}_{\underline{\underline{B}}} \underline{\dot{\alpha}}_{\text{air}} \tag{3.92}$$

The output equation is in principle arbitrary and case-dependent. For example, if one is interested in monitoring the loads and displacements, combining Eq. 3.88 and 3.91:

$$\underbrace{\begin{Bmatrix} \underline{F} \\ \underline{x} \end{Bmatrix}}_{\underline{y}} = \underbrace{\begin{bmatrix} \underline{\underline{R}}_\alpha \underline{\underline{H}}_8 \\ \underline{\underline{T}}_4 \end{bmatrix}}_{\underline{\underline{C}}} \underline{x} + \underbrace{\begin{bmatrix} \underline{\underline{R}}_\alpha \underline{\underline{H}}_9 \\ \underline{\underline{0}} \end{bmatrix}}_{\underline{\underline{D}}} \underline{\dot{\alpha}}_{\text{air}} \tag{3.93}$$

3.3.3. VERIFICATION

In this section, the aeroelastic module will be benchmarked against NASTRAN® predictions on the CRM model (see Appendix C for a detailed description of the model). In particular the following will be investigated: *(i)* the aeroelastic modal response of the wing model and *(ii)* the free-free gust response of the model at a cruise speed of 190 m/s. Obtaining the modal response of an aeroelastic model in state-space means solving the eigenvalue problem at a given speed around which the system is linearized. In NASTRAN®, the aeroelastic modal response is only calculated internally within the flutter solution SOL145. To avoid this problem and extract the aeroelastic modes, the SOL145 is required at one speed point and a discrete range of reduced frequencies. The eigenvectors are only accessible in the *.f06 result file.

The frequencies and modal shape comparison (via the modal assurance criterion) are hereby shown. The error on the frequency is on average 0.26%, with a maximum absolute value at 0.44% on the mode No. 2. The modal shape are in great agreement, with a relatively low level of cross-correlation.

Tab. V.7: Frequency (left) and MAC (right) comparison of the aeroelastic modes of the free-free beam.

	No.	Beam	NASTRAN®	Error (%)
Free-Free	1	2.81	2.82	-0.36
	2	4.37	4.38	-0.44
	3	4.72	4.72	0.03
	4	5.53	5.52	0.13
	5	7.04	7.07	-0.37

No.		NASTRAN®				
1	Beam	0.97	0.29	0.26	0.23	0.11
2		0.45	0.84	0.22	0.16	0.03
3		0.16	0.15	0.81	0.22	0.02
4		0.06	0.02	0.02	0.81	0.26
5		0.26	0.48	0.09	0.05	0.96

The clamped-free comparison is also shown to benchmark the free-free results obtained with the framework developed within this work. The frequencies in this case match within an average error of 0.72% and a maximum absolute value of 1.73% on mode No. 3.

Tab. V.8: Frequency (left) and MAC (right) comparison of the aeroelastic modes of the clamp-free beam.

	No.	Beam	NASTRAN®	Error (%)
Clamp-Free	1	2.43	2.45	-0.82
	2	3.28	3.26	0.61
	3	4.55	4.63	-1.73
	4	5.53	5.5	0.55
	5	6.74	6.73	0.15

No.		NASTRAN®				
1	Beam	0.88	0.17	0.19	0.18	0.00
2		0.14	0.99	0.23	0.17	0.00
3		0.19	0.23	0.98	0.16	0.00
4		0.15	0.12	0.16	0.87	0.02
5		0.04	0.00	0.00	0.00	0.83

A visual comparison of the aeroelastic mode shapes can be found in Fig. 3.21. Since the NASTRAN® eigenvector are only accessible through the *.f06 solution file, the values have been applied on the discrete structural model generated within the current aeroelastic framework to be able to visualize the modes on the 3D wing.

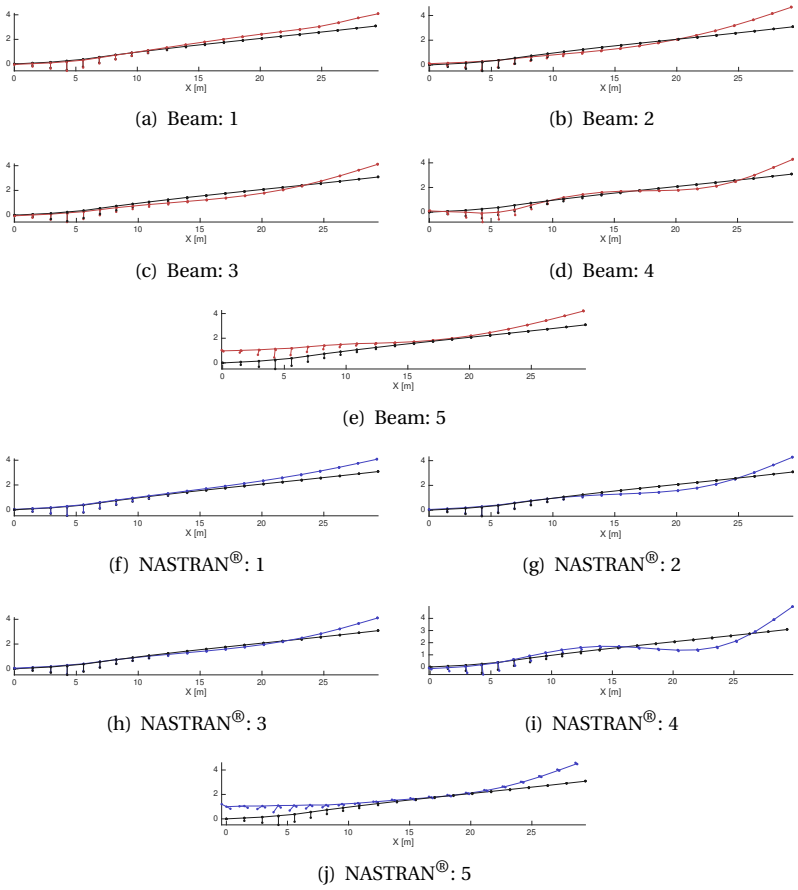

(a) Beam: 1

(b) Beam: 2

(c) Beam: 3

(d) Beam: 4

(e) Beam: 5

(f) NASTRAN®: 1

(g) NASTRAN®: 2

(h) NASTRAN®: 3

(i) NASTRAN®: 4

(j) NASTRAN®: 5

Figure 3.20: Mode shapes of the free-free wing model in comparison.

Below a comparison of the aeroelastic modes of the free flying aircraft is shown. The frequencies match within an average error of 0.58% and a maximum absolute value of 2.76% on mode No. 3.

Tab. V.7: Frequency (left) and MAC (right) comparison of the aeroelastic modes of the free-free aircraft.

	No.	Beam	NASTRAN®	Error (%)
Free-Free	1	1.43	1.44	-0.65
	2	2.27	2.26	0.23
	3	2.45	2.38	2.76
	4	4.11	4.10	0.17
	5	4.76	4.78	-0.40

No.		NASTRAN®				
1	Beam	0.95	0.26	0.25	0.23	0.09
2		0.47	0.86	0.12	0.15	0.02
3		0.17	0.15	0.82	0.24	0.01
4		0.05	0.01	0.02	0.81	0.26
5		0.23	0.48	0.09	0.05	0.96

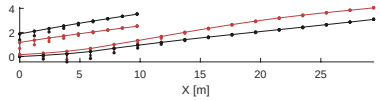

(a) Beam: 1

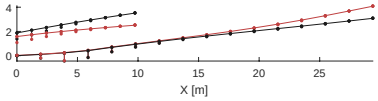

(b) Beam: 2

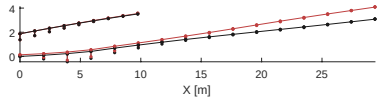

(c) Beam: 3

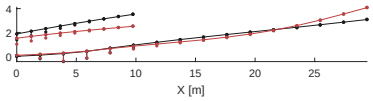

(d) Beam: 4

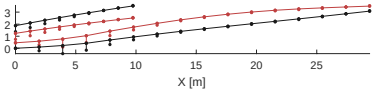

(e) Beam: 5

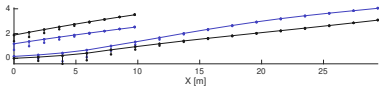

(f) NASTRAN®: 1

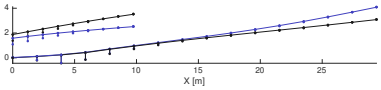

(g) NASTRAN®: 2

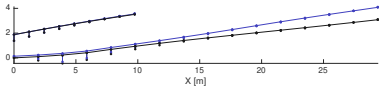

(h) NASTRAN®: 3

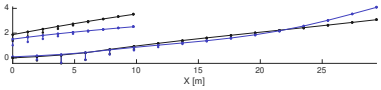

(i) NASTRAN®: 4

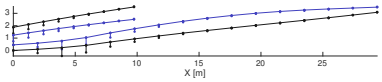

(j) NASTRAN®: 5

Figure 3.21: Mode shapes of the free-free aircraft model in comparison.

Free-Free Gust Response in NASTRAN®

A simplified version of the free-free gust response is obtained using SUPORT1 cards on the root node. This allows to free the elevation and pitch degree of freedom only and calculate the longitudinal response to a gust perturbation. The gust is modeled using a linear combination TLOAD2 cards to obtain the desired input signal.

Assuming a flow velocity of V_∞, and perturbations $V_i << V_\infty$, the angle of attack input signal induced by a '1 - cosine' gust is given by:

$$\alpha_i = \frac{V_i}{V_\infty} = \frac{w_i}{2V_\infty}\left(1 - \cos\frac{\pi V_\infty t}{l}\right), \quad 0 \leq t \leq \frac{2l}{V_\infty} \tag{3.94}$$

with w_i is the maximum value of the gust velocity profile, l is half of the gust length. Remembering that the aeroelastic state-space system is such that the input signal is the time-derivative of the angle of attack, one has:

$$\dot{\alpha}_i = \frac{\pi w_i}{2l}\sin\frac{\pi V_\infty (t - x_i/V_\infty)}{l}, \quad 0 \leq t - \frac{x_i}{V_\infty} \leq \frac{2l}{V_\infty} \tag{3.95}$$

For this analysis, the maximum gust velocity has been set to 17 m/s with a flow velocity of 190 m/s. The gust to flow velocity ratio is thus ≈ 0.089. The input signals are shown in Fig. 3.22.

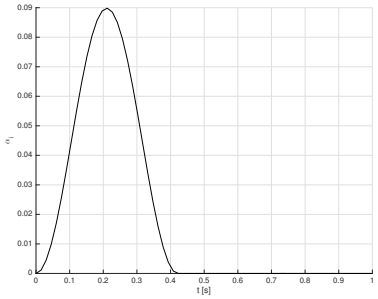

(a) Perturbation angle of attack.

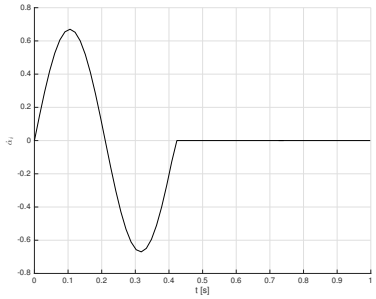

(b) Perturbation angular velocity.

Figure 3.22: Input signals.

The gust response in terms of tip out-of-plane deflection, tip twist deflection, and rigid elevation and pitch are shown in Fig. 3.23. The results show excellent agreement. Note that the elevation will evolve into a very slow oscillation (similar to a phugoid), however the period is far larger than the time-frame of this analysis, [8].

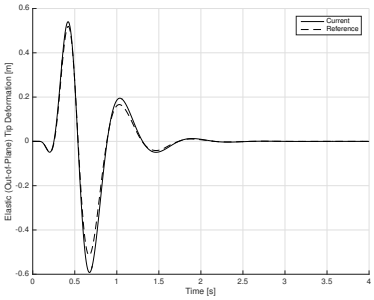

(a) Tip out-of-plane deflection.

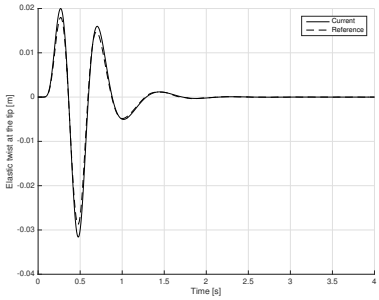

(b) Tip twist.

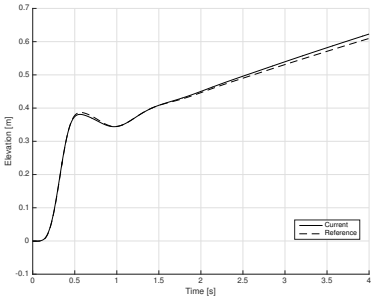

(c) Elevation.

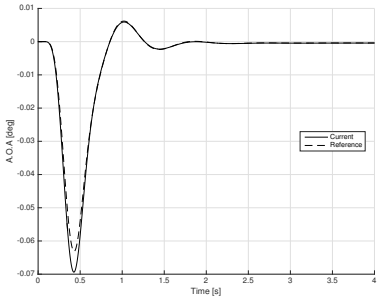

(d) Angle of attack.

Figure 3.23: Gust response using a 1 - cosine profile.
Reference: NASTRAN®, SOL146.

3.4. OVERVIEW OF OPTIMIZATION FRAMEWORK

In this section, the overall optimization work flow will be presented in order to understand the type of information that is exchanged between the analysis and optimization module to be able to calculate new design options, refer to Fig. 3.24. The optimization framework for aeroelastic tailoring starts by defining a set of independent and collectively comprehensive set of variables that describe the design. This set of variable is referred to as design variables. The design variables are optimized in order to minimize the objective function, (e.g. the structural mass of the design). In particular:

- The analysis module takes in the design variables and evaluates the objective function, the constraint margins and the variation of both objective and constraints with respect to the design variables. The constraint margins are quantities, ranging from 0 to 1, that indicate how close the design is to the prescribed margins of safety of a particular phenomenon (e.g. material failure).
- The optimization module takes in the objective function, the constraints and the sensitivities thereof with respect to the design variables, and determines the new set of design variables that minimize the objective function.

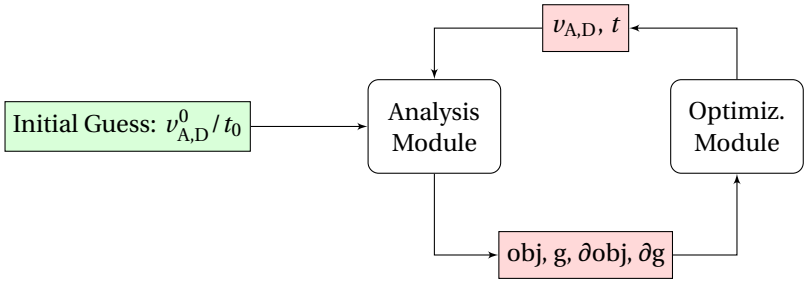

Figure 3.24: Optimization work flow and information exchange.

In a classic aeroelastic tailoring optimization, [1], the design variables are the lamination parameters and the thickness of a composite laminate. The lamination parameters are a continuous representation of the stiffness properties of the laminate. The relationship between the lamination parameters and the laminate stiffness distribution is discussed in Sec. 3.4.1. In Sec. 3.4.2, the stiffness properties of the laminates are derived as a function of the highest stiffness direction of the laminate, also referred to as principal direction. The implications and application of this particular stiffness representation will be further elaborated in Chap. 5.

3.4.1. STIFFNESS PARAMETERIZATION

The lamination parameters were first introduced by Tsai et al. [9] as a representation of the stiffness properties of a composite laminate in integral form. In particular, the lamination parameters are divided in three categories for *(i)* in-plane stiffness, indicated with subscript A, *(ii)* the coupling stiffness, indicated with subscript B, *(iii)* the out-of-plane stiffness, indicated with subscript D. With θ being the ply angles of a given stacking sequence, the lamination parameters for a general laminate are the following 12 variables:

$$\{v_{1A}, v_{2A}, v_{3A}, v_{4A}\} = \int_{-0.5}^{0.5} \{\cos 2\theta, \sin 2\theta, \cos 4\theta, \sin 4\theta\}\, d\bar{z}$$

$$\{v_{1B}, v_{2B}, v_{3B}, v_{4B}\} = 4\int_{-0.5}^{0.5} \bar{z}\,\{\cos 2\theta, \sin 2\theta, \cos 4\theta, \sin 4\theta\}\, d\bar{z} \tag{3.96}$$

$$\{v_{1D}, v_{2D}, v_{3D}, v_{4D}\} = 12\int_{-0.5}^{0.5} \bar{z}^2\,\{\cos 2\theta, \sin 2\theta, \cos 4\theta, \sin 4\theta\}\, d\bar{z}$$

where v refers to the lamination parameters, θ to the orientation of the ply, and $\bar{z}$ to the ply thickness.

The relationship between the lamination parameters and the stiffness matrices ($\underline{\underline{A}}$, $\underline{\underline{B}}$ and $\underline{\underline{D}}$) are then given by:

$$\begin{aligned}
\underline{\underline{A}} &= h\left(\underline{\underline{\Gamma}}_0 + \underline{\underline{\Gamma}}_1 v_{1A} + \underline{\underline{\Gamma}}_2 v_{2A} + \underline{\underline{\Gamma}}_3 v_{3A} + \underline{\underline{\Gamma}}_4 v_{4A}\right) \\
\underline{\underline{B}} &= \frac{h^2}{4}\left(\underline{\underline{\Gamma}}_0 + \underline{\underline{\Gamma}}_1 v_{1B} + \underline{\underline{\Gamma}}_2 v_{2B} + \underline{\underline{\Gamma}}_3 v_{3B} + \underline{\underline{\Gamma}}_4 v_{4B}\right) \\
\underline{\underline{D}} &= \frac{h^3}{12}\left(\underline{\underline{\Gamma}}_0 + \underline{\underline{\Gamma}}_1 v_{1D} + \underline{\underline{\Gamma}}_2 v_{2D} + \underline{\underline{\Gamma}}_3 v_{3D} + \underline{\underline{\Gamma}}_4 v_{4D}\right)
\end{aligned} \tag{3.97}$$

with $\underline{\underline{\Gamma}}_i$ being the matrices of material invariants, related to the material properties $E_{1,1}$, $E_{2,2}$, $G_{1,2}$, ν_{12}, as derived in extensive details in Gürdal et al. [10].

Once the lamination parameters, and their relationships with the in-plane, coupling and out-of-plane stiffness matrices are known, the stiffness distribution can be visualized as a function of the angular direction θ. This visualization is shown only for the in-plane ($\underline{\underline{A}}$) and out-of-plane ($\underline{\underline{D}}$) stiffness matrices, since for symmetric laminate the coupling matrix $\underline{\underline{B}}$ is zero. For each set of lamination parameters (or equivalently for each laminate) the modulus of elasticity related to both membrane (m) and flexural (f) stiffness along an axis θ can be defined as follows:

$$E_m = \frac{1}{h A_{1,1}^{-1}(\theta)} \tag{3.98}$$

$$E_f = \frac{12}{h^3 D_{1,1}^{-1}(\theta)} \tag{3.99}$$

The stiffness terms as a function of the angular direction θ is obtained by the following matrix rotation:

$$\begin{cases}
A_{1,1}^{-1}(\theta) = \underline{\underline{T}}^T A_{1,1}^{-1} \underline{\underline{T}} \\
D_{1,1}^{-1}(\theta) = \underline{\underline{T}}^T D_{1,1}^{-1} \underline{\underline{T}}
\end{cases} \tag{3.100}$$

with $\underline{\underline{T}}$ being the rotation matrix defined as:

$$\underline{\underline{T}} = \begin{bmatrix}
\cos^2\theta & \sin^2\theta & 2\cos\theta\sin\theta \\
\sin^2\theta & \cos^2\theta & -2\cos\theta\sin\theta \\
-\cos\theta\sin\theta & \cos\theta\sin\theta & \cos^2\theta - \sin^2\theta
\end{bmatrix} \tag{3.101}$$

An example of the in-plane stiffness distribution derived using this visualization method for different standard laminates is hereby shown. The laminates are indicated with the main fiber angle and its percentage as a subscript, e.g. 0_{25} means 25% fibers at 0°.

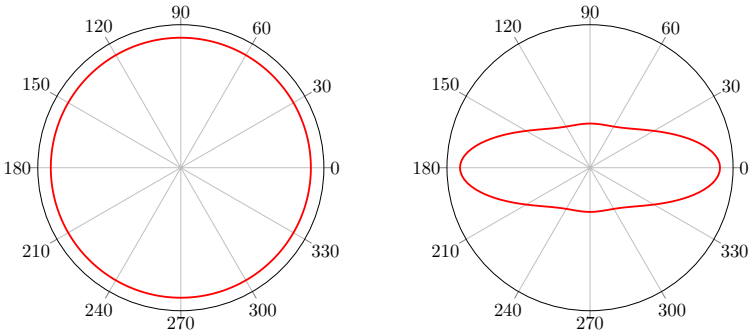

(a) $0_{25}/90_{25}/\pm 45_{50}$ (b) $0_{60}/90_{10}/\pm 45_{30}$

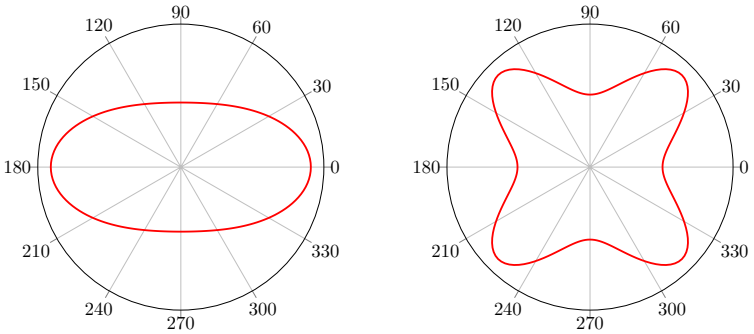

(c) $0_{44}/90_{12}/\pm 45_{44}$ (d) $0_{10}/90_{10}/\pm 45_{80}$

Figure 3.25: Stiffness distribution of standard composite laminates.

3.4.2. PRINCIPAL DIRECTION OPTIMIZATION

The term principal direction refers to the direction on the panel where the highest stiffness is registered. In most cases, the principal direction is unique and can be easily identified from the polar plots. However, in the most generic case, where there might be multiple directions at high stiffness (e.g. Fig. 3.25(d)), the 0 direction can be taken as a reference. The idea behind Principal Direction Optimization is to adjust the orientation of the stiffness polar (or equivalently of its principal direction) to minimize structural mass under a given set of performance requirements. In this section, this approach will be presented in detail, with the aim of combining two main aspects, namely *(i)* the weight-saving potential of stiffness tailoring and *(ii)* the advantages of working with standard certified laminates. To be able to optimize the principal direction , the relationship between the lamination parameters and the laminate principal direction has to be calculated. The derivation is hereby presented.

LAMINATION PARAMETERS AS A FUNCTION OF THE PRINCIPAL DIRECTION

Let v^*_{iA} and v^*_{iD} be the in-plane and out-of-plane lamination parameters of a given standard stacking sequence, chosen at the start of the optimization. For the purposes of this derivation, let us assume that the principal direction of this laminate is aligned with the 0 axis of the polar plot. It has already been seen how the stiffness modulus (either membrane or flexural) is a function of the axis orientation θ^* via the lamination parameters. In this section, the relationship between the lamination parameters and the principal direction orientation α will be derived.

At the start of the optimization, the lamination parameters are given by:

$$\begin{aligned}\{v^*_{1A}, v^*_{2A}, v^*_{3A}, v^*_{4A}\} &= \int_{-0.5}^{0.5} \{\cos 2\theta^*, \sin 2\theta^*, \cos 4\theta^*, \sin 4\theta^*\}\, d\bar{z} \\ \{v^*_{1D}, v^*_{2D}, v^*_{3D}, v^*_{4D}\} &= 12\int_{-0.5}^{0.5} \bar{z}^2 \{\cos 2\theta^*, \sin 2\theta^*, \cos 4\theta^*, \sin 4\theta^*\}\, d\bar{z}\end{aligned} \tag{3.102}$$

With θ being the combined axis orientation (that includes the shift of the principal direction α, equal for all plies in a laminate) defined as:

$$\theta = \theta^* + \alpha \tag{3.103}$$

the lamination parameters of the rotated stack become:

$$\begin{aligned}\{v_{1A}, v_{2A}, v_{3A}, v_{4A}\} &= \int_{-0.5}^{0.5} \{\cos 2(\theta^* + \alpha), \sin 2(\theta^* + \alpha), \cos 4(\theta^* + \alpha), \sin 4(\theta^* + \alpha)\}\, d\bar{z} \\ \{v_{1D}, v_{2D}, v_{3D}, v_{4D}\} &= 12\int_{-0.5}^{0.5} \bar{z}^2 \{\cos 2(\theta^* + \alpha), \sin 2(\theta^* + \alpha), \cos 4(\theta^* + \alpha), \sin 4(\theta^* + \alpha)\}\, d\bar{z}\end{aligned} \tag{3.104}$$

One of the lamination parameters will be worked out in detail to show the complete approach. The other terms can be derived similarly. The expression of v_{1A} is:

$$v_{1A} = \int_{-0.5}^{0.5} \cos 2(\theta^* + \alpha)\, d\bar{z} \tag{3.105}$$

or equivalently,

$$v_{1A} = \int_{-0.5}^{0.5} \cos 2\theta^* \cos 2\alpha - \sin 2\theta^* \sin 2\alpha\, d\bar{z} \tag{3.106}$$

by separating the integrals, one obtains,

$$v_{1A} = \int_{-0.5}^{0.5} \cos 2\theta^* \cos 2\alpha\, d\bar{z} - \int_{-0.5}^{0.5} \sin 2\theta^* \sin 2\alpha\, d\bar{z} \tag{3.107}$$

which leads to (see Eq. 3.102),

$$v_{1A} = v^*_{1A} \cos 2\alpha - v^*_{2A} \sin 2\alpha \tag{3.108}$$

By following a similar logic, and leveraging the standard formulas for cosine and sine for summation of angles the following relationships for the lamination parameters can be calculated, both in-plane:

$$\begin{cases} v_{1A} = v^*_{1A}\cos 2\alpha - v^*_{2A}\sin 2\alpha \\ v_{2A} = v^*_{1A}\sin 2\alpha + v^*_{2A}\cos 2\alpha \\ v_{3A} = v^*_{3A}\cos 4\alpha - v^*_{4A}\sin 4\alpha \\ v_{4A} = v^*_{3A}\sin 4\alpha + v^*_{4A}\cos 4\alpha \end{cases} \tag{3.109}$$

as well as out-of-plane:

$$\begin{cases} v_{1D} = v^*_{1D}\cos 2\alpha - v^*_{2D}\sin 2\alpha \\ v_{2D} = v^*_{1D}\sin 2\alpha + v^*_{2D}\cos 2\alpha \\ v_{3D} = v^*_{3D}\cos 4\alpha - v^*_{4D}\sin 4\alpha \\ v_{4D} = v^*_{3D}\sin 4\alpha + v^*_{4D}\cos 4\alpha \end{cases} \tag{3.110}$$

Equivalently, in matrix format, the two sets of equations become:

$$\begin{Bmatrix} v_{1A} \\ v_{2A} \\ v_{3A} \\ v_{4A} \\ v_{1D} \\ v_{2D} \\ v_{3D} \\ v_{4D} \end{Bmatrix} = \underbrace{\begin{bmatrix} \cos 2\alpha & -\sin 2\alpha & & & & & & \\ \sin 2\alpha & \cos 2\alpha & & & & & & \\ & & \cos 4\alpha & -\sin 2\alpha & & & & \\ & & \sin 4\alpha & \cos 4\alpha & & & & \\ & & & & \cos 2\alpha & -\sin 2\alpha & & \\ & & & & \sin 2\alpha & \cos 2\alpha & & \\ & & & & & & \cos 4\alpha & -\sin 4\alpha \\ & & & & & & \sin 4\alpha & \cos 4\alpha \end{bmatrix}}_{\underline{\underline{T}}(\alpha)} \begin{Bmatrix} v^*_{1A} \\ v^*_{2A} \\ v^*_{3A} \\ v^*_{4A} \\ v^*_{1D} \\ v^*_{2D} \\ v^*_{3D} \\ v^*_{4D} \end{Bmatrix} \tag{3.111}$$

In this format, the sensitivities with respect to the principal direction α, indicated as $v_{i,\alpha}$, can be calculated as follows:

$$\begin{Bmatrix} v_{1A,\alpha} \\ v_{2A,\alpha} \\ v_{3A,\alpha} \\ v_{4A,\alpha} \\ v_{1D,\alpha} \\ v_{2D,\alpha} \\ v_{3D,\alpha} \\ v_{4D,\alpha} \end{Bmatrix} = \underbrace{\begin{bmatrix} 2\sin 2\alpha & 2\cos 2\alpha & & & & & & \\ -2\cos 2\alpha & 2\sin 2\alpha & & & & & & \\ & & 4\sin 4\alpha & 4\cos 2\alpha & & & & \\ & & -4\cos 4\alpha & 4\sin 4\alpha & & & & \\ & & & & 2\sin 2\alpha & 2\cos 2\alpha & & \\ & & & & -2\cos 2\alpha & 2\sin 2\alpha & & \\ & & & & & & 4\sin 4\alpha & 4\cos 4\alpha \\ & & & & & & -4\cos 4\alpha & 4\sin 4\alpha \end{bmatrix}}_{\partial\underline{\underline{T}}/\partial\alpha(\alpha)} \begin{Bmatrix} v^*_{1A} \\ v^*_{2A} \\ v^*_{3A} \\ v^*_{4A} \\ v^*_{1D} \\ v^*_{2D} \\ v^*_{3D} \\ v^*_{4D} \end{Bmatrix} \tag{3.112}$$

To verify the validity of this approach, the author compared the lamination parameters calculated with the classic laminate theory to the ones calculated with Eq.3.111 following a rotation α of the principal direction. The laminate chosen for this verification is the standard $0_{60}/90_{10}/\pm 45_{30}$ with a principal direction rotation $\alpha = -30°$. Note that a positive angular rotation is counterclockwise on the polar plot.

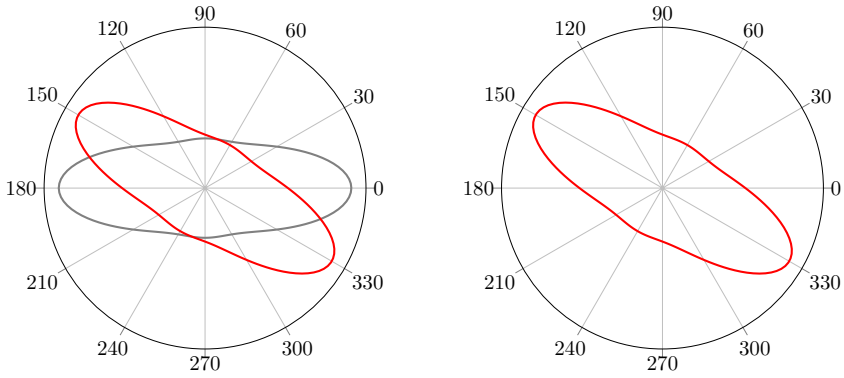

(a) Stiffness distribution (red) of the standard stacking sequence after the application of the principal rotation α.

(b) Stiffness distribution of the rotated stacking sequence using classic lamination theory.

The lamination parameters in the comparison show an exact match compared to the prediction classic lamination theory applied on the rotated stack, [10].

Lamination Parameters	Principal Rotation	Classic Lamination Theory	Err. [%]
v_{1A}	0.46985	0.46985	3.5E-14
v_{2A}	0.17101	0.17101	1.0E-14
v_{3A}	0.30642	0.30642	-1.8E-14
v_{4A}	0.25712	0.25712	-4.3E-14
v_{1D}	0.84248	0.84248	1.3E-14
v_{2D}	0.31382	0.31382	1.8E-14
v_{3D}	0.72468	0.72468	-1.5E-14
v_{4D}	0.60808	0.60808	-1.8E-14

Finally, for optimization purposes, the derivatives of the lamination parameters with respect to the principal direction rotation α can be used to extend the sensitivities in the current work flow (that exchanges sensitivities with respect to lamination parameters) using the chain rule. For example, the constraint sensitivity with respect to v_{1A} can be transformed to a derivative to α as follows:

$$\frac{\partial g}{\partial \alpha} = \frac{\partial g}{\partial v_{1A}} \frac{\partial v_{1A}}{\partial \alpha} \equiv \frac{\partial g}{\partial v_{1A}} \frac{\partial \underline{\underline{T}}}{\partial \alpha}(\alpha)\, v^*_{1A} \tag{3.113}$$

The other sensitivities can be derived similarly.

REFERENCES

[1] N. Werter, *Aeroelastic modelling and design of aeroelastically tailored and morphing wings,* PhD Dissertation, Delft University of Technology (2017).

[2] P. Nikravesh, *Understanding mean-axis conditions as floating reference frames,* Advances in Computational Multibody Systems, 2:185–203 (2005).

[3] Siemens, *Plm standard practices,* https://www.plm.automation.siemens.com/global/en/ (2019).

[4] J. Hess and A. Smith, *Calculation of potential flow about arbitrary bodies,* Progress in Aeronautical Sciences, 8:1–138 (1967).

[5] J. Katz and A. Plotkin, *Low-speed aerodynamics,* Mac Graw-Hill (1991).

[6] Z. Rusak, E. Wasserstrom, and A. Seginer, *Numerical calculation of nonlinear aerodynamics of wing-body configurations,* AIAA Journal, 21(7):929–936 (1983).

[7] S. Singh, N.and Aikat and B. Basu, *Incompressible potential flow about complete aircraft configurations,* Aeronautical Journal, 93(929):335–343 (1989).

[8] T. Xiao, L. Zhang, and M. Fei, *Asiasim 2012, part ii, ccis 324, pp. 319–327, springer-verlag berlin heidelberg,* 2012 (nan).

[9] S. Tsai and N. Pagano, *Invariant properties of composite materials,* Composite Materials Workshop, pp.233-253, Technomic Publishing Co., Westport, CT, USA (1968).

[10] Z. Gürdal, R. Haftka, and P. Hajela, *Design and optimization of laminated composite materials,* John Wiley and Sons, Inc (1999).

4

AEROELASTIC TAILORING

In this section, the classic approach to aeroelastic tailoring, namely the optimization of the clamped-free wing, will be compared to *(i)* the optimization of the free-free wing and *(ii)* the optimization of the flexible aircraft. The comparison will be discussed in terms of optimum design and its performance (e.g. structural mass, active constraints, load alleviation etc.). In this comparison, the overall mass and load (re)distribution during the aeroelastic tailoring optimization will be discussed and monitored. Both distributions contribute to the final objective (structural mass) and the performance of the design. Furthermore, the weight-saving potential, the sizing constraints and relevant aeroelastic phenomena driving the optimization will be discussed for each of the above-mentioned approaches.

4.1. OBJECTIVE AND CONSTRAINTS

The objective of the optimizations is to minimize the structural mass of the composite wing by optimizing its thickness and stiffness distribution, described as a function of lamination parameters. As discussed in Chap. 2, the formulation in terms of lamination parameters is continuous and is thus suitable for gradient-based optimizers. The present work uses the globally convergent method of moving asymptotes (GCMMA) as presented by Svanberg [1]. The globally convergent version of the method of moving asymptotes (MMA) is a variant that divides the optimization search in an outer and inner loop to guarantee convergence to some local minimum from any feasible starting point. In particular, the outer iteration is the one that searches for the next design option while the inner iteration refines the design option looking for a feasible solution. The constraints adopted for the aeroelastic tailoring optimization and their relative margins of safety (MS) or limits are summarized in Tab. 4.1. The margins of safety combine both certification aspects, according to EASA CS-25, and knockdown factors for material scatter and barely-visible impact damage, [2]. The additional constraint required for free-free structures is with respect to their handling qualities. The formulation for this constraint in the longitudinal case is further discussed in Sec. 4.2.

Table 4.1: Details of constraint limits and margins of safety.

Minimum Thickness	0.00183 [m] (10 plies)
Maximum Tensile Strain	6420 [μs]
Maximum Compression Strain	4857 [μs]
Maximum Shear Strain	5332 [μs]
MS for Aeroelastic Stability	0.15
Interval of Local Angle of Attack	$\pm$15 [deg]
MS of Buckling Factor	0.4375
Minimum Aileron Effectiveness	0.10

4.2. HANDLING QUALITIES

The aeroelastic state-space of the free-free wing raises an important question regarding the assessment of the system stability at a certain speed. In classic aeroelastic tailoring[1] the stability of the system is enforced constraining its eigenvalues. This guarantees flutter- and divergence-free designs. A similar approach can be used to ensure aeroelastic stability of the free-free model. However, generally speaking, it is not always possible to stabilize the phugoid and short-period response[2]. The two responses fall under what regulatory bodies call *longitudinal handling qualities* with specific ranges of values specified per aircraft category and mission. These values ensure *(i)* stability of the system or equivalently *(ii)* acceptable levels of performance as long as an active control-system can intervene. The handling qualities are thus an indication of the level of maneuverability of an aircraft. The maneuverability is commonly assessed using a numerical rating scale first introduced by Cooper et al. in 1969 [3].

The most extensive certification requirements are found in the US Military Specification for Flying Qualities, MIL-HDBK-1797, also based on the Cooper and Harper rating scale. The scale distinguishes between three levels of handling qualities, namely:

- *Level 1*: adequate for the mission,
- *Level 2*: acceptable for the mission even though some degradation in effectiveness may exist,
- *Level 3*: controllable.

In case of any degradation of effectiveness within the flight envelope (*Level 2* maneuverability) it is important to demonstrate that the control system can safely intervene to restore the desired level of effectiveness. For certification purposes, the flight qualities are to be proven adequate for the mission, thus *Level 1* maneuverability, regardless of any control action.

[1] Aeroelastic tailoring of the clamped-free wing.
[2] This applies to unconventional configurations, especially military aircraft.

The levels of maneuverability are defined for four different aircraft classes. Among those, the one of interest in commercial aviation is *Class III*. This class generally encompasses large, heavy, medium-to-low maneuverability. Within this class, the handling qualities are furthermore distinguished for three flight phases referred to as *categories* (CAT),

CAT A: combat and high-precision maneuvers,

CAT B: gradual maneuvers (e.g. cruise, pull-up, pull-down),

CAT C: take-off and landing.

The following are the handling qualities selected for the stability and maneuverability assessment needed for aeroelastic tailoring optimization,

- phugoid damping,
- short-period damping,
- short-period frequency,
- flight-path constraint, measuring the variation of the angle of attack due to a change in flight speed in degrees/knots.

The requirements prescribed by the specifications can be enforced as constraints for the optimization thus ensuring that the tailored design meets the required level of maneuverability for a given mission. An overview of all the constraints across the certification levels is hereby shown.

	Level 1	Level 2	Level 3
Phugoid	$\zeta \geq 0.04$	$\zeta \geq 0$	$T \geq 55$s
Flight Path	$\alpha/V \leq 0.06$	$\alpha/V \leq 0.15$	$\alpha/V \leq 0.25$
Short-Period Damping (CAT. A/C)	$0.35 \leq \zeta \leq 1.30$	$0.25 \leq \zeta \leq 2.00$	$0.15 \leq \zeta$[3]
Short-Period Damping (CAT. B)	$0.30 \leq \zeta \leq 2.00$	$0.20 \leq \zeta \leq 2.00$	$0.15 \leq \zeta$

The short-period frequency has a more elaborate constraint formulated as a function of *(i)* the ratio n_z/α (in g's/radiants)[4] and *(ii)* the frequency ω_n in radiants. The constraint ranges across the three levels are shown in Fig. 4.1.

Applying the constraint on the short-period frequency translates into enforcing the frequency to get as close as possible to the middle line in the prescribed range. In this way one can ensure that:

- regardless of the initial design point (possibly assessed at Level 2 or 3), the optimizer has a clear path to Level 1, and
- the value of the short-period frequency does not get closer to the range boundaries as the optimization converges.

A more in-depth analysis of the evolution of the short-period frequency on this diagram will be discussed later in the result section.

[3] It can be adjusted, together with the regulatory bodies, at altitudes above 20,000 ft.
[4] n_z is the load factor in multiples of the gravitational acceleration

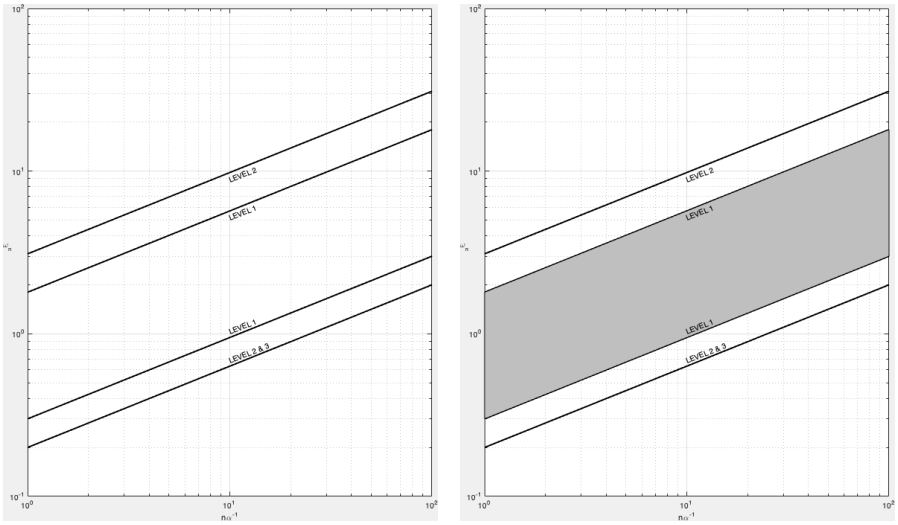

(a) Constraint ranges across all three levels.

(b) Range for a *Level 1* assessment.

Figure 4.1: Constraints on the short-period frequency. The requirement for a *Level 1* assessment is to have a design that falls between the interval indicated in the figure.
Legend: on the x axis: load factor / angle of attack $n\alpha^{-1}$ [rad]; on the y axis: modal frequency ω_n [rad/s].

Table 4.2: Overview of static load cases.

LC	Mach [-]	EAS [m/s]	n_z [-]	Description
1	0.85	240.0	2.5	Pull-up maneuver
2	0.60	198.0	-1	Push-down maneuver

4.3. OPTIMIZATION SET-UP

The aircraft model used for the aeroelastic tailoring studies hereby discussed is based on the NASA Common Research Model (CRM). The geometric description of the aircraft is shown in Fig. 4.2, where the engine and main landing gear location is indicated. The fuel distribution is given in Fig. 4.3(a). The loadcases adopted for the study can be found in Tab. 4.2.

At the start of the optimization the wing has a zero-dominated layup (60% in 0, 10% in 90 and 30% in ±45) for top and bottom skin and quasi-isotropic (QI) spars. Such stiffness distribution is widely used as a reference in aeroelastic tailoring, as discussed in Dillinger et al. [4], for a more realistic estimation of the weight-saving potential of aeroelastic tailoring as opposed to a QI initial design which is highly over-designed. The fuselage, in the flexible aircraft case with an initial mass of 21,800 kg, has a QI stiffness distribution and both stiffness and thickness are kept constant throughout the optimization.

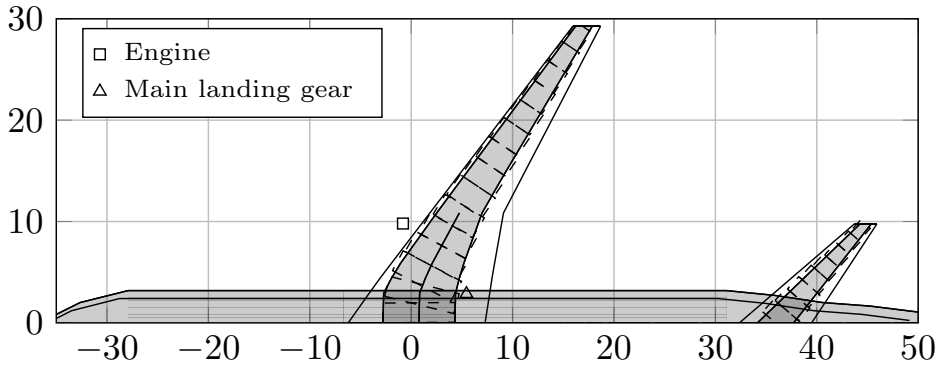

Figure 4.2: CRM aircraft model. Length on both the x and y axis is in SI unit [m].
Note: only the wing and horizontal tail are optimized (optimization ID = 2).

Three aeroelastic tailoring optimizations have been run on the CRM-wing model:
(i) the classic aeroelastic tailoring optimization with a clamp-free wing (ID = 0),
(ii) the aeroelastic tailoring of a free-free wing (ID = 1) and
(iii) the flexible aircraft model (ID = 2).

The design variables for each of the three optimizations are the lamination parameters and the thickness of the skins and spars panels of a composite wing. In the flexible aircraft case, the lamination parameters and thickness of the horizontal tail are also optimized. The goal of the study is to observe the difference in optimum design due to mass and load (re)distribution. The specific loading condition and mass distribution influence the severity of a particular constraint, which translates into an influence in the design area available to the optimizer to look for optimum solutions.

Below follows an overview of the optimization set-up for all three cases addressed in this chapter, together with a quantitative analysis and visual representation of the differences between the three optimizations.

		ID		
		0	1	2
Model Details	Wing is optimized.	✓	✓	✓
	Tail is optimized.	✗	✗	✓
	Fuselage flexibility.	✗	✗	✓
	Fuselage is optimized.	✗	✗	✗
Constraints	Buckling	✓	✓	✓
	Material Failure	✓	✓	✓
	Aeroelastic Stability	✓	✓	✓
	Flight Dynamics Stability	✗	✓	✓

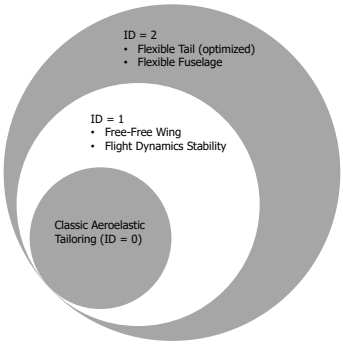

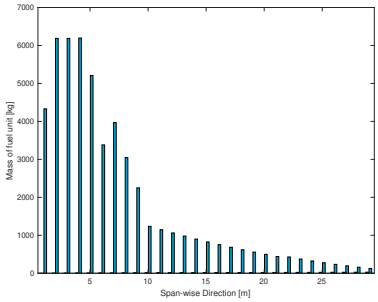

(a) Fuel distribution along the wing.

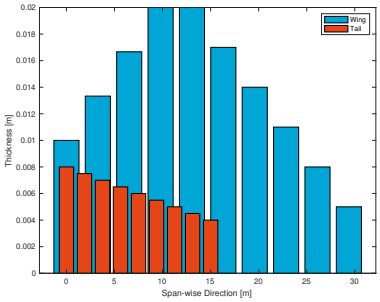

(b) Initial thickness distribution of the wing.

Figure 4.3: Data distributions of the initial design.

Table 4.3: Converged objective in comparison. Wing structural mass is indicated.
The wing structural mass accounts for the mass of skins, spars and stringers only.

ID	Model	mass [kg]	Δ [%]
0	Clamped-Free Wing	4,650	-
1	Free-Free Wing	4,846	+4.4
2	Flexible Aircraft	5,215	+12.0

4.4. OPTIMIZATION RESULTS

The wing-only optimization (ID = 0) converged to a final wing structural mass, that includes the mass of skins, spars, and stringers, of 4,650 kg, which will be used as a reference for this discussion. As shown in Tab. 4.3, the free-free wing (ID = 1) has a structural mass of 4,846 kg (about 4.4% heavier), whereas the aircraft (ID = 2) shows an increase in structural mass of approximately 12% to about 5,125 kg. These results can be explained by looking at the physics behind aeroelastic tailoring, and the results of the strains and buckling margins shown in Appendices E and F. In short, there are several main physical factors that are driving the results of these optimization, namely *(i)* the severity of the handling quality constraints in optimization 1, and *(ii)* the beneficial effect of the horizontal tail flexibility in optimization 2, *(iii)* its detrimental effect in optimization 2, and *(iv)* the tailoring effects resulting from a change in mass and fiber angle distribution.

4.4.1. INFLUENCE OF THE HANDLING QUALITY CONSTRAINTS

In optimization 1, a free-free wing via aeroelastic tailoring is designed requiring a stable Level 1 design in terms of handling qualities. This constraint implies that *1)* the design shows no dynamic instability, and *2)* the modal response falls within a prescribed interval of frequency and damping. Among the four main responses monitored for the assessment of the longitudinal handling qualities, the short-period is the most critical since the process of aeroelastic tailoring tends to destabilize it as a consequence of load redistribution during the optimization.

In particular, the objective of aeroelastic tailoring is weight minimization which implies a wing root bending moment minimization (RBM) by moving lift inboard. For a swept-back wing, an inboard movement of the lift vector also implies a forward movement (towards the aircraft nose). At the same time, the center of gravity (CG) is also moving backward (towards the rear of the aircraft) due to the fact that the wing weight decreases during the optimization. These two factors cause the aerodynamic center (AC) to move in front of the CG, which indicates an unstable short period mode, [5]. An example of a design with an unstable short-period as a result of an aeroelastic tailoring optimization process is found in previous work of the author, [6]. In this case the author, only monitored the short-period response to observe its evolution during a tailoring optimization.

Enforcing handling quality constraint means not only correcting this tendency to instability but also steering the short-period response into a prescribed range. Moreover, steering the short-period response into a certain range (for example Level 1) has to do with increasing the frequency separation between short-period and first out-of-plane bending. Since these two modes fall in a similar range of frequency (1-5 Hz), these modes can resonate thus leading to body-freedom instabilities. A clear frequency separation can already be seen in stiff wing models (for example, conventional aluminum wings), but as the structures increase in flexibility the relative difference becomes less. The value of short period frequencies has been monitored during the optimization for both the clamped-free wing and the free-free wing. The convergence history is shown in Fig. 4.4 for both loads cases. For the optimum design the Level 1 value for the short-period frequency is of 1.87 Hz. The value of the short-period frequency at the end of the optimization is 3.15 Hz, with a separation of 1.84 Hz from the Level 1 frequency, which is at 1.31 Hz. The significance of the handling quality constraint prescribed by the regulations can be now better understood and quantified. Finally, note how the clamped-free wing would violated this condition, reaching a frequency separation of only 0.2 Hz at the end of the optimization.

In synthesis.

- The load redistribution that occurs during the process of an aeroelastic tailoring optimization tends to destabilize the short-period response.
- This tendency can be corrected thus obtaining a stable Level 1 design in terms of handling quality. This correction results in an increase in structural mass of the optimum design.
- The handling quality constraint prescribed by the authorities means requiring a minimum separation frequency between the short-period and the first out-of-plane bending frequency.

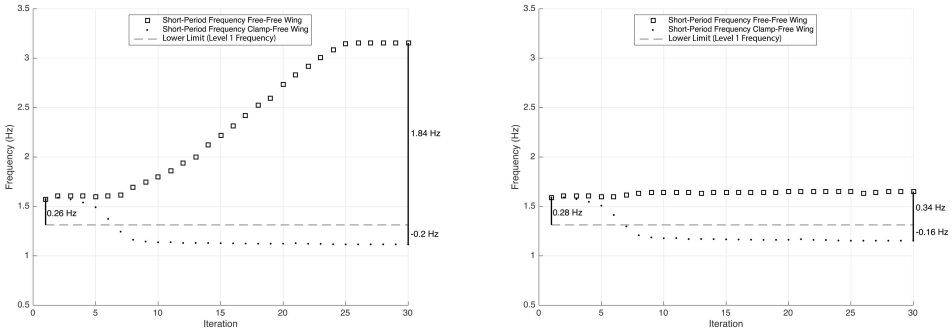

(a) Load case 1 (pull-up maneuver)

(b) Load case 2 (push-down maneuver)

Figure 4.4: History of short-period and first out-of-plane bending (IOB) frequencies.

4.4.2. BENEFICIAL EFFECT OF THE FLEXIBLE TAIL

In subsection 4.4.1, it has been discussed how the aerodynamic center (AC) and center of gravity (CG) move during an aeroelastic tailoring optimization as a result of the load redistribution caused by stiffness and mass tailoring. The relative position of the CG with respect to AC is important for the stability of the aircraft in flight. One of the reasons as to why the handling quality constraints have severe consequences for the optimum design in terms of final structural mass is because it becomes difficult to correct the short-period response when the optimizer has a narrow range of available CG positions. In optimization 1 (free-free wing), the only parameter to vary the CG position is the wing structural mass distribution, but the range is rather narrow compared to optimization 2 (flexible aircraft) where the optimizer can vary the mass of the horizontal tail as well. Changing the mass distribution on the horizontal tail has a bigger effect on the CG position because of the relative distance between the two surfaces (i.e. wing and horizontal tail.). This is what is referred to as the beneficial effect of the tail.

To put things into perspective, in optimization 1 the max. difference in terms of CG between the first and last iteration of the optimization is 1.80 m, compared to a shift of 3.41 m in optimization 2, Fig. 4.5. The wider range of CG position is a favorable tool, in unison with the stiffness and mass tailoring, to correct the short-period response. This statement is also supported by the fact that the flight dynamic stability is not active in optimization 2. The sizing constraint in this case is a combination of material and buckling failure.

4.4.3. NEGATIVE EFFECT OF THE FLEXIBLE TAIL

The terms *negative* refers to the fact that a certain behaviour causes the objective function (to minimize) to increase in value. The negative effect of the horizontal tail is due to the fact that it has the potential to increase the loading conditions on the wing, thus increasing the stress and the severity of buckling on the wing surface. The magnitude of

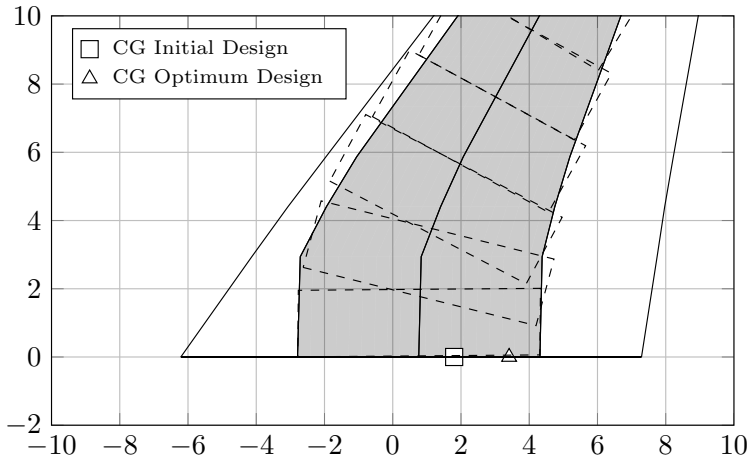

Figure 4.5: Detail of the root section to highlight the shift in CG position during optimization 2. Length on both the x and y axis is in SI unit [m].

the loads experienced by the tail is relatively low compared to the ones on the wing so that the condition on the tail is not critical.

The influence of the tail is particularly on the moment equilibrium and it depends on the relative position between the wing aerodynamic center (AC) and the aircraft center of gravity (CG), as shown in 4.4.2.

In case the CG is in front of the AC, the horizontal tail generates negative lift to balance the moment. As a result, the lift the wing has to generate is equal to the weight plus the lift generated by the tail,

$$L_{\text{wing}} = W + L_{\text{tail}} \tag{4.1}$$

hence

$$L_{\text{wing}} > W \tag{4.2}$$

The opposite scenario, where the AC is in front of the CG, the horizontal tail generates positive lift, thus,

$$L_{\text{wing}} < W \tag{4.3}$$

In synthesis:

- The horizontal tail has the beneficial effect of extending the range of available CG position to correct the flight dynamic stability.
- The horizontal tail has the detrimental effect of increasing the loading conditions (depending on the relative position of AC and CG) on the wing, thus increasing the strain levels.
- The aim of the optimizer is to find the appropriate balance between moving the AC (through load redistribution) and moving the CG (through mass redistribution) to achieve *1)* optimal stability and *2)* manageable stress/strain levels.

4.4.4. OVERVIEW OF THE DRIVERS BEHIND THE OPTIMIZATION

With the term *drivers* the author refers to the set of factors that drive the objective function to its minimum value. The adjective beneficial will be used to indicate that any particular factor/event tends to decrease the objective function (directly beneficial) or create a certain condition that is favorable to a decrease in objective function (indirectly beneficial - e.g. a decrease in the strain level leads to a lighter design because the wing is under less critical loading conditions). Vice versa, negative will refer to those factors/events causing, directly or indirectly, an increase in objective function.

Beneficial Drivers

- Decrease in root-bending moment due to an in-board shift of the lift distribution.
- Decrease in overall lift due to the positive lift generated by the horizontal tail (NB: this also implies that the AC is in front of the CG).
- Wide range of CG positions available and attainable through mass redistribution by the optimizer.

Negative Drivers

- AC moves in front of the CG due to an in-board shift of the lift distribution.
- Increase in overall lift due to the negative lift generated by the horizontal tail (NB: this also implies that the CG is in front of the AC).
- Narrow range of CG positions available and attainable through mass redistribution by the optimizer.

It is important to mention how some of the forces behind the optimization are opposing each other, with the same force having the potential of being both beneficial or detrimental depending on the particular case. For example, a shift in the relative position of AC and CG can either cause a decrease in root-bending moment (beneficial) or a dynamic instability (detrimental) depending on the circumstances and the severity of the other constraints (which also steer the load distribution in a certain direction).

Here is the task of the optimizer, through the sensitivities, to find the path with the least conflict between these forces and achieve an optimal objective. It has also been observed how the optimizer, as a last resort, makes use of a classic approach to solving some of the design and stability requirement, namely increasing the structural mass. By increasing the mass, and the rigidity of the structure, does two things to the design: *1)* it automatically increases the frequency separation between flexible and rigid modes (because of the decrease in flexibility), *2)* it decreases the overall stress levels of the structure. A visual overview of the drivers is shown in Fig. 4.6.

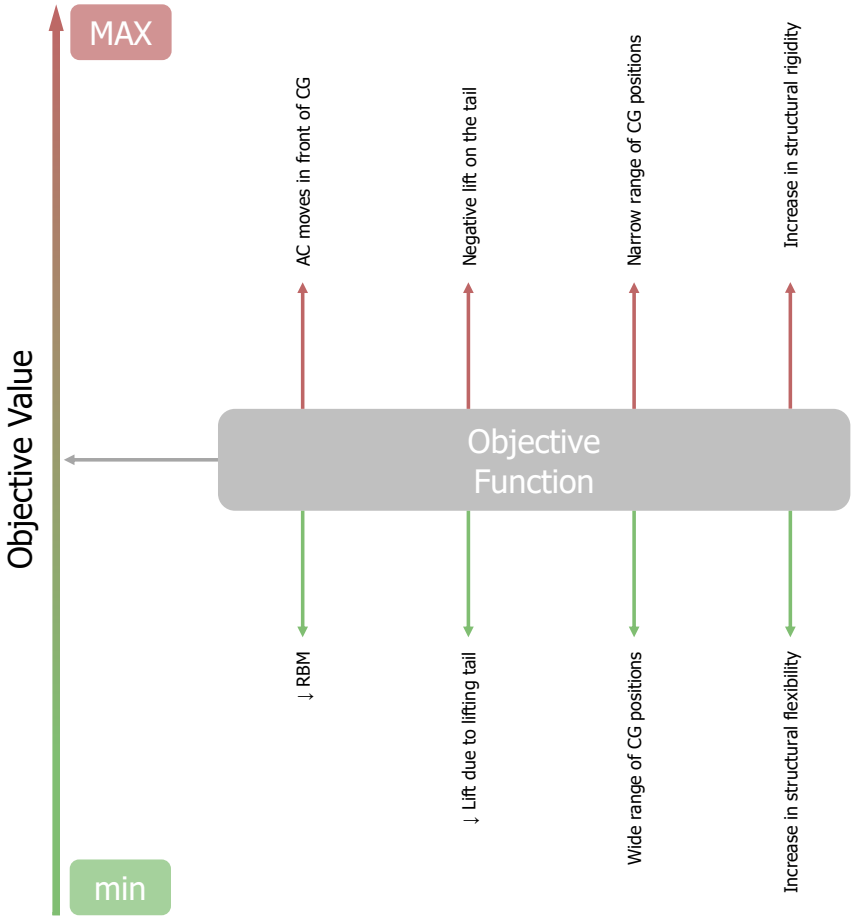

Figure 4.6: Visual overview of the drivers behind the optimization.

4.4.5. STIFFNESS AND MASS TAILORING

The results on stiffness and thickness tailoring are summarized in Appendix E. In all three optimization cases, one can see the following trends,

- a beneficial wash-out effect is induced by controlling the stiffness and thickness distribution. An example of wash-out control through material tailoring is observed in the spar thickness distribution in Appendix E.1 where the front spar is thicker than the rear spar. This allows the rear spar to deform more, compared to the front spar, and thus reduce the local angle of attack. A similar trend can be seen in the top and bottom skin in chord-wise direction. The stiffness tailoring, on the other hand, controls the local twist distribution by rotating the principal direction of the design patches. This phenomenon can be observed in the optimized stiffness distribution of both top and bottom skin in Appendix E.2 and E.3.,

- the optimized stiffness distribution is a result of the particular active constraint associated to every patch. For example, the patches where the buckling margins are closer to the critical value of 1.0, the optimized stiffness approaches almost a cross-ply stiffness distribution that is most suitable for a buckling driven design. On the other hand, a very defined principal direction is typical of patches where the strain margins are critical.

4.4.6. MARGINS

This paragraph discusses the results in terms of margins calculated during the optimization via aeroelastic tailoring. An overview of the strain and buckling margins of the design configurations used for this study are shown in Appendix F. Both measures are conservative to account for material imperfections, damage and scatter.

The strain and buckling margins are active in maneuver load cases. The margins are influenced by the internal load distribution and consequently both the material and stiffness distribution of the optimized design will determine whether strain or buckling failure occurs first. In particular:

- in optimization 1, due to load redistribution for both load alleviation and to stabilize the handling quality response, the inboard area are under high loading conditions causing both strains and buckling indexes to reach the prescribed margin.

- in optimization 2, the wing is sized by a combination of buckling and strain. The strain levels are relatively higher compared to optimization 0 since the horizontal tail has a detrimental effect generating opposite lift to balance out the moment. This happens because the CG is pushed in front of the AC to stabilize the aeroelastic system.

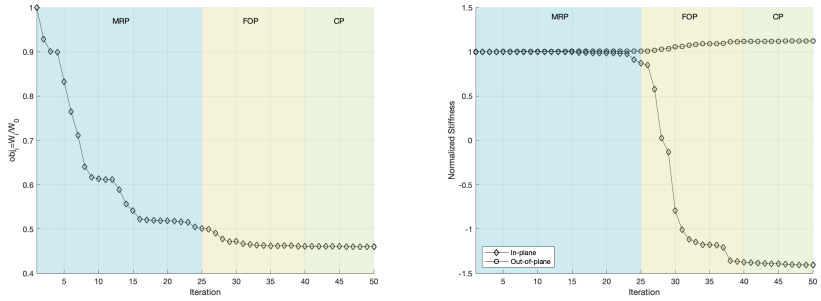

(a) Objective history.

(b) Stiffness history

Figure 4.7: The three phases of aeroelastic tailoring on the objective convergence in optimization 0.
Legend: **MRP** refers to **m**ass **r**emoval **p**hase, **FOP** to **f**iber **o**rientation **p**hase and **CP** to **c**onvergence **p**hase.

4.4.7. THE THREE PHASES OF AEROELASTIC TAILORING

In this section, another interesting process behind aeroelastic tailoring optimizations will be discussed. The three phases of aeroelastic tailoring refer to the generic approach to mass minimization chosen by the optimizer based on the sensitivity analysis. The process of minimizing the structural mass happens in the following three steps:

- Mass Removal Phase (MRP). In this initial phase, in the very first iterations, the objective function (in this case the structural mass) drops significantly. Here the optimizer is removing the additional mass and redistributing the remaining mass. In optimization 0, the objective has dropped by about 50% in this phase, Fig. 4.7(a).
- Fiber Orientation Phase (FOP). With the new mass distribution, the fiber orientation (and specifically the principal orientation) is to be adjusted to decrease the strain levels and achieve further mass reduction, Fig. 4.7(b). The stiffness history in Fig. 4.7(b) shows the average in-plane ($E_{11,\mathrm{m}}$ or membrane) and out-of-plane ($E_{11,\mathrm{f}}$ or flexural) stiffness of the wing structure, normalized as $(1 - E/E_0)$. The change in lamination parameters is reflected in the value of both membrane and flexural stiffness, [2].
- Convergence Phase (CP). In this last phase, usually reaching iteration number 20-50 depending on the specific case, the objective is rather stable at its minimum value while the optimizer explores the last options in terms of mass redistribution and fiber orientation.

It is important to note that these three phases do not show a clear-cut separation, but in reality one can observe an overlap of a few iterations between them. The design performance indicators are changing in either the MRP or FOP region as a result of the changes in mass and fiber angle orientation.

REFERENCES

[1] K. Svanberg, *The method of moving asymptotes – a new method for structural optimization,* International Journal for Numerical Methods in Engineering, 24, 359-373 (1987).

[2] C. Kassapoglou, *Design and analysis of composite structures with applications to aerospace structures,* John Wiley and Sons, Ltd Publication (2010).

[3] G. Cooper and R. Harper, *The use of pilot rating in the evaluation of aircraft handling qualities,* Technical Report TN D-5153, NASA (1969).

[4] J. Dillinger, *Static aeroelastic optimization of composite wings with variable stiffness laminates",* PhD Dissertation, Delft University of Technology (2014).

[5] B. Etkin, *Dynamics of atmospheric flight,* Dover Publications (2005).

[6] M. Natella, X. Wang, and R. De Breuker, *The effect of aeroelastic tailoring on flight dynamic stability,* 59th AIAA/ASCE/AHS/ASC Structures, Structural Dynamics, and Materials Conference (2018).

5

STIFFNESS OPTIMIZATION STRATEGIES

The stiffness of a certain panel is determined by a set of 12 lamination parameters, also referred to as *stiffness design variables*. Only 8 of these parameters describe the stiffness distribution of unbalanced/symmetric laminates. During the optimization, these variables are allowed to change within limits of feasibility [1] to achieve the adequate stiffness distribution to alleviate load and reduce the structural mass. The biggest objection to this practice comes from the aeronautical and aerospace industry with regard to the many problems of working with unbalanced/symmetric laminates. In this chapter the author will *(i)* give an overview of the industry standards at the time of this writing and elaborate on the problem of using unbalanced/symmetric laminates for real-life structures, *(ii)* present an alternative option to stiffness optimization that combines the industry requirements and the weight-saving potential of the latest academic practices. The proposed approach will be referred to as Principal Direction Optimization.

In this chapter the following three approaches will be discussed:

- *Standard Laminates Optimization* (SLAM) : This is the industry standard at the time of this writing. The approach consists of using a set of predefined stacking sequences for which material allowables are determined through testing.
- *Unbalanced/Symmetric Laminates Optimization* (USYM): This is the latest practice in aeroelastic tailoring, allowing full variation of the lamination parameters for unbalanced/symmetric laminates.
- *Principal Direction Optimization* (PDIR) : The proposed alternative to combine the benefits of SLAM and USYM optimization. This method uses standard/certified laminates while optimizing their highest stiffness direction to reduce mass.

The PDIR and USYM optimization strategies will be benchmarked against the industry standard (SLAM) to understand the weight-saving potential and the main design drivers. The flexible aircraft model is used for this study. The reader is referred to Sec. 3.4.1 for further details on the *Principal Direction Optimization* and Sec. 4.3 for the optimization settings.

5.1. DISCUSSION ON INDUSTRY STANDARDS

Composite design and manufacturing in the aerospace industry is heavily regulated. The certification aspects revolve around the ability to understand and predict failure modes and material allowables, [2]. In particular, moving from the coupon to part level, two things have to be proven: 1) that the failure modes at a coupon level are the same as the ones at a part level and 2) that the models developed at the coupon level are able to predict the failure modes at the part level. These two conditions have been proven for metals and a selected number of composite laminates, for example the quasi-isotropic. Proving the link between the coupon and the part level for unbalanced/symmetric composite laminates is a more ambitious endeavor. This is mainly due to the lack of reliable methods for failure prediction and poor understanding of the failure modes of this class of composite materials. Not being able to rely on the scalability and predictability of material allowables and failure modes implies increasing costs (testing, manufacturing, certification etc.) for an aircraft manufacturer, far beyond commercial viability of the product. It is upon the research community not only to invest further into the understanding, modeling and prediction of the failure mechanisms of more complex composite laminates, but also to prove a significant benefit in terms of design performance that would justify further investment in testing, manufacturing and certification.

THE SCALABILITY PROBLEM OF FAILURE MODES AND ALLOWABLES

Research in the field of failure mechanisms of composite laminates is perhaps the most challenging area within this topic. The nature of composite materials, with the coexistence of matrix and fibers, is such that knowledge of material failure developed for aluminum materials is in most cases invalid or at best inaccurate. An important study highlighting the particular effect of scalability (in terms of laminate thickness) on failure modes is found in Cimini et al. [3]. The work analyses the failure mode resulting from a notched specimen (which can also model imperfections). The mode and relative allowable predicted at specimen level changed when assessing a laminate of scaled thickness. Scaling introduces 3D effects, through the thickness, which in turn cause new failure mechanisms more likely to be critical under a certain loading condition. This kind of unpredictability is what invalidates most of the failure criteria developed for aluminum, or isotropic materials.

RANGES OF SCALABILITY FOR BALANCED LAMINATES

The practical solution for industry relies in the identification of a range of thickness where the specimen properties are constant. For quasi-isotropic, and balanced/symmetric laminates one can create families of laminates with similar failure modes and allowables and determine (experimentally) a range of thickness in which the failure characterization remains unaltered. Adding an extra set of fibers, or creating a new laminate family implies the extra cost (in terms of human effort and operational costs) of setting up a new test campaign to characterize a certain laminate and validate the scalability range. For a more extensive overview of this practice, the author directs the interested reader to the work of Feraboli et al. [4] and [5].

Table 5.1: Converged objective in comparison. Wing structural mass is indicated.

Strategy	mass [kg]	Δ_{SLAM} [%]	Δ_{USYM} [%]
SLAM	5776	N/A	+11.
PDIR	5623	-2.6	+7.8
USYM	5215	-9.7	N/A

5.2. OPTIMIZATION RESULTS

In this section the results of the three aeroelastic tailoring optimizations, referred to as SLAM, PDIR and USYM, are presented. The optimization using standard laminates (SLAM) will be used as a benchmark for the other two cases. In all three cases, the following laminates are used for optimization purposes.

Part	0 (%)	±45 (%)	90 (%)
Top Skin	60	30	10
Bottom Skin	60	30	10
Front Spar	60	30	10
Rear Spar	60	30	10
Stringers	60	30	10

As summarized in Tab. 5.1, the structural mass obtained for the reference model (SLAM) is 5,776 kg for the wing. By optimizing the principal direction of the standard laminates (PDIR) one can further reduce the structural mass by about 3%, while the optimization using unbalanced/symmetric laminates gives us a 10% saving in structural mass.

There are three major observations that can be made based on the data from this particular study.

1. In all three cases, the thickness of the laminates is distributed in such a way to alleviate load by reducing the aerodynamic load in the outboard region. This is achieved in two ways, *(i)* by differential thickness in chord-wise direction and *(ii)* by differential thickness in the spar layout, in particular designing the spars in such a way that the rear spar is thinner than the front spar. These are both common trends observed in classic aeroelastic tailoring and thus confirmed in this study.

2. In the PDIR optimization, while the overall stiffness polar stays fixed, the principal direction converges to a similar direction as the one obtained in the USYM optimization. This indicates that load alleviation is mainly controlled by the principal direction of a laminate rather than the specific laminate itself, see Fig. 5.1.

3. The main difference between the PDIR and USYM optimization lies in the margins and constraints violations of the optimum design. This point requires a more elaborate discussion, addressed in Sec. 5.3.

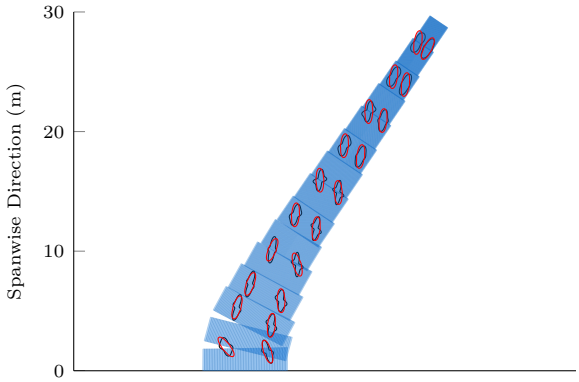

Figure 5.1: Top skin optimized thickness in comparison.
Legend → Black: USYM, Red: PDIR

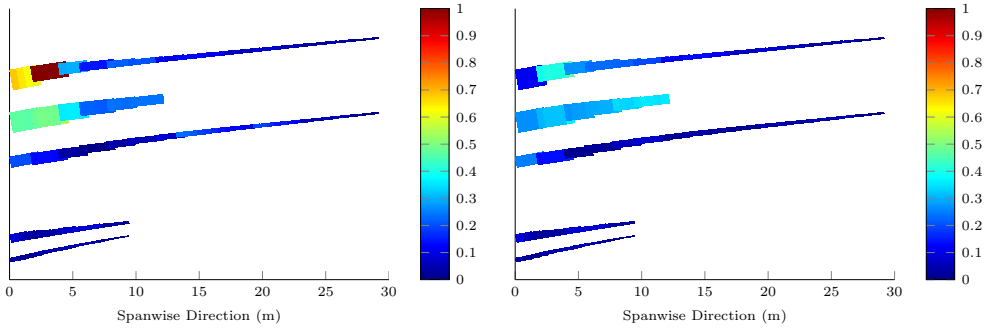

(a) $0_{60}/\pm 45_{30}/90_{10}$ (b) $0_{10}/\pm 45_{80}/90_{10}$

Figure 5.2: Buckling margins for spars mounting different standard laminates.

5.3. LAMINATE SELECTION

It has been mentioned in the previous section how the main difference between the PDIR and USYM optimization lies in the margins (and constraint violations) of the final design. In this section, the reasoning for this difference will be further detailed. The underlying objective is twofold. By analyzing this difference further one aims at *(i)* improving the margins of the PDIR optimum design and *(ii)* explore whether there is room to further decrease the structural mass of the design, currently just 3% lower.

In this particular comparison between the PDIR and USYM optimization, the PDIR optimization leads to a design that shows more critical conditions in buckling. In particular in the spars, the numerical buckling constraint value actually goes beyond the prescribed limit of 1.0 reaching the value of 1.3, see Appendix H.2. The interested reader can find more information on the buckling model used for this analysis in Appendix D.

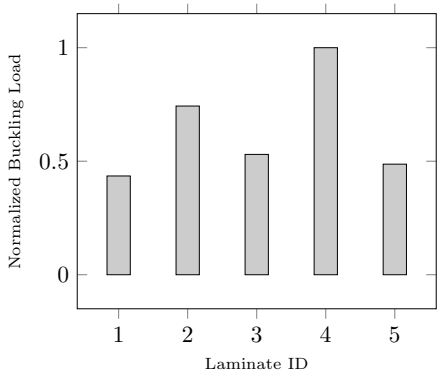

Figure 5.3: Buckling load of the specimen using different standard stacking sequence.

The higher buckling margins can be explained by looking back at the choice of laminates made for the wing and their buckling load. For the spars in the PDIR optimization a 0-dominated standard laminate has been chosen, with 60% fibers in 0° direction, 30% in ±45° and 10% in 90°. The question is whether the relatively poor performance in buckling was driven by the poor performance of this standard laminate, or in other words by the relatively low buckling load of this particular laminate. To test this hypothesis one can look at different standard stacking sequence and calculated the buckling load (under combined loading[1]) of a specimen. The idea behind this strategy is to:

- see if a standard laminate with a significantly higher buckling load can be found, and
- the implication of using a superior laminate (as in with a higher buckling load) in the PDIR optimization can be quantified.

For this comparison, the following stacking sequences were taken into consideration:

Laminate ID	0 (%)	±45 (%)	90 (%)
1	60	30	10
2	25	50	25
3	44	44	12
4	10	80	10
5	50	40	10

Each of these stacking sequences has been applied on a specimen of 0.5 aspect ratio for the estimation of the buckling load under combined compression and shear loading. For the analytical model used for the quick assessment of the buckling load of the specimen, the interested reader is referred to the work of Kassapoglou [6].

[1] Combined loading refers to both compression and shear.

As seen from Fig. 5.3, sequence 4 ($0_{10}/\pm45_{80}/90_{10}$) has a significantly higher buckling load than the remaining 4 sequences. To assess whether a specimen with a higher buckling load can improve the performance of the optimum design, a PDIR optimization is run where sequence 4 is applied to the spars. By doing this, the following has been observed for the final design:

- The structural mass of the wing converged to 5581 kg, further reducing the structural mass compared to the SLAM benchmark (5776 kg). The relative difference is around 4%.
- The spars are not critical any more in buckling. The index does not exceed the predefined margin of 15%. A visual comparison of the buckling margins of the spars in both optimizations is shown in Fig. 5.2.

5.4. A FRAMEWORK FOR PRINCIPAL DIRECTION OPTIMIZATION

Based on the data and insights from this case study, one can derive a framework for aeroelastic tailoring of standard (and certified) laminates via principal direction optimization.

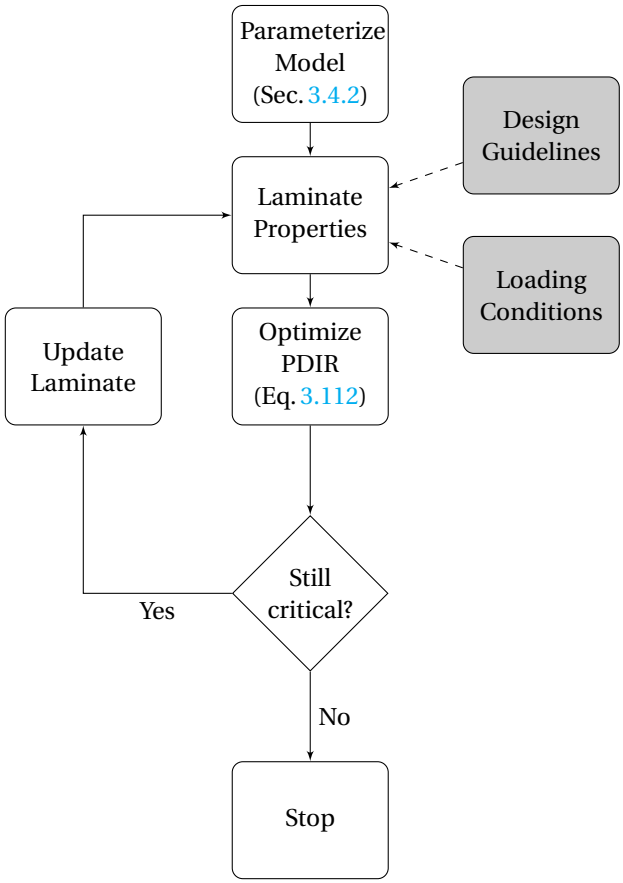

There are three main steps to perform principal direction optimization while minimizing the structural mass and achieve good design performance in terms of margins.

- Step 1: Parameterize the design as discussed in Sec. 3.4.2 to describe the stiffness distribution as a sole function of the principal direction of the laminate. Note that for the purposes of the optimization, the choice of principal direction is arbitrary. For simplicity it can always be aligned with the 0 of the stiffness polar.
- Step 2: Identify critical areas based on the loading conditions of a particular design to derive the core performance required in that area. For example, in a static pull-up maneuver, the inboard area of the top skin is likely to be under heavy loading conditions which indicates a higher probability of observing material failure.
- Step 3: For the critical areas, choose a standard laminate that matched the required performance. Note that the critical areas are defined as laminates for which a given margin is ≥ 1.

Note that for the purposes of this exercise, the author has not taken into account a pre-optimization step where the initial stacking sequence is optimized for specific performance required for the design. For the future development of this framework, it is worth looking into ways to connect the principal direction optimizer to a database of certified stacking sequences for which the material allowables are known. The principal direction optimizer could be wrapped into a discrete-type optimizer (for example using genetic algorithms) to select a particular stacking sequence for the predefined critical areas.

REFERENCES

[1] Z. Gürdal, R. Haftka, and P. Hajela, *Design and optimization of laminated composite materials,* John Wiley and Sons, Inc (1999).

[2] SAE, *Composite material handbook,* Volume 17 (2017).

[3] T. Pinto, C. Cimini, and S. Ha, *Ply thickness influence in compression after impact damage on carbon/epoxy test specimens,* 31st Congress of the International Council of the Aeronautical Sciences, ICAS 2018 International Council of the Aeronautical Sciences (2018).

[4] P. Feraboli, F. Deleo, B. Wade, M. Rassaian, M. Higgins, A. Byar, M. Reggiani, A. Bonfatti, L. DeOto, and M. A, *Predictive modeling of an energy-absorbing sandwich structural concept using the building block approach,* Composites (Part A), 41/6, pp. 774-786 (2010).

[5] P. Feraboli, *Composite materials strength determination within the current certification methodology for aircraft structures,* Journal of Aircraft, 46/4, pp. 1365-1374 (2009).

[6] C. Kassapoglou, *Design and analysis of composite structures with applications to aerospace structures,* John Wiley and Sons, Ltd Publication (2010).

6

CRITICALITY OF GUST LOADS

In classic aeroelastic tailoring analysis and optimization, which models a clamp-free wing structure, the dynamic response is overestimated thus making the method conservative due to the fact that all the energy coming from the gust perturbation is converted into the wing structural deformation. In the case where the wing is free to move at the root, some of that energy will dissipate into elevating and rotating the whole structure thus alleviating its overall deflection. This simple consideration prompts the author to reassess the role of dynamic loads in the sizing a composite structure.

This chapter is divided into two main sections. In the first one, both the clamp-free and free-free gust responses will be analyzed in order to benchmark the reduction in elastic deflection due to the change in boundary condition. The second section discusses the criticality of the dynamic load in the aeroelastic tailoring optimization. Both static and dynamic loads will be considered in the optimization. A loading condition will be considered critical when it results in higher margins compared to other loading conditions. The static maneuver loads will be taken into account both with and without maneuver load alleviation, performed by deflecting the control surfaces to shift most of the lift inboard.

6.1. DYNAMIC RESPONSES IN COMPARISON

Before going into the details of the sizing loads, it is useful to discuss the dynamic response of a wing under the two different boundary conditions, namely either *(i)* clamp-free or *(ii)* free-free.

The literature on this topic highlights that the clamp-free model tends to overestimate the response to a dynamic excitation, e.g. vertical gust [1], making the dynamic cases the sizing loading condition for a particular wing model. This is true in most cases, but it is important to understand the limitations of the clamp-free models and the many factors influencing the amplitude or criticality of the dynamic response.

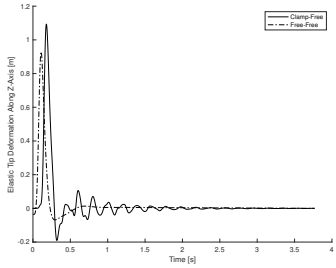

(a) Vertical displacement history at the wing tip.

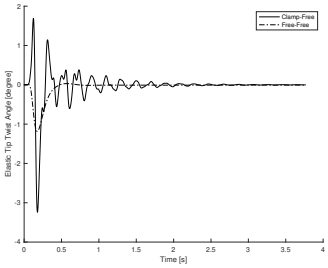

(b) Elastic twist history at the wing tip.

Figure 6.1: Dynamic responses of the clamp-free and free-free wing in comparison.

Let us imagine an aircraft is in cruise flight and encounters a vertical gust. The gust can be seen as additional energy added to the system. This energy can be dissipated in different ways. The result is a vibration that is a combination of three main responses:

- the aircraft elevation,
- the aircraft pitch rotation,
- an additional oscillating elastic deformation of the wing.

The energy will dissipate through these three outlets, but the amount of energy each channel takes will depend on its inertial properties. In particular, the clamp-free model assumes the wing will take all the additional energy coming in the system from the vertical gust. This means the fuselage inertial properties are many orders of magnitude higher (or infinitely higher, mathematically speaking) than the one of the wing. The fuselage is thus acting as a clamp for the wing. The more comparable the inertial properties, the more energy will be dissipated through elevating and pitching the aircraft as opposed to oscillating elastic deflections in the wing.

The question, from a structural design standpoint, is then to understand by how much the wing main structure is over-designed as a result of adopting the classic clamp-free boundary conditions. That will allow to exploit the full weight-saving potential of composite materials with the scope of designing lighter and fuel efficient structures.

For the CRM aircraft, the comparison between the two dynamic responses is shown in Fig. 6.1. For the vertical tip displacement, a 15% decrease in the positive peak can be observed. The reduction in absolute value of the negative peak of deflection and elastic twist is such that both buckling of the bottom skin and aeroelastic instability are likely to be less critical. This reduction in the peak of the dynamic response was obtained with a fuselage to wing inertial ratio of approximately 10^3, meaning that the inertia of the fuselage is 3 orders of magnitude higher than the one of the wing.

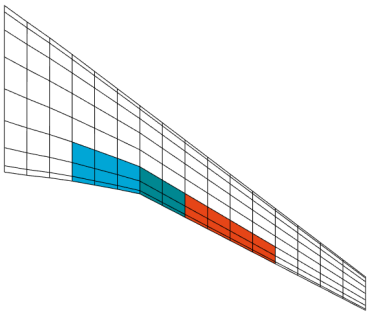

(a) Position of the control panels for maneuver load alleviation.

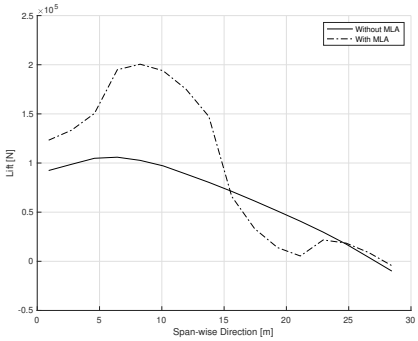

(b) Example of attainable inboard shift in lift.

Figure 6.2: Details of the control panels for maneuver load alleviation.

6.2. GUST RESPONSE WITH MANEUVER LOADS ALLEVIATION

The goal of maneuver load alleviation is to reduce the root bending moment on the wing structure. This is obtained by shifting most of the lift towards the inboard region. To alter the distribution on the CRM wing, three control surfaces are modeled as shown in Fig. 6.2(a). The control surfaces in blue and green are deflected downwards (positive rotation) to increase the lift generated in the inboard area. Conversely, the long surface in orange is deflected upwards (negative rotation) to drop lift in the outboard area. An example of the type of distribution attainable with such a distribution of control surfaces is shown in Fig. 6.2(b). This allocation of the control surfaces is based on two conditions:

- the control panels at the further end of the wing are left for roll control,
- the left-most control surface (blue) is located close to the fuselage-wing junction and is a dual surface, assuming it can used both as a flap as for maneuver load alleviation. The literature on this matter refers to such surfaces as flaperon, [2].

6.3. LOADING CONDITIONS

The loading conditions taken into account for the optimization study are the standard CRM static maneuver points, shown in Tab. 6.1, together with two dynamic cases each modeling a (1 – cos) gust perturbation in the most extreme points of the flight envelope. The expression for the standard (1 – cos) gust is hereby given:

$$v_g = 0.5 v_{max} \left(1 - \cos \frac{\pi p}{H}\right) \tag{6.1}$$

where v_{max} is the velocity peak, p is the gust penetration measured in meters, and H is the half length in meters. The gust loads are shown in details in Tab. 6.2. A visual representation of the gust perturbation is found in Fig. 6.3. The half lengths are chosen such that the wing is excited around its first bending frequency. In particular, the gust at half length of 40 m has a frequency close to the first wing bending frequency.

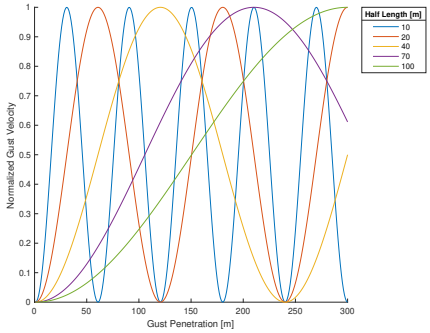

Figure 6.3: Visual representation of the gust perturbations at different half lenghts.

Table 6.1: CRM standard static maneuver points.

Description	Load ID	EAS [m/s]	Mach [-]	Altitude [m]	Load Factor [g]
Cruise	1	136	0.85	11,000	1.0
Pull-up	2	240	0.85	3,000	2.5
Push-down	3	198	0.85	0	-1.0

6.4. OPTIMUM DESIGNS AND SIZING LOADS

A summary of the structural mass of the wing of the optimum design is given in Tab. 6.3. The discussion is mainly focused on the wing structural mass given its high impact on the optimization margins and objective function. For clarification purposes, the objective function is formulated as:

$$\text{obj} = \frac{\text{Wing Structural Mass} + \text{Tail Structural Mass}}{(\text{Wing Structural Mass} + \text{Tail Structural Mass})_0} \tag{6.2}$$

where subscript 0 refers to the structural mass of the initial design point given to the optimizer. The structural mass includes the mass of the wing box only, namely skins, spars and stringers. The rib mass is not included in those values given that it remains constant during the aeroelastic tailoring optimization.

With reference to Tab. 6.3, the observations made on the present aeroelastic tailoring optimization study will be discussed. The observations will particularly be with respect to the effect of maneuver load alleviation, free-free boundary condition and the change in sizing loads on the optimum design.

6.4.1. EFFECT OF MANEUVER LOAD ALLEVIATION

Alleviating the static loads shifts most of the lift generation to the inboard area of the wing. As a result the root bending moment (RBM) is reduced significantly. The RBM of the optimum design is reduced by 16%, 6.0% and 9.0% in cruise, pull-up at 2.5 g and

Table 6.2: CRM dynamic loads (vertical gust perturbation).

Load ID	EAS [m/s]	Mach [-]	Altitude [m]	Gust Velocity [m/s]	Half Lengths [m]
4	150	0.45	0	17	10 - 20 - 40 - 70 - 100
5	240	0.80	11,000	17	10 - 20 - 40 - 70 - 100

Table 6.3: Overview of the wing structural mass of the optimum designs.

	With MLA	W/o MLA
Clamp-Free	5,652 kg	6,530
Free-Free	5,467	6,340

push-down at -1.0 g respectively. These relative changes, with respect to the initial design, are larger than the reduction obtained as a byproduct of the load redistribution during aeroelastic tailoring. A consequence of minimizing the structural mass is to passively alleviate loads by means of tailoring the stiffness and mass distribution. The reduction in RBM is the main cause of stress relief on the wing that allows the objective function, in this case the stuctural mass, to converge on lower values compared to the cases without any alleviation. Each of the cases will be discussed in detail.

MLA in the Clamp-Free Boundary Condition: the clamp-free boundary condition overestimates the dynamic response to a gust perturbation, since all of the additional energy brought into the system is converted into wing structural deformation. In the case where MLA is not activated, the dynamic case is the sizing load for the wing structure. With the activation of the control surfaces for load alleviation, the overall criticality of the static maneuver points is lowered. At the same time the inboard area, where most of the lift is generated, will experience higher shear loads as a result of the higher local stresses in the area. As a consequence, with active MLA with clamp-free boundary conditions, the inboard area tends to be designed by static loads, the outboard by dynamic loads since it is relieved of the static ones. The difference in the sizing loads can be observed in the strain margins distribution along the wing in Fig. 6.4.

MLA in the Free-Free Boundary Condition: the free-free boundary conditions reduced the positive peak of the dynamic response to a gust perturbation. For this reason, when the loads are not alleviated on the wing, the static maneuver load tends to be the sizing ones. This obviously depends on the relative reduction of the criticality of the dynamic response. For the CRM aircraft this reduction remains around 10% also for the optimum design. When MLA is activated, the outboard area is relieved of the static strains and thus sized by the dynamic loads. However, the inboard area, similarly to the case with active MLA in a clamp-free boundary condition, will still be sized by the static maneuver loads given the high lift concentration in this area. The details on the sizing loads are shown in Fig. 6.5.

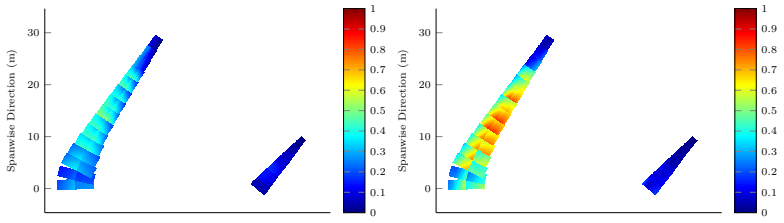

(a) Pull-up maneuver: MLA ✗ (b) Gust loads: MLA ✗

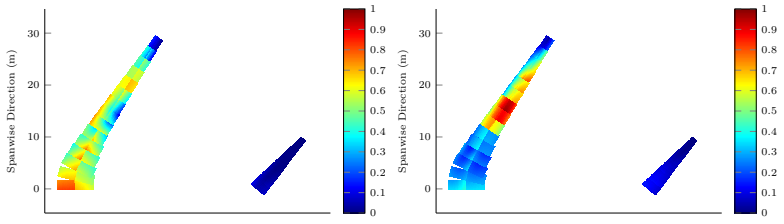

(c) Pull-up maneuver: MLA ✓ (d) Gust loads: MLA ✓

Figure 6.4: Strain margins under maneuver load alleviation in the clamp-free model.

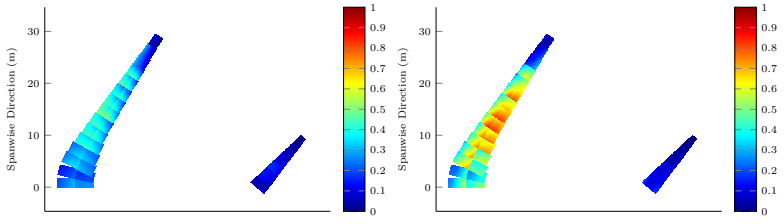

(a) Push-up maneuver: MLA ✗ (b) Gust load: MLA ✗

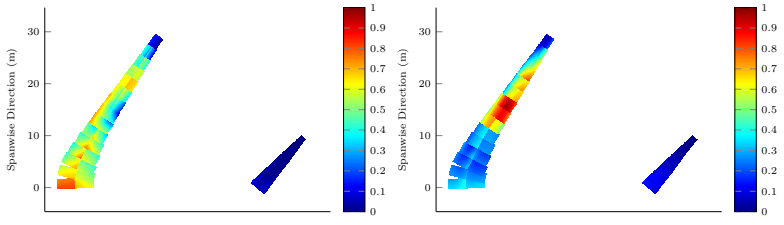

(c) Push-up maneuver: MLA ✓ (d) Gust loads: MLA ✓

Figure 6.5: Strain margins under maneuver load alleviation in the free-free model.

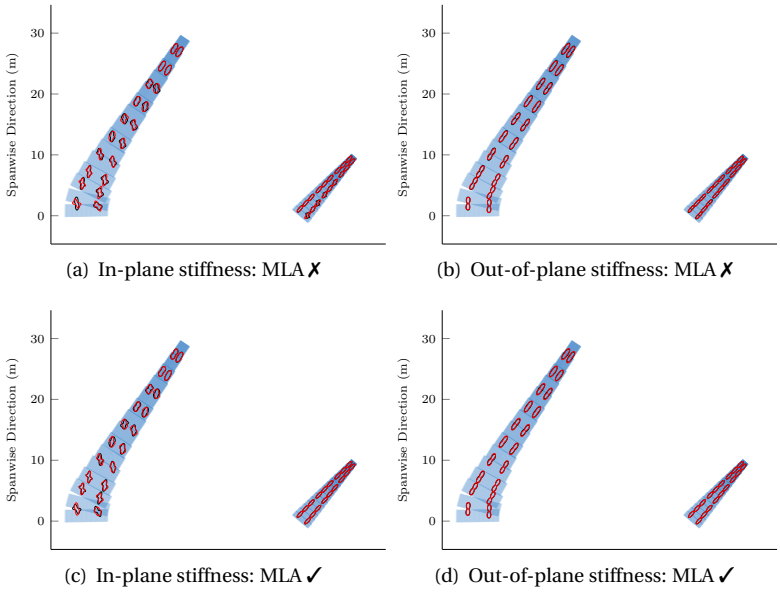

(a) In-plane stiffness: MLA ✗ (b) Out-of-plane stiffness: MLA ✗

(c) In-plane stiffness: MLA ✓ (d) Out-of-plane stiffness: MLA ✓

Figure 6.6: Overview of stiffness variation because of a change in boundary condition.
Legend - **black:** clamp-free, red: free-free

6.4.2. EFFECT OF THE FREE-FREE BOUNDARY CONDITION

The change in boundary condition has a marginal change on the converged objective. The effect on the optimization drivers is however twofold:

- the boundary condition changes the optimum stiffness distribution, enhancing wash-out and local stiffening based on the load redistribution during the optimization as seen in Fig. 6.6. The out-of-plane stiffness properties are less sensitive to changes in boundary conditions compared to the in-plane ones.
- the change in boundary condition from clamp-free to free-free shifts the sizing loads and the overall dominance of static and dynamic loads along the wing. This shift is more pronounced if MLA is not active.

6.5. OVERVIEW OF RELATIVE CHANGES IN STRUCTURAL MASS

The relative changes in objective function are quantified in this section with reference to the previous discussion on the effect of maneuver load alleviation and change in boundary condition.

	Clamp-Free		Free-Free	
	With MLA	W/o MLA	With MLA	W/o MLA
Wing Structural Mass [kg]	5,652	6,530	5,467	6,340
Relative Difference [%]	-13	-	-14	-

	With MLA		W/o MLA	
	Clamp-Free	Free-Free	Clamp-Free	Free-Free
Wing Structural Mass [kg]	5,652	5,467	6,630	6,340
Relative Difference [%]	-	-2.8	-	-2.9

6.6. SYNTHESIS AND CRITICALITY MATRIX

The considerations in this chapter can be collected in the criticality matrix as a qualitative reference for future studies in optimization of composite structure under combined statics and dynamics loads. Note that the static loads are taken into account both with and without maneuver load alleviation.

	With MLA	W/o MLA
Clamp-Free	The static loads design inboard region, the dynamic ones the outboard.	Dynamic loads are critical.
Free-Free	The static loads design the inboard region. The loading conditions are comparable in the outboard one.	Dynamic loads are critical.

By excluding the maneuver load alleviation from the optimization, the sizing condition is only determined by whether a particular analysis method is overestimating the dynamic response or not. In the former case, the dynamic loads will be critical. In the latter, the static loads.

The introduction of maneuver load alleviation makes the prediction more complicated since the static and dynamic loading conditions compete to design particular areas. A rather clear trend has been observed for the clamp-free wing, where the static loads size the inboard regions (due to the shift of lift towards the mid-plane), while the dynamic size the outboard ones. For the free-free case, this distinction is less clear and will have to be determined case by case. This depends on the degree of alleviation realized in the model, both statically through MLA and dynamically through the ratio of inertial properties.

The criticality matrix is meant to give awareness to engineers and structural designers of the limitations and/or implications of a particular approach. For structures of conventional aircraft that are more prone, for example, to dynamic instabilities, it might be good practice to be on the conservative side when predicting the dynamic response and thus give it a higher weight in the sizing process. By being more aware of the implications of a particular analysis and optimization practice, one can make better decisions at the start of the design process taking into account the unique characteristics of a given structure.

REFERENCES

[1] N. Werter, *Aeroelastic modelling and design of aeroelastically tailored and morphing wings,* PhD Dissertation, Delft University of Technology (2017).

[2] W. Scott, *Morphing wings,* Aviation Week and Space Technology (2006).

CONCLUSIONS

The observations in this dissertation will be organized in two main sections. In the first one, we will refer back to the main objective of the dissertation and comment on the importance of a comprehensive analysis and optimization framework for preliminary design of composite structures. The second and last section will discuss the future developments suggested by the author to advance the capabilities of the presented framework.

REFLECTIONS ON THE OBJECTIVE OF THIS DISSERTATION

With this dissertation, the author set out to develop a preliminary design framework for aeroelastic tailoring optimization of a full composite aircraft. With said framework the author has been able to address and contextualize some of the limitations of the state-of-the-art classic aeroelastic tailoring designs. The classic aeroelastic tailoring design refers to the aeroelastic optimization of a clamp-free structural wing model. Contextualizing the common assumptions behind the classic aeroelastic tailoring frameworks brings depth to the results and conclusions drawn at preliminary design level. The main observations are hereby summarized.

Classic vs Full Aircraft Tailoring

Modeling the flexible aircraft within the aeroelastic tailoring framework inevitably adds more phenomena to account for and thus more drivers to the optimization. Among said drivers, two play an important role and affect the optimum design, namely the flight dynamic stability and the horizontal tail.

The longitudinal flight dynamic stability comes in the equation from the fact that the boundary condition at the symmetry plane is changed from clamped to free. This allows to enforce flight stability as a constraint during the optimization and control dynamic instabilities such as the *body-freedom flutter*. Moreover, one could also already control the maneuverability parameters of the aircraft by constraining the relevant handling qualities. Being able to do this at preliminary design level means altering the path to the optimum design by adding new constraint. This translated in a mass and performance penalty.

The effect of the horizontal tail is twofold and the final effect on the optimum design is case dependent. Designing the horizontal tail allows the optimizer more control on the flight stability response, making it easier to avoid instabilities or match the requirements on handling qualities. On the other hand, the horizontal tail plays an important role in the moment equilibrium equation. Depending on the center of gravity position, this

might cause increased loads on the wing surface which results in higher margins and thus higher objective function (i.e. structural mass).

Optimum vs Better Stiffness Distribution
The optimum stiffness distribution achieved by adopting unbalanced/symmetric laminates is often times not realistic because of the complications of actually manufacturing and certifying the laminates resulting from such distribution. Being able to account for this at preliminary design level means finding a way to incorporate, for example, existing certified stacking sequences in the aeroelastic tailoring framework. By doing so, one can achieve a better stiffness distribution, compared to the optimum with unbalanced/symmetric laminates, yet incorporating the benefits of stiffness tailoring and passive load alleviation in the final design. Working with certified stacking sequence and allowing the tailoring of their principal direction shifts more responsibilities on the structural engineers for the selection of the appropriate sequences at the onset of the optimization for maximum performance.

Optimum vs Better Mass Distribution
The mass distribution contributes to the passive load alleviation in two ways, namely by *i)* chord- and *ii)* span-wise mass differentials. Let us know look at each of these mechanisms separately to discuss their effect on the wing model.

Chord-wise Mass Differential The chord-wise mass differential is a passive load alleviation method used in both skins and spars. It causes the leading edge of the skins, or the leading edge spar to be stiffer than the trailing edge counterpart. As a result, upon elastic deformation, the leading edge tends to deflect less compared to the trailing edge inducing wash-out.

Span-wise Mass Differential The span-wise mass distribution is optimized to stiffen the design around either heavily loaded areas of areas where heavy non-structural masses are attached to. An example of span-wise mass tailoring can be observed around where the engine is mounted.

One important factor for the realization of the optimum mass distribution is the following. Every change in mass distribution causes the loads along of the wing to be redistributed. The redistribution is feasible if the optimizer can find the stiffness distribution that can bear those loads. The extend the optimizer can actually reach the optimum mass distribution is related to the size of the stiffness design space.

Sizing Loads
All the extra factors included at preliminary design level have the potential to cause a shift in the sizing loads on the wing structure. Understanding the limitations behind a particular approach is the key to understanding the limitations related to the optimum design. More attention is to be given to the assumptions needed to use a particular model. For example, it has been observed that in cases where the inertia of the fuselage

is larger by several orders of magnitude than the one of the wing, the clamp-free boundary condition describes the model fairly well. It is only when the ratio between the two inertia gets lower that the model shows its limitations, e.g. overestimating a dynamic response to a vertical perturbation. These differences ultimately translate to differences in the sizing loads in an optimization.

SUGGESTED FUTURE WORK

As discussed in the reflections of the previous section, the ability to solve 'advanced' problems at preliminary design is crucial for the later phases of the design cycle. With the aim of increasing the level of confidence in the results at medium- to low-fidelity level, useful in the preliminary design phase, the author suggests five focus areas:

I. Software Architecture

Being able to address the modeling challenges at preliminary design level requires a great deal of thought in the software architecture of a given tool. Said architecture will provide:

- the modularity needed to embed different solutions for the various physics-based problems that are of importance in the preliminary studies. The solutions are not necessarily to be built-in, but could be provided by existing tools or established commercial software. The latter can also serve as reference in verification studies.
- the framework needed to explore a wide range of configurations varying high-level design parameters, and
- the scalability required to address realistic problems and handle the added complexity that comes with it.

II. Allowables and Failure Mechanisms

The design of composite structure is as good as the allowables used to characterize the materials and predict its failure. In this context, quick, physics-based model could help update the failure margins for critical areas of a particular design.

III. Loads Prediction

In a similar fashion as for the previous comment, the structural analysis is only as good as the loads that are applied on it. The limitations of panel-based models in their ability to predict local loads and local transonic effect are known in literature. This area also calls for fast and physics-based models to incorporate said effects at preliminary design level.

IV. Control

The load alleviation techniques explored in this dissertation are limited to passive alleviation through the optimization of stiffness and mass distribution. This optimization is usually performed requiring no aeroelastic instability in the process. Enabling the aeroelastic stability constraint inevitably limits the design space. Aeroservoelasticity, which is aeroelasticity with the addition of control design, can help explore new design options and new configurations.

A

Appendix A: Ch. 3 - Rotation Matrix

A

TIME DERIVATIVE OF A ROTATION MATRIX

A rotation matrix $\underline{\underline{R}}(t)$ benefits of the following property, such that:

$$\underline{\underline{R}}(t)\underline{\underline{R}}^T(t) = \underline{\underline{I}} \tag{A.1}$$

with $\underline{\underline{I}}$ being the identity matrix. Taking the time derivative of both sides, one has:

$$\frac{\mathrm{d}}{\mathrm{d}t}\underline{\underline{R}}(t)\underline{\underline{R}}^T(t) + \underline{\underline{R}}(t)\frac{\mathrm{d}}{\mathrm{d}t}\underline{\underline{R}}^T(t) = 0 \tag{A.2}$$

or equivalently:

$$\frac{\mathrm{d}}{\mathrm{d}t}\underline{\underline{R}}(t)\underline{\underline{R}}^T(t) + \left(\frac{\mathrm{d}}{\mathrm{d}t}\underline{\underline{R}}(t)\underline{\underline{R}}^T(t)\right)^T = 0 \tag{A.3}$$

which means that the term $\underline{\underline{S}}(t)$ defined as:

$$\underline{\underline{S}}(t) = \frac{\mathrm{d}}{\mathrm{d}t}\underline{\underline{R}}(t)\underline{\underline{R}}^T(t) \tag{A.4}$$

is a skew symmetric matrix, in this case of the pseudo-vector or rotations. By post-multiplying Eq. A.3 by $\underline{\underline{R}}(t)$, we have:

$$\frac{\mathrm{d}}{\mathrm{d}t}\underline{\underline{R}}(t) = \underline{\underline{S}}(t)\underline{\underline{R}}(t) \tag{A.5}$$

Q.E.D.

B

Appendix B: Ch. 3 - Lagrangian Dynamics

B

LAGRANGIAN DYNAMICS OF FLEXIBLE BODIES

The velocity and acceleration of any given point on the structure, taking into account its initial position and deformation, were given in Eq. 3.22 and 3.23:

$$\begin{cases} \ddot{\underline{r}} = \begin{bmatrix} \underline{\underline{R}} & \underline{\underline{\tilde{I}}} & \underline{\underline{\tilde{r}}} \end{bmatrix} \begin{bmatrix} \ddot{\underline{\delta}} \\ \dot{\underline{r}}_{EB} \\ \underline{\omega}_{EB} \end{bmatrix} + \underline{\underline{\Omega}}\,\underline{\underline{\Omega}}\,\underline{r} + 2\,\underline{\underline{\Omega}}\,\underline{\underline{R}}\,\dot{\underline{\delta}} \\ \dot{\underline{r}} = \begin{bmatrix} \underline{\underline{R}} & \underline{\underline{\tilde{I}}} & \underline{\underline{\tilde{r}}} \end{bmatrix} \begin{bmatrix} \dot{\underline{\delta}} \\ \underline{r}_{EB} \\ \underline{\omega}_{EB} \end{bmatrix} \end{cases} \tag{B.1}$$

These expression can be used in the generic Lagrangian term hereby given:

$$\frac{\mathrm{d}}{\mathrm{d}t}\frac{\partial T}{\partial \dot{q}} - \frac{\partial T}{\partial q} = \underbrace{M\ddot{q}}_{1} + \underbrace{\dot{M}\dot{q}}_{2} - \frac{1}{2}\dot{q}^T\left(\frac{\partial M^T}{\partial q}\right)\dot{q} \tag{B.2}$$

with T being the kinetic energy of the system and q its degrees of freedom. The non-linear terms including $\partial M/\partial q$ will not be addressed since outside of the scope of this dissertation. The terms number 1 and 2 will now be analyzed separately.

1. *Mass Matrix*
   Remembering that the definition of kinetic energy is:
   $$T = \underline{v}^T\,\underline{\underline{M}}\,\underline{v} \tag{B.3}$$
   and the mass matrix can be derived as:
   $$M_{i,j} = \frac{\partial^2 T}{\partial \dot{q}_i \partial \dot{q}_j} \tag{B.4}$$
   in view of Eq. B.1, the mass matrix can be rewritten as:
   $$\underline{\underline{M}}_s = \begin{bmatrix} \underline{\underline{R}} & \underline{\underline{\tilde{I}}} & \underline{\underline{\tilde{r}}} \end{bmatrix}^T \underline{\underline{M}} \begin{bmatrix} \underline{\underline{R}} & \underline{\underline{\tilde{I}}} & \underline{\underline{\tilde{r}}} \end{bmatrix} \tag{B.5}$$

2. *Acceleration Forces*
   Taking the time derivative of the mass matrix previously defined, one has:
   $$\dot{\underline{\underline{M}}} = \frac{\mathrm{d}}{\mathrm{d}t}\left\{ \begin{bmatrix} \underline{\underline{R}} & \underline{\underline{\tilde{I}}} & \underline{\underline{\tilde{r}}} \end{bmatrix}^T \underline{\underline{M}} \begin{bmatrix} \underline{\underline{R}} & \underline{\underline{\tilde{I}}} & \underline{\underline{\tilde{r}}} \end{bmatrix} \right\} \equiv 2 \begin{bmatrix} \underline{\underline{R}} & \underline{\underline{\tilde{I}}} & \underline{\underline{\tilde{r}}} \end{bmatrix}^T \underline{\underline{M}} \begin{bmatrix} \underline{0} & -\underline{\underline{\Omega}}\,\underline{\underline{\tilde{r}}} - \underline{\underline{R}}\,\dot{\underline{\underline{\delta}}} & \underline{\underline{\Omega}}\,\underline{\underline{R}} \end{bmatrix} \tag{B.6}$$
   This term will be now multiplied by the velocity vector, thus obtaining:
   $$\underline{f}_{\text{acc}} = \dot{\underline{\underline{M}}}\,\dot{\underline{q}} = 2 \begin{bmatrix} \underline{\underline{R}} & \underline{\underline{\tilde{I}}} & \underline{\underline{\tilde{r}}} \end{bmatrix}^T \underline{\underline{M}} \begin{bmatrix} \underline{0} & -\underline{\underline{\Omega}}\,\underline{\underline{\tilde{r}}} - \underline{\underline{R}}\,\dot{\underline{\underline{\delta}}} & \underline{\underline{\Omega}}\,\underline{\underline{R}} \end{bmatrix} \begin{bmatrix} \dot{\underline{\delta}} & \dot{\underline{r}} & \underline{\omega} \end{bmatrix}^T \tag{B.7}$$
   which can be simplified in:
   $$\underline{f}_{\text{acc}} = \begin{bmatrix} \underline{\underline{R}} & \underline{\underline{\tilde{I}}} & \underline{\underline{\tilde{r}}} \end{bmatrix}^T \underline{\underline{M}} \left(\underline{\underline{\Omega}}\,\underline{\underline{\Omega}}\,\underline{r} + 2\,\underline{\underline{\Omega}}\,\underline{\underline{R}}\,\dot{\underline{\delta}} \right) \tag{B.8}$$
   Q.E.D.

C

Appendix C: CRM Aircraft

VERIFICATION MODEL

The aircraft model used for the verification is the NASA Common Research Model (CRM)[1]. The CRM is used to create three configurations: *(i)* wing-only indicated with W, *(ii)* wing and horizontal tail indicated with WT and *(iii)* symmetric aircraft with flexible wing, horizontal tail and fuselage indicated with AC. In the WT configuration, a rigid link is implemented to connect the two parts[2].

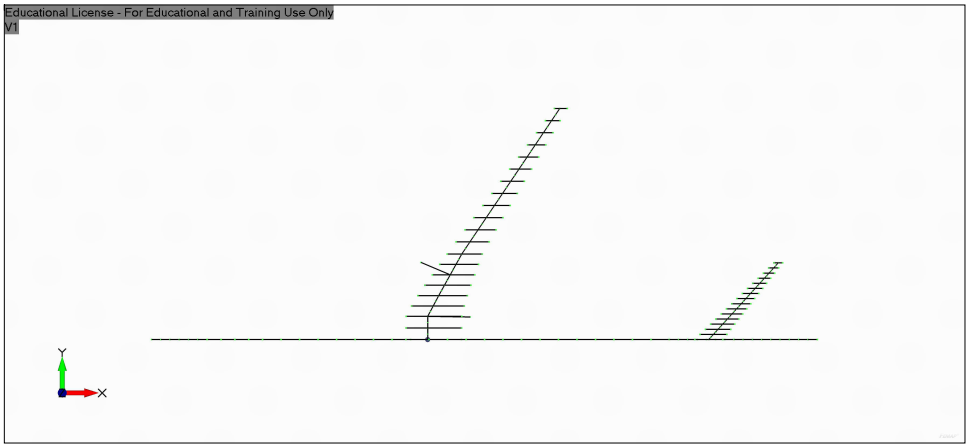

Figure C.1: NASTRAN® model of the full aircraft structure.

A summary of the most important characteristics of the model is hereby given.

Quantity	Unit	Value
Wing span	m	58.8
Wing area	m^2	410.7
Tail span	m	19.5
Tail area	m^2	91.3
Fuselage length	m	85.0
Fuselage radius	m	3.0
Distance wing-tail[3]	m	39.0
Wing structural mass[4]	kg	10500.0
Tail structural mass	kg	1326.0
Fuselage structural mass	kg	20790.0
Engine mass	kg	9700.0
Main landing gear mass	kg	4810.0
Fuel mass	kg	52580.0

[1] https://commonresearchmodel.larc.nasa.gov
[2] The equivalent of a NASTRAN RBE2.
[4] The distance is measured from the leading edge of both surfaces.
[4] The value of structural mass includes skins, spars, ribs and stringers.

D

APPENDIX D: BUCKLING MODEL

D.1. BUCKLING

This section gives an overview of the buckling model used in this dissertation as idealized and developed by [1].The model is used to define the inverse buckling reserve factor r, used as a failure index,

$$r = \text{FS} \cdot \frac{N}{N_{\text{buckl}}} \tag{D.1}$$

where FS is the factor of safety. The index r ranges from 0 to 1, where:

- 0 indicates that buckling is not critical for a particular panel ($N_{\text{buckl}} = \infty$), while
- 1 indicates that the panel is operating at the prescribed margin of safety.

The margin for the buckling analysis has been set to 0.4375, where both the safety factor for certification purposes (FS_c) and the knockdown factor for environmental conditions (k) is included. The breakdown of the margin of safety is as follows:

$$\text{MS} = \frac{\text{FS}_c}{k} - 1 \tag{D.2}$$

by using the typical values for both factors (Ref. [2]),

$$\text{MS} = \frac{1.15}{0.8} - 1 \tag{D.3}$$

and thus obtained a total margin of safety of 0.4375 (or equivalently a factor of safety of 1.4375).

The patch between two ribs and two stringers is modeled as a simply-supported flat panel under in-plane loads. The simply-supported boundary condition holds under the assumption that the stiffeners do not buckle, not separate from the panel.

The wing is discretized in quadrilateral elements, and for each of the element the inverse buckling reserve factor is calculated. The geometry of the panel is projected in the local coordinate system, and mapped to the standard square described by the following normalized coordinates:

$$-1 \leq \xi \geq 1 \tag{D.4}$$

$$-1 \leq \eta \geq 1 \tag{D.5}$$

The bending displacement w is formulated in normalize coordinates using Lobatto shape functions,

$$w = \sum_i a_i \phi_i(\xi, \eta) \tag{D.6}$$

Let $\mathbf{a}$ be vector containing the coefficients a_i multiplying the Lobatto shape functions. The strain energy for each panel is written as,

$$2U = \mathbf{a}^T \mathbf{K} \mathbf{a} \tag{D.7}$$

where $\mathbf{K}$ is the stiffness matrix of the panel given by,

$$\mathbf{K} = D_{11}\mathbf{K}^{11} + D_{12}\mathbf{K}^{12} + D_{16}\mathbf{K}^{16} + D_{22}\mathbf{K}^{22} + D_{26}\mathbf{K}^{26} + D_{66}\mathbf{K}^{66} \tag{D.8}$$

The matrices $\mathbf{K}^{ij}_{pq}$ are the integral of the second derivative of the shape functions. For example, the term $\mathbf{K}^{11}$ is calculated as,

$$K^{11}_{pq} = \int_{\Omega} \frac{\partial^2 \phi_p}{\partial x^2} \frac{\partial^2 \phi_q}{\partial x^2} d\Omega \tag{D.9}$$

Equivalently the potential energy can be written as,

$$2V = \mathbf{a}^T \mathbf{K}_g \mathbf{a} \tag{D.10}$$

where $\mathbf{K}_g$ is the geometric stiffness matrix defines as,

$$\mathbf{K}_g = -N_x \mathbf{K}^{xx} - N_y \mathbf{K}^{yy} - N_{xy} \mathbf{K}^{xy} \tag{D.11}$$

where $\mathbf{K}^{xx}$, $\mathbf{K}^{yy}$ and $\mathbf{K}^{xy}$ are given by the following integrals,

$$K^{xx}_{pq} = \int_{\Omega} \frac{\partial \phi_p}{\partial x} \frac{\partial \phi_q}{\partial x} d\Omega \tag{D.12}$$

$$K^{yy}_{pq} = \int_{\Omega} \frac{\partial \phi_p}{\partial y} \frac{\partial \phi_q}{\partial y} d\Omega \tag{D.13}$$

$$K^{xy}_{pq} = \int_{\Omega} \frac{\partial \phi_p}{\partial x} \frac{\partial \phi_q}{\partial y} d\Omega \tag{D.14}$$

From the expressions for strain and potential energy the eigenvalue problem can be formulated as follows,

$$\left(\mathbf{K}_g - r\mathbf{K}\right)\mathbf{a} = \mathbf{0} \tag{D.15}$$

where r is the inverse buckling factor. The constraint formulation is thus,

$$r - 1 \leq 0 \tag{D.16}$$

D

REFERENCES

[1] J. Dillinger, *Static aeroelastic optimization of composite wings with variable stiffness laminates"*, PhD Dissertation, Delft University of Technology (2014).

[2] C. Kassapoglou, *Design and analysis of composite structures with applications to aerospace structures,* John Wiley and Sons, Ltd Publication (2010).

E

Appendix E: Ch. 4 - Optimum Design

E.1. THICKNESS

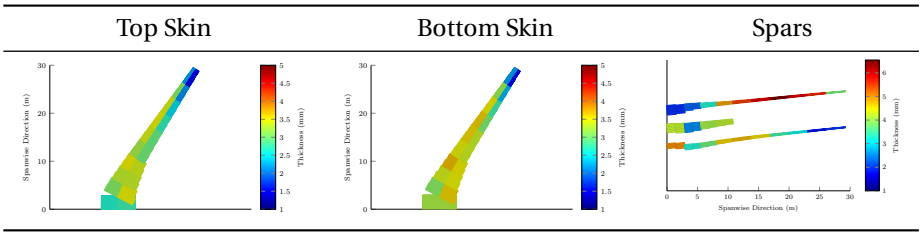

Figure E.1: Optimized thickness of the reference wing (ID = 0).

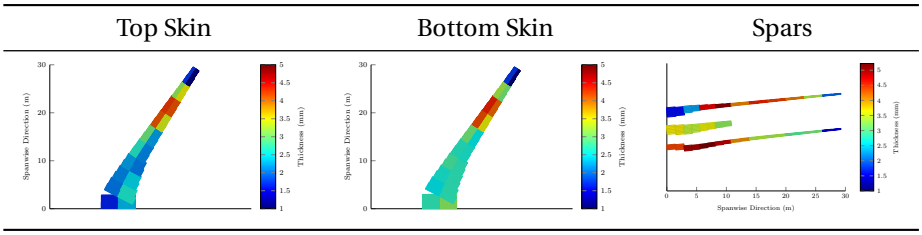

Figure E.2: Optimized thickness of the free-free wing (ID = 1).

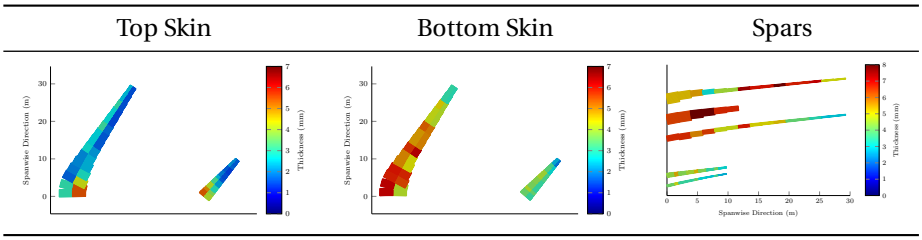

Figure E.3: Optimized thickness of the flexible aircraft (ID = 2).

E.2. IN-PLANE STIFFNESS

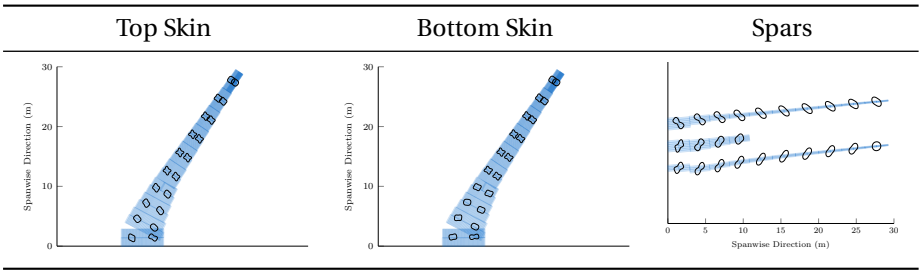

Figure E.4: Optimized in-plane stiffness of the reference wing (ID = 0).

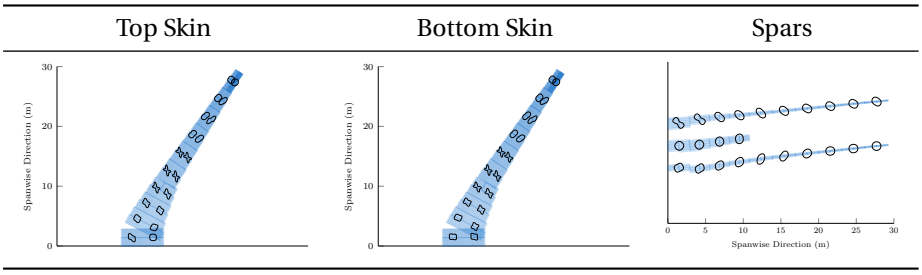

Figure E.5: Optimized in-plane stiffness of the free-free wing (ID = 1).

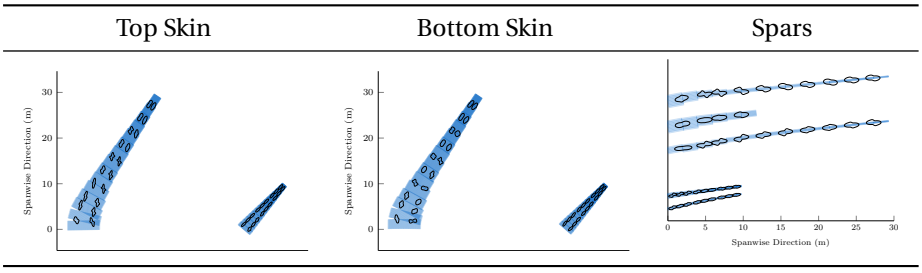

Figure E.6: Optimized in-plane stiffness of the flexible aircraft (ID = 2).

E.3. OUT-OF-PLANE STIFFNESS

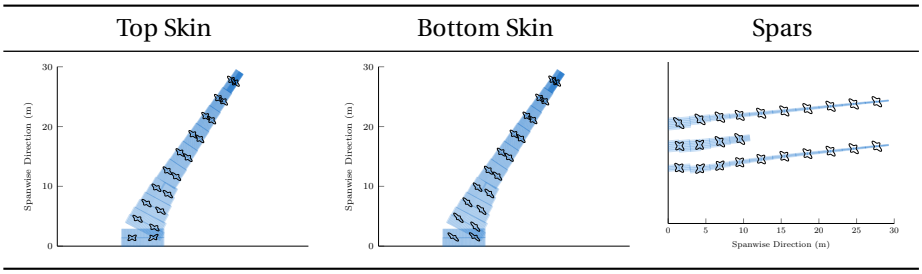

Figure E.7: Optimized out-of-plane stiffness of the reference wing (ID = 0).

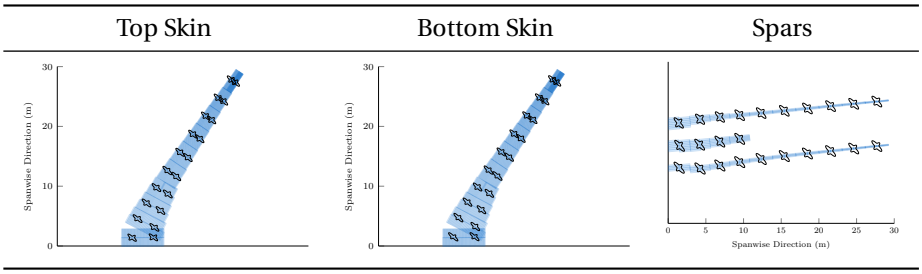

Figure E.8: Optimized out-of-plane stiffness of the free-free wing (ID = 1).

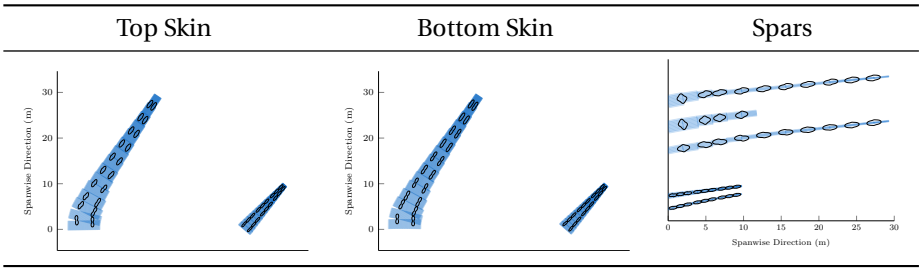

Figure E.9: Optimized out-of-plane stiffness of the flexible aircraft (ID = 2).

F

Appendix F: Ch. 4 - Margins

F.1. STRAIN MARGINS

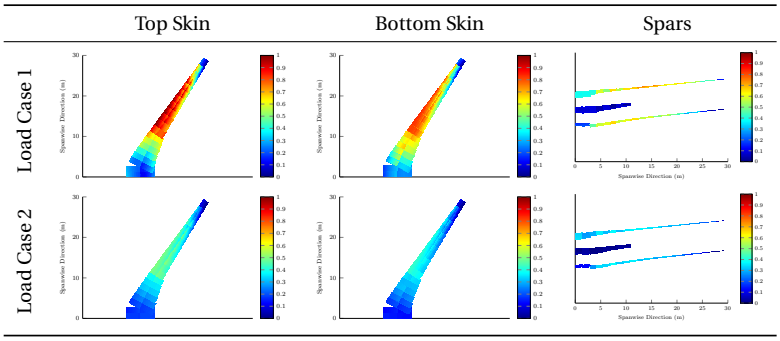

Figure F.1: Strain margins of the reference wing (ID = 0).

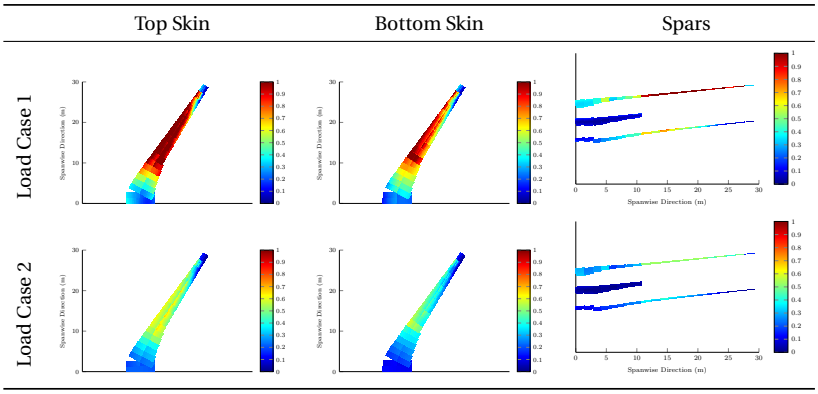

Figure F.2: Strain margins of the free-free wing (ID = 1).

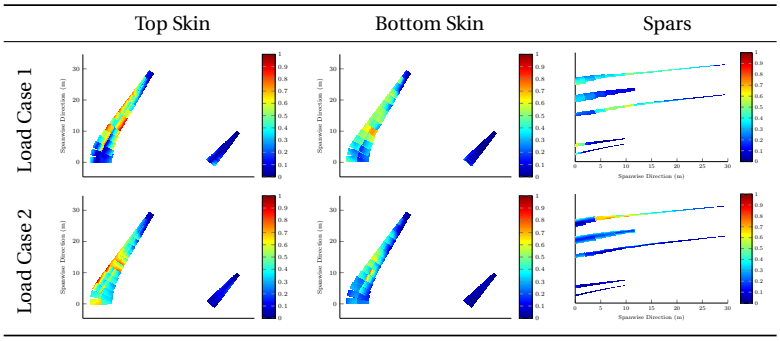

Figure F.3: Strain margins of the flexible aircraft (ID = 2).

F.2. BUCKLING MARGINS

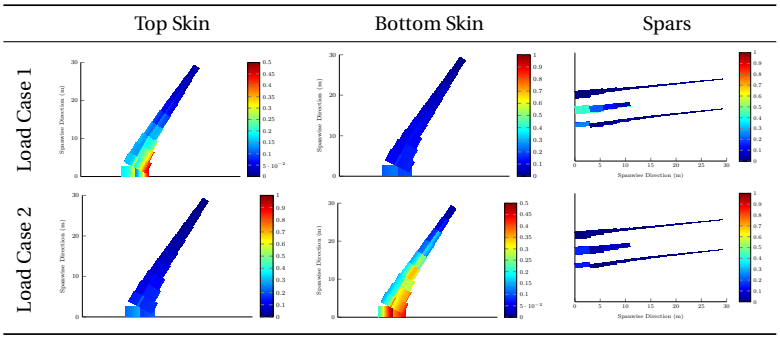

Figure F.4: Buckling margins of the reference wing (ID = 0).

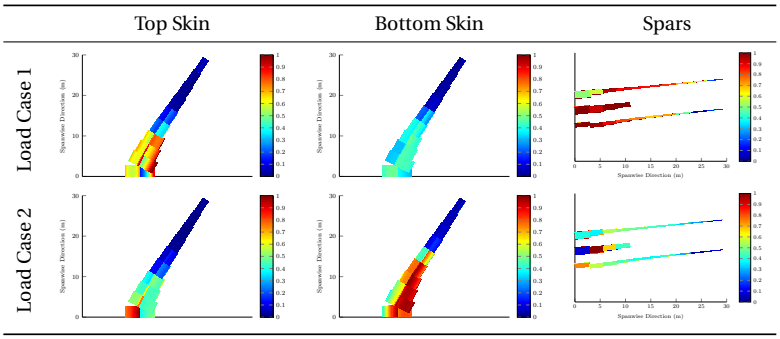

Figure F.5: Buckling margins of the free-free wing (ID = 1).

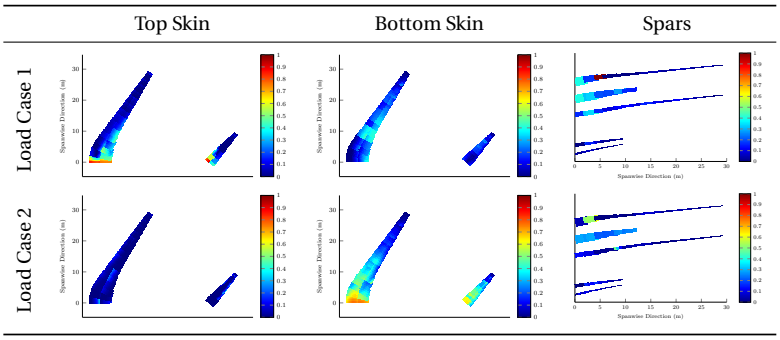

Figure F.6: Buckling margins of the flexible aircraft (ID = 2).

G

Appendix G: Ch. 5 - Optimum Design

G.1. THICKNESS

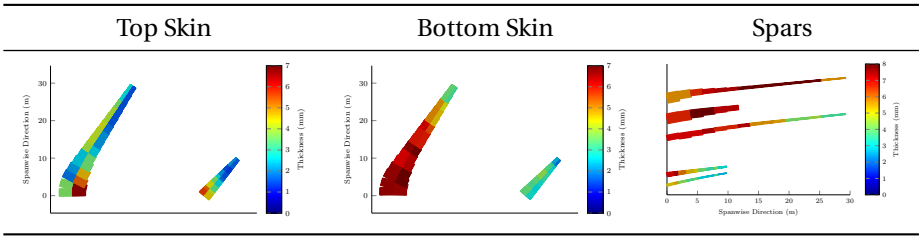

Figure G.1: Optimized thickness of the reference aircraft (fixed laminates).

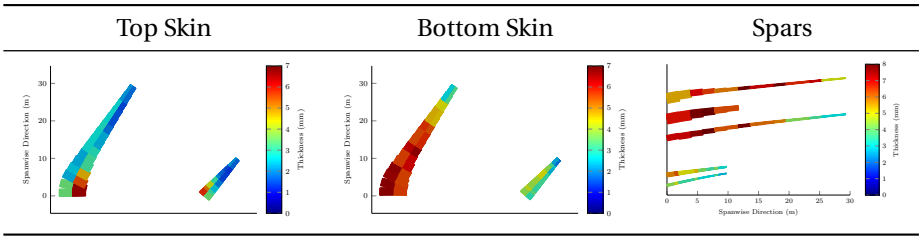

Figure G.2: Optimized thickness using principal direction optimization.

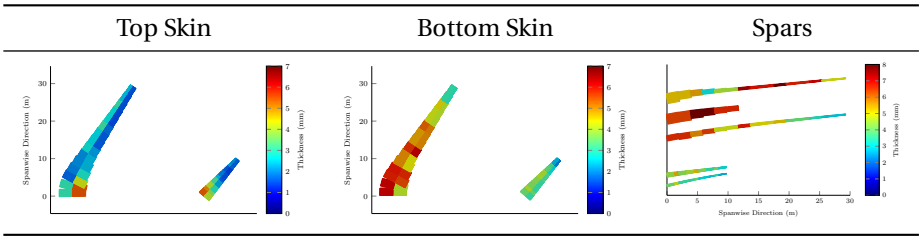

Figure G.3: Optimized thickness using unbalanced/symmetric laminates.

G.2. IN-PLANE STIFFNESS

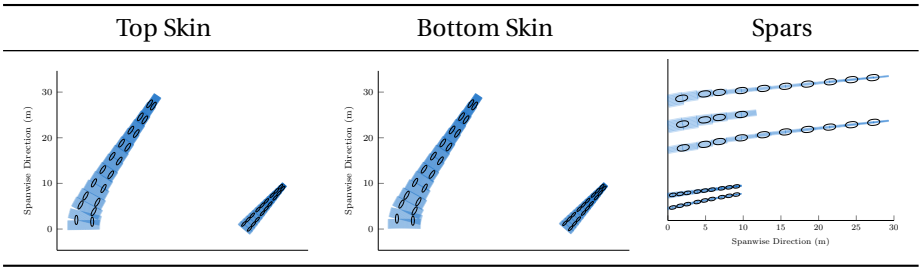

Figure G.4: Optimized in-plane stiffness of the reference aircraft (fixed laminates).

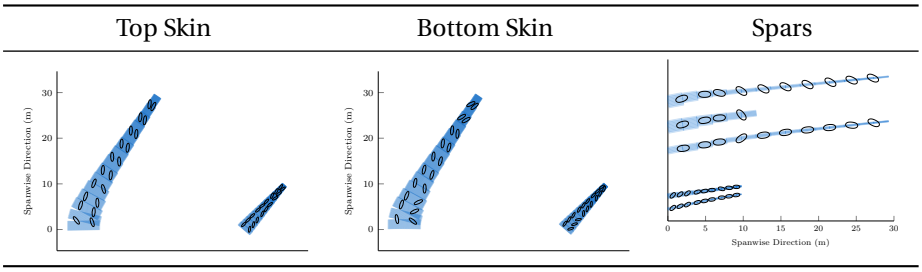

Figure G.5: Optimized in-plane stiffness using principal direction optimization.

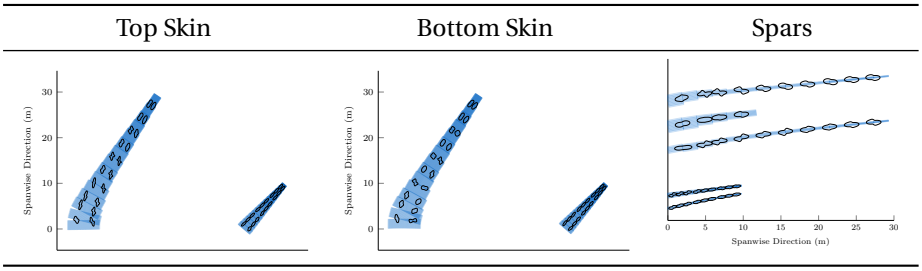

Figure G.6: Optimized in-plane stiffness using unbalanced/symmetric laminates.

G.3. OUT-OF-PLANE STIFFNESS

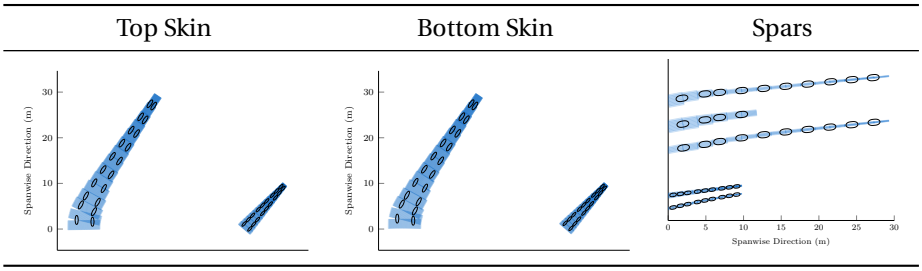

Figure G.7: Optimized out-of-plane stiffness of the reference aircraft (fixed laminates).

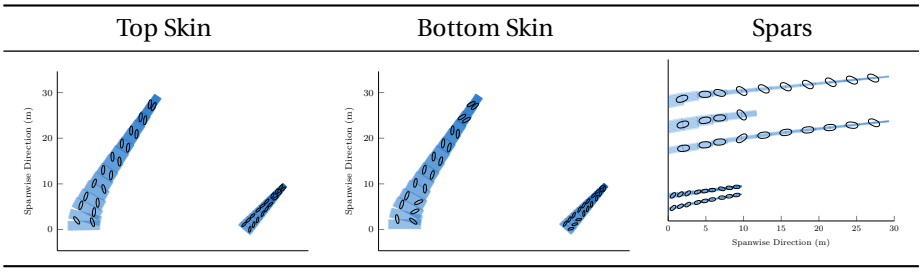

Figure G.8: Optimized out-of-plane stiffness using principal direction optimization.

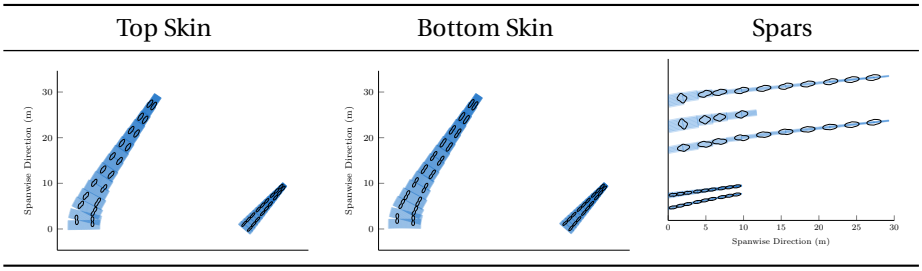

Figure G.9: Optimized out-of-plane stiffness using unbalanced/symmetric laminates.

H

Appendix H: Ch. 5 - Margins

H.1. STRAIN MARGINS

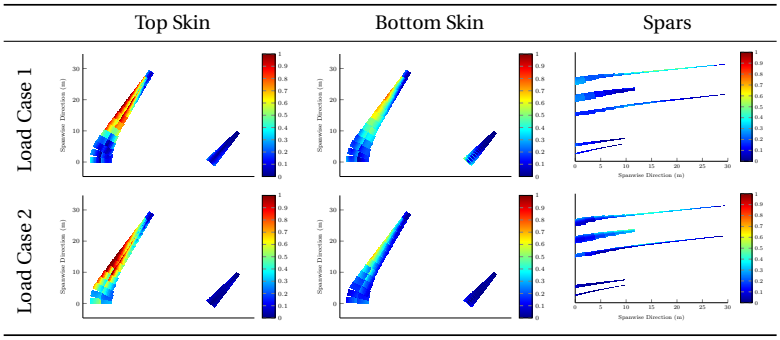

Figure H.1: Strain margins of the reference aircraft (fixed laminates).

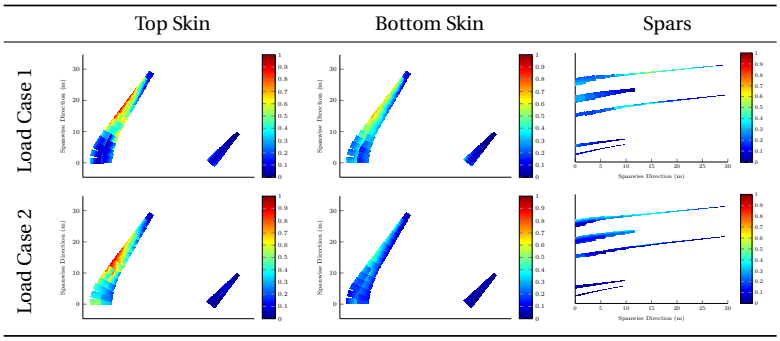

Figure H.2: Strain margins using principal direction optimization.

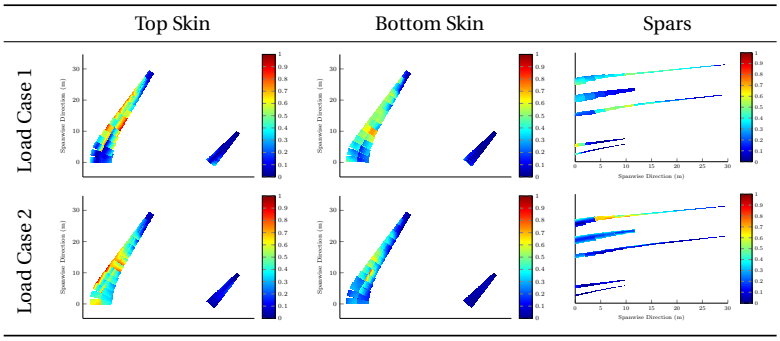

Figure H.3: Strain margins using unbalanced/symmetric laminates.

H.2. BUCKLING MARGINS

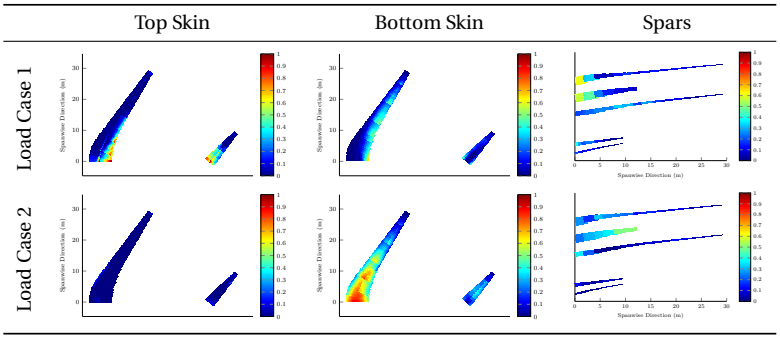

Figure H.4: Buckling margins of the reference aircraft (fixed laminates).

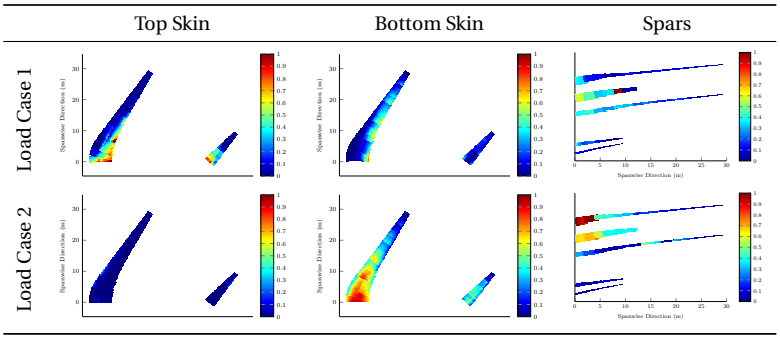

Figure H.5: Buckling margins using principal direction optimization.

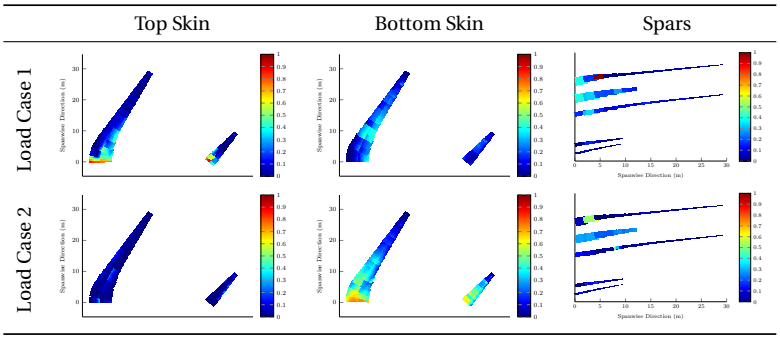

Figure H.6: Buckling margins using unbalanced/symmteric laminates.

ACKNOWLEDGEMENTS

Directed by:
Mario Natella

Promoted, encouraged and supported by:
Roeland De Breuker

Mentored with love by:
Esmay Verschuren

Assistant Directors:
Bibi (Babacita) and Basilicum van den Bosch

CAST:
The Families
Los Natellas
De Verschurens and Begemanns

The Industry Experts
Pedro Higino Alonso de Passos Cabral
Alex Pereira do Prado
Gustavo (Zorg) Henrique di Caprio Silva

Gli Sventrapapere a mazza chiegata
Gennaro Bellizzi and Francesco (Ciccio) Menduni

The Holy Chickens
Sharhzad Timman, Jacqueline Chindea

Sparring Partner
教授王雪蕊

The Office Colleagues
Darwin Rajpal
Paul Lancelot
Tigran Mkhoyan
洪智
Javier (Saverio) Gutierrez
Ines Uriol Balbin
and many more...